Dissertation

submitted to the
Combined Faculty for the Natural Sciences and Mathematics
of the Heidelberg University, Germany

for the degree of
Doctor of Natural Sciences

Put forward by

M. Sc. Renato Félix Bautista
Born in Tepic, Mexico

Oral examination: June 21st, 2021

Monitoring of lateral positions of therapeutic carbon-ion pencil beams using secondary ion tracking

This PhD thesis has been carried out
at the German Cancer Research Center (DKFZ) in Heidelberg
under the supervision of Dr. Mária Martišíková

Referees: Prof. Dr. Joao Seco

Prof. Dr. Oliver Jäkel

Zusammenfassung

Die Strahlentherapie mit Kohlenstoff-Ionen wurde als hocheffektive Modalität für die Krebsbehandlung entwickelt. Aufgrund der präzisen Dosisverteilungen werden gesunde Organe in der Umgebung des Tumors besser geschont als bei der Standard-Radiotherapie mit Photonen. Allerdings ist die Dosisverteilung in der Strahlentherapie mit Kohlenstoffionen sensitiver auf Unsicherheiten. Daher sind Strategien zur Überwachung des Ionenstrahls während einer Behandlung, idealerweise direkt im Patienten, von großer Bedeutung. In dieser Arbeit wurde eine nicht-invasive Methode zur Messung der lateralen Positionen von bleistiftartigen Kohlenstoffionenstrahlen im Patienten entwickelt. Sie basiert auf der Detektion und Spurverfolgung der geladenen Kernfragmenten, die den behandelten Patienten als Sekundärstrahlung verlassen. Die Leistungsfähigkeit der entwickelten Methode wurde an patientenähnlichen Modellen, die die klinische Situation nachahmen, am Heidelberger Ionenstrahl-Therapiezentrum (HIT) in Heidelberg, Deutschland, untersucht. Darüber hinaus wurde die entwickelte Methode zum ersten Mal während einer Patientenbehandlung getestet. Die Präzision, Genauigkeit und Effektivität der entwickelten Methode wurden als klinisch relevant erwiesen im Bezug auf den maximal akzeptierten Unsicherheiten von 1 mm. Außerdem konnte die Strahlbewegung verfolgt werden, was zukünftig zur Online Strahlüberwachung genutzt werden könnte. Diese unabhängige Strahlüberwachungsmethode ist bereit, an einer größeren Patientengruppe in einer klinischen Studie evaluiert zu werden.

Abstract

Carbon-ion beam radiotherapy has been developed as a highly effective modality for cancer treatment. Based on the precise dose distributions of carbon-ion treatments, a better sparing of healthy organs surrounding the tumor site compared to the standard photon radiotherapy are provided. However, dose distributions in carbon-ion beam radiotherapy are more prone to uncertainties. Therefore, strategies to monitor the ion beam during a treatment delivery, ideally directly in the patient, are of great importance. In this thesis, a non-invasive methodology to measure the lateral pencil beam positions in the patient has been developed. It is based on detection and tracking of charged nuclear fragments leaving the treated patient as secondary radiation. The performance of the developed methodology was investigated in patient-like models mimicking clinical situations at the HIT facility in Heidelberg, Germany. Moreover, the developed methodology has been tested for the first time during a real patient treatment. Precision, accuracy and effectivity of the developed method were found to be clinically attractive compared to the maximal accepted uncertainties of 1 mm. Additionally, the beam movement was aiming towards online carbon-ion beam monitoring. This independent beam monitoring methodology is ready to be evaluated on a larger patient group in a clinical study.

Contents

Scientific Contributions iii

1. Introduction 1
1.1. The role and the benefits of carbon-ion beams in radiation therapy 1
1.2. Challenges of carbon-ion beams in radiation therapy 2
1.2.1. Carbon-ion treatment uncertainties 2
1.2.2. QA limitations 2
1.2.3. Synchrotron-base facility limitations 3
1.2.4. Need for carbon-ion beam monitoring 4
1.3. Aim of the thesis 4
1.3.1. Methodology requirements 5
1.4. Thesis structure 6

2. Physics and radiobiology of ion beams for monitoring in radiotherapy 7
2.1. Physical processes of ions in matter 7
2.1.1. Stopping power 7
2.1.2. Straggling of energy loss and of range 10
2.1.3. Lateral scattering 12
2.1.4. Nuclear fragmentation 13
2.2. Physical advantages of carbon-ion beam radiotherapy 16
2.3. Beam monitoring of nuclear fragmentation 19
2.4. Radiobiology of ion beams in radiation therapy 21
2.4.1. Linear energy transfer 21
2.4.2. Biological concepts of modeling the repair mechanisms of cells 21
2.4.3. Relative biological effectiveness 23
2.5. Cyclotron- and synchrotron-based therapy facilities 25
2.6. Semiconductor detectors 26

3. Materials and Methods 31
3.1. Heidelberg Ion-Beam Therapy Center 31

3.1.1. The active raster scanning technique ... 32
3.1.2. Monitoring system at beam nozzle and beam record files ... 33
3.2. Treatment plans used ... 34
3.3. Secondary ion tracking system ... 36
3.4. Experimental configurations for the pencil beam monitoring ... 40
3.4.1. Tracking system positioned at 30° ... 40
3.4.2. Tracking system positioned at the beam axis (0°) ... 41
3.4.3. Measurements of real–patient treatment delivery ... 42
3.5. Data processing and analysis ... 44
3.5.1. Clusterization and coincidence processes ... 44
3.5.2. Analysis of ion tracks ... 46
3.5.3. Effectivity, precision and accuracy of the method ... 47

4. Results and Discussion ... 51
4.1. Pencil beam monitoring with the tracking system positioned at 30° ... 52
4.1.1. Comparison between measured and reference lateral beam positions ... 52
4.1.2. Precision and accuracy ... 54
4.1.3. Reproducibility ... 55
4.1.4. Sensitivity ... 56
4.1.5. Alignment of the tracking system ... 58
4.1.6. Discussion to 4.1 ... 59
4.2. Pencil beam monitoring with the tracking system positioned at 0° ... 60
4.2.1. Comparison of the results with the tracking system positioned at 30° and 0° ... 63
4.2.2. Performance of the method for a real clinical treatment plan ... 65
4.2.3. Discussion to 4.2 ... 71
4.3. First clinical measurement during a patient treatment ... 73
4.3.1. Testing of influence on the beam monitoring system ... 73
4.3.2. Measurements and results ... 74
4.3.3. Discussion to 4.3 ... 76
4.4. Overall discussion and outlook ... 77

5. Summary ... 81

6. Conclusions ... 83

Bibliography ... 85

Acknowledgments ... 97

Scientific Contributions

Papers

- **Félix-Bautista, R.**, Gehrke, T., Ghesquiere-Diérickx, L., Reimold, M., Amato, C., Turecek, D., Jakubek J., Ellerbrock M. and Martišiková, M. (2019). Experimental verification of a non-invasive method to monitor the lateral pencil beam position in an anthropomorphic phantom for carbon-ion radiotherapy. Physics in Medicine and Biology, 64(17). https://doi.org/10.1088/1361-6560/ab2ca3

- **Félix-Bautista, R.**, Ghesquiere-Diérickx, L., Marek, L., Granja, C., Soukup, P., Turecek, D., Brons, S., Ellerbrock, E., Jäkel, O., Gehrke, T. and Martišiková, M. (2021). Quality assurance method for monitoring of lateral pencil beam positions in scanned carbon-ion radiotherapy using tracking of secondary ions. Provisionally accepted in Medical Physics.

Conferences

- **Félix-Bautista, R.**, Gehrke, T., Reimold M. and Martisikova, M. **Poster:** Assessment of the lateral pencil beam positions in a treatment-like situation. National Center for Radiation Research in Oncology Retreat, Dresden, Germany, 2018.

- **Félix-Bautista, R.**, Gehrke, T., Ellerbrock, M. and Martisikova, M. **Talk:** Intrafractional visualisation of the scanning pencil beam in 12C radiotherapy. 57th Annual Conference of the Particle Therapy Co-Operative Group, Cincinnati, USA, 2018.

- **Félix-Bautista, R.**, Ghesquière-Diérickx, L., Reimold, M., Gehrke, T., Ellerbrock, M. and Martišíková, M. **Poster:** In vivo monitoring using secondary ions: lateral beam scanning. 3rd Heidelberg Symposium on Novel Techniques in Ion Beam Radiotherapy, Heidelberg, Germany, 2018.

- **Félix-Bautista, R.**, Ghesquière-Diérickx, L., Gehrke, T., Ellerbrock, M. and Martišíková, M. **Talk:** Monitoring of lateral pencil beam positions in carbon-ion beam therapy. 2019th DKFZ PhD Retreat, Weil der Stadt, Germany, 2019.

- **Félix-Bautista, R.**, Ghesquière-Diérickx, L., Gehrke, T., Turecek, D., Jakubek, J., Ellerbrock, M. and Martišíková, M. **Talk:** Non-invasive visualization of the pencil beam scanning movement in an irradiated object during a carbon-ion beam therapy delivery. 21st International Workshop on Radiation Imaging Detectors, Chania, Crete, Greece, 2019.

- **Félix-Bautista, R.**, Ghesquière-Diérickx, L., Gehrke, T., Turecek, D., Jakubek, J., Ellerbrock, M. and Martišíková, M. **Poster:** Monitoring method to visualize the lateral pencil beam movement during scanned carbon-ion beam radiotherapy. 2019 IEEE Nuclear Science Symposium & Medical Imaging Conference, 2019, Manchester, UK, 2019. (MIC Poster Session, IEEE Trainee Grant)

- **Félix-Bautista, R.**, Ghesquière-Diérickx, L., Gehrke, T., Turecek, D., Jakubek, J., Ellerbrock, M. and Martišíková, M. **Poster:** Secondary ion tracking to visualize the lateral pencil beam movement during scanned Carbon-Ion Beam Therapy. 2019th DKFZ PhD Poster Presentation, Heidelberg, Germany, 2019.

Chapter 1
Introduction

1.1. The role and the benefits of carbon-ion beams in radiation therapy

Different particle techniques have been used and developed over the past years for cancer treatments, since particles were first proposed by Robert R. Wilson in 1946, and first used for treatments at the Lawrence Berkeley Laboratory in 1954 [Giap and Giap, 2012]. The number of particle therapy treatments with protons and carbon ions is increasing worldwide, and especially in Europe [Grau et al, 2020]. At the end of 2019, more than 250 000 patients have been treated with protons and carbon ions [PTCOG Patient Statistics].

Ions can deliver dose to the tumor in a more conformal manner, i.e., following the shape of the tumor. This is possible because primary ions stop inside the patient and the maximum dose deposition of the ions, the so-called Bragg peak, is placed at the end of their trajectory. The highly localized maximum dose deposition is the primary physical rationale for using ions for cancer treatments [Durante and Debus, 2018]. The entire tumor can be irradiated by adjusting the position of the maximum dose deposition region by changing the primary ion beam energy. The direct consequence of this is that the healthy tissue and organs at risk surrounding the tumor can be better spared in comparison to the existing cancer treatment modalities with photons (e.g., VMAT, IMRT/IGRT, SBRT) [Fiorino et al, 2020]. In addition, protons and carbon ions in radiotherapy particularly exhibit an enhancement of their biological effectiveness over radiotherapy with photons. This is considered the main biological rationale for the use of ions for radiotherapy [Durante and Debus, 2018].

Among the available particle therapy modalities, carbon-ions offer several advantages compared to protons. As carbon ions have higher mass than protons, the scattering in air, inside the patient and even in the beam nozzle is decreased. From this, narrower carbon-ion pencil beams can be delivered, in contrast to proton beams. Additionally,

carbon ions have shown higher benefit for treating radio-resistant tumors, minimizing the toxicity to sensitive healthy tissue [Schulz-Ertner et al, 2006; Combs et al, 2012], as well as significant benefits for cancer treatments in clinical trials of skull base, head and neck, gastrointestinal and central nervous system, among others [Malouff et al, 2020; Schaub et al, 2020]. Moreover, carbon-ion beam radiation therapy (CIRT) has been and still being studied in combination with other cancer treatment modalities, such as, chemotherapy, immunotherapy, intensity-modulated radiation therapy and surgery, to further investigate the full benefits of CIRT [Malouff et al, 2020].

1.2. Challenges of carbon-ion beams in radiation therapy

1.2.1. Carbon-ion treatment uncertainties

Benefits of carbon-ion beams in radiation therapy also bring challenges. These challenges are related to the delivered dose distribution quality and sensitivity to even minor changes in the delivery system and in the patient geometry, among others [Eley et al, 2015]. These uncertainties can compromise the quality of the delivered dose and thus potentially the outcome of the treatment as well.

Uncertainties can originate from inside the patient due to organ motion, weight loss and tumor shrinkage along the course of the treatment [Lomax, 2008]. Other uncertainties can be related to fluctuations in the ion beam parameters, such as the beam energy, size, position and number of delivered primary ions [Rizzoglio et al, 2020]. These uncertainties can lead to undesirable variations of the ion beam range and lateral beam positions, deteriorating the proper delivered dose and causing potentially underdosage of the tumor or overdosage of healthy tissue, in particular at organs at risk surrounding the tumor [Lomax, 2008]. Uncertainties can also be introduced during the acquisition of computed tomography or magnetic resonance imaging performed for diagnosis, planning and treatment purposes [Pereira et al, 2014; FitzGerald et al, 2018]. This imaging procedure can be performed in in-room or out-room modalities, also used to identify potential changes concerning the patient geometry. Imaging is integrated in the standard clinical routine, following a detailed program for the high-quality treatment to be delivered to the patient [Jäkel et al, 2000; Molinelli et al, 2013; Zhu et al, 2015; Bizzocchi et al, 2017].

1.2.2. QA limitations

Quality assurance (QA) verifications are based on measurements of the parameters of the therapeutic ion beams. These beam parameters can be measured before and during patient treatment deliveries using multi-wire proportional chambers and ionization chambers located inside the beam nozzle [Parodi et al, 2012], and one multi-wire proportional chamber placed directly at the room isocenter. These QA measurements are

used for machine-related verifications, but they can also be used for patient-related verifications. Indeed, patient-related measurements are occasionally performed to verify the designed plans for new treatments and check the suitability of the equipment when delivering such new treatment plans. For that, treatment plans are delivered onto water phantoms [Jäkel et al, 2001], which do not correspond to the actual geometry of the patient. These QA patient-related verifications are only performed once before the first delivery of a new treatment plan.

On the other hand, QA machine-related verifications at the isocenter are carried out every morning before starting the treatment deliveries of the day [Jäkel et al, 2000]. However, such machine-related measurements only verify the beam quality at the isocenter once per day, and only some beam energies, size and positions are evaluated[1].

QA machine-related verifications in the beam nozzle are always performed during any type of irradiation. The real-time verification of the therapeutic ion beam parameters directly during a patient treatment delivery can only be performed using the multi-wire proportional chambers and ionization chambers located inside the beam nozzle [Parodi et al, 2012]. These ion beam parameters are then extrapolated to the room isocenter.

1.2.3. Synchrotron-base facility limitations

In synchrotron-based facilities, the beam is deflected via magnets in the plane perpendicular to the beam direction to irradiate a specific spot. The active raster scanning is the technique used for the ion beam delivery at the Heidelberg Ion-Bam Therapy Center (HIT) (see section 2.3.1 for more details). The tumor volume is segmented into virtual slices. These iso-energy slices are irradiated by changing the ion beam energy. With this technique, the tumor volume is completely covered by the desired dose. However, carbon-ion beams in synchrotron-based facilities suffer from inherent disadvantages compared to cyclotrons-based facilities. The nozzle-to-isocenter distance is much larger at synchrotron-based facilities and the beam extraction may cause variations of the lateral beam positions at the isocenter. Uncertainties of 1 mm in the lateral positions of the beam contribute to a dose inhomogeneity of more than 5 % [Li et al, 2013; Actis et al, 2014]. Moreover, the extrapolation of the lateral beam position from the beam nozzle to the isocenter is more challenging for synchrotron-based facilities than for those with cyclotrons, due to the fine-tuning of several components during the beam delivery. At HIT, where de nozzle-to-isocenter distance is 1.1 m [Tessonnier et al, 2016] –which represent an increase of two to five times of the distance compared to cyclotron-based facilities–, a source point in between the deflecting scanner magnets is considered for the

[1] Dr. Stephan Brons, personal communication, HIT, 2020.

extrapolation. This leads to spill-to-spill variations depending on the beam energy and size.

Therefore, given all of this, the monitoring of lateral pencil beam positions in radiotherapy with carbon ions is even of much more importance than with protons.

1.2.4. Need for carbon-ion beam monitoring

Since the already existing real-time beam monitoring system are not in the room isocenter, but inside the beam nozzle, real-time QA methodologies capable of monitoring the lateral carbon-ion pencil beam positions at the isocenter without interfering with that point have to be developed.

In particular, the existing QA methodologies use different types of detectors e.g., scintillator detectors, flat panels detectors, parallel-plane ionization chambers, among others. No procedures concerning the real-time monitoring of the lateral pencil beam positions based on hybrid pixel semiconductor detectors are available so far. This thesis addresses the verification of lateral spot positions of carbon-ion beam scanning during the treatment delivery using hybrid pixel detectors for particle tracking.

1.3. Aim of the thesis

As described above, misplacements of the lateral ion beam positions in the isocenter arising from different sources of uncertainties can compromise the quality of the delivered dose and thus potentially also the outcome of the treatment.

In this thesis, the development of a methodology to monitor the lateral positions of carbon-ion pencil beams in the isocenter during scanned carbon-ion beam radiotherapy, without any interaction with the primary beam, is presented. This methodology is considered as an independent and complementing tool to the already existing ion beam verification strategies. In comparison to other beam verification techniques, this methodology addresses the monitoring of lateral beam positions during the treatment delivery.

This proposed methodology is based on the detection and tracking of charged nuclear fragments (referred to as secondary ions in this thesis), generated by nuclear inelastic interaction between the therapeutic ion beams and the target nuclei, and leaving the irradiated object or patient. The performance of the methodology is evaluated in terms of effectivity, reproducibility, precision and accuracy.

The secondary-ion signal is detected by using fast hybrid silicon pixel detectors, developed by the Medipix, and later Timepix, Collaboration with the knowledge gained in High-Energy Particle Physics at CERN [Poikela et al. 2014].

The detection and tracking of secondary ions using these detectors have been investigated in this thesis to provide information concerning the lateral position of the irradiated spot.

Therefore, the novel methodology proposed in this thesis is a candidate for non-invasive lateral ion-beam position verifications during the treatment delivery.

1.3.1. Methodology requirements

Important requirements were identified first. This thesis is structured according to the requirements of the development of a novel independent and complementing methodology for the verification of the lateral ion beam position.

a) Since the yield of secondary ions is important for the assessment of the methodology in terms of precision and accuracy, the tracking system has to be able to achieve single ion detection for therapeutic carbon-ion beam intensities.
b) The methodology aims to reach the clinically acceptable uncertainties of ±1 mm in the lateral positions of pencil beam.
c) In order to reach an effectivity of 100%, two positions of the tracking system are investigated: 0° and 30° relative to the beam direction.
d) The methodology has to allow assessing both lateral directions (vertical and horizontal) and reproducing the pattern of the reference pencil beam scanning movement laterally.
e) The methodology is designed to work with enough statistics in order to reach the clinically accepted uncertainties. For that, the tracking system requires technology capable of overcoming challenges due to the high secondary-ion fluence rate at the small detection angle (0°). Thus, changes in the hardware of the detectors are introduced, i.e., new chipboards to enhance the synchronization between the detectors, together with the fine-tuning of detector parameters for an optimal operation.
f) Most of the existing ion beam monitoring based on secondary ion detection are designed for the verification of the ion beam range, and some of them are used in conjunction with positron emission tomography. This proposed monitoring methodology is intended to be simultaneously used for twofold purposes in future: verifications of expected stopping positions and of lateral beam positions at the isocenter.

g) For the potential application in daily clinical situations of the proposed methodology, treatment plans are especially designed for patient-like objects, as well as treatment plans for real patients are tested.

1.4. Thesis structure

The structure of this thesis is the following. Chapter 2 describes comprehensive background of the physical processes involved in the interactions of therapeutic ions with matter, and the differences in the beam delivery techniques between therapy centers based on cyclotron and synchrotron accelerators. Experimental configurations, the used detection and tracking system and the developed data analysis techniques are presented in Chapter 3. The found results are presented and discussed in Chapter 4. Chapter 5 gives an outlook summarizing future investigations, and conclusions.

The content of this thesis is based on three main investigations as follows:

i. Experiments in a head phantom with the tracking system positioned at 30° relative to the beam axis

ii. Experiments in the head phantom with the tracking system positioned at 0° relative to the beam axis, divided in two parts:
    a. Comparison with the experiments performed at 30°.
    b. Measurements to assess the capabilities of the monitoring methodology using a real patient treatment plan.

iii. First clinical application of the proposed monitoring methodology performed during a patient treatment with the tracking system positioned at 30° relative to the beam axis.

A part of the presented results was already published (see section 4.1) [Félix-Bautista et al, 2019] and accepted for a second publication (see section 4.2) [Félix-Bautista et al, 2021].

Chapter 2

Physics and radiobiology of carbon-ion beams and methods for monitoring in radiation therapy

In this chapter the physical processes of the passage of ions through matter, including the detection of ions with semiconductor detectors, and the radiobiological aspects of carbon-ion beam radiotherapy are explained. The most relevant topics in these fields for a better understanding of this thesis are presented in the following order. In section 2.1, physical concepts as stopping power, energy and range straggling, lateral scattering and nuclear fragmentation as interactions of ions interacting with matter are described. In section 2.2, these interactions of ions with matter are presented from a clinical perspective. The radiobiology of therapeutic ion beams in radiotherapy is explained in section 2.3. In section 2.4, the differences concerning the operational parameters and the ion beam delivery between cyclotron- and synchrotron-based cancer treatment facilities are described. Finally, a brief explanation about semiconductor detectors is given in section 2.5, since the detection of ions created during carbon-ion irradiations in this thesis is based on this type of detectors.

2.1. Physical processes of ions in matter

2.1.1. Stopping power

The stopping power (S) of ions, is defined as the mean energy loss ($\overline{dE}$) in a path length of any material (dx), as shown in equation 2.1:

$$S = -\left(\frac{\overline{dE}}{dx}\right). \tag{2.1}$$

The minus sign in equation 2.1 is introduced to have positive values for the stopping power although the change of the energy of the ion is negative. The stopping power has contributions of energy loss due to inelastic interactions with electrons of the target, due to elastic interactions with the nuclei of the target and due to radiative processes, so-called Bremsstrahlung (see Figure 2.1).

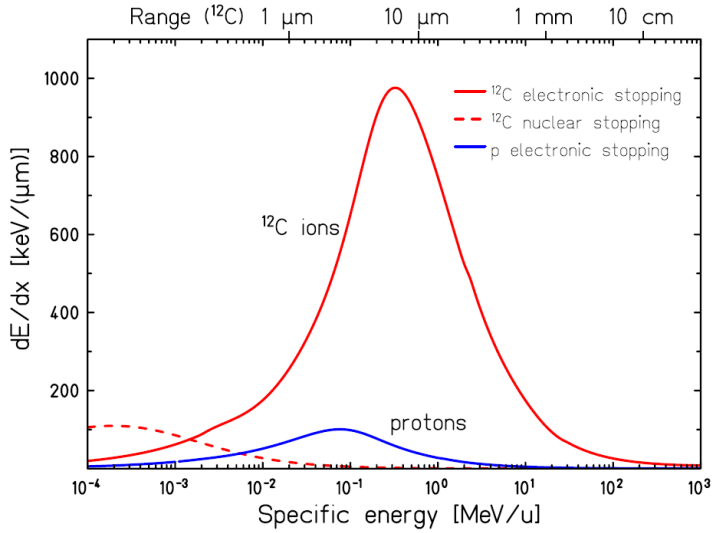

Figure 2.1. Stopping power of carbon ions and protons in water as a function of energy. Reprinted from Schardt et al, 2010.

The elastic interactions with target nuclei at low ion energies of 10 keV/n is only present at the very last few µm of the carbon-ion range. Bremsstrahlung of ions is also negligible for energies up to several GeV/n, because of the much larger mass of the ion with respect to the electron mass [Zyla et al, 2020]. Hence, for ion energies used in radiotherapy reaching up to several hundred MeV/n up to 240 MeV/n, in the irradiation performed in this thesis, energy loss is mainly caused by electronic interactions. The electronic stopping power (S_{elec}) is described by equation 2.2, well-known as the Bethe-Bloch equation [Bethe, 1930; Bloch, 1933; Fano, 1963; Zeitling et al, 2007]:

$$S_{elec} = -\frac{2\pi e^4}{m_e c^2} N_A \frac{Z}{A} \frac{z^2}{\beta^2} \rho \left[2ln\left(\frac{2m_e c^2 \beta^2}{I(1-\beta^2)} \right) - 2\beta^2 - \delta - 2\frac{C}{Z} \right], \tag{2.2}$$

where m_e and e are the electron mass and charge, $\beta = v/c$, where v stands for the velocity of the ion and c for the speed of light and. The nuclear charges of the ion and the target are z and Z, respectively, N_A is the Avogadro's number, A and ρ is the atomic weight and the density of the target, respectively. I stands for the mean ionization energy of the

target. The last two terms indicate the shell effect ($2C/Z$) and the density effect (δ) corrections. The former term corrects for the ion velocity that is assumed to be much higher than that of the orbital electrons in the atom. The latter term corrects for polarization effects that appears in the trajectory of the ion due to dielectric target's properties. From equation 2.2, it is clearly seen, that the energy loss increases while decreasing the velocity of the ion. This is indicated as the $1/\beta^2$ dependence.

When using therapeutic ion energies, which implies non-relativistic energies, β is approximated as a function of the energy per nucleon of the incident ions (E_n), given by equation 2.3:

$$\bar{E} = \frac{E}{A} \tag{2.3}$$

where A is the atomic weight and E is the energy of the incident ion. From this, the stopping power of an ion in human tissue can be expressed in terms of the stopping power of a proton, as indicated in equation 2.4 [Schlegel and Bille, 2002]:

$$S_i(E_n) \approx z_i^2 S_p(E_n/A), \tag{2.4}$$

where S_p is the stopping power of a proton and z_i is the charge of the ion. Knowing the ion stopping power, another important characteristic of ion beams can be calculated. The mean ion range (R) is defined as the mean traveled path length before the ion stops inside a medium. The range of ion in matter can, therefore, be determined as the integral of the inverted stopping power over the beam energy, from E = 0 MeV/n to $E = E_0$, being the initial energy. This is expressed by equation 2.5:

$$R_{CSDA} = \int_{E_0}^{0} \left(\frac{dE}{dx}\right)^{-1} dE, \tag{2.5}$$

where R_{CSDA} stands for the ion range in the continuous slowing down approximation range. Examples of ion ranges for different ion types in water are depicted in Figure 2.2.

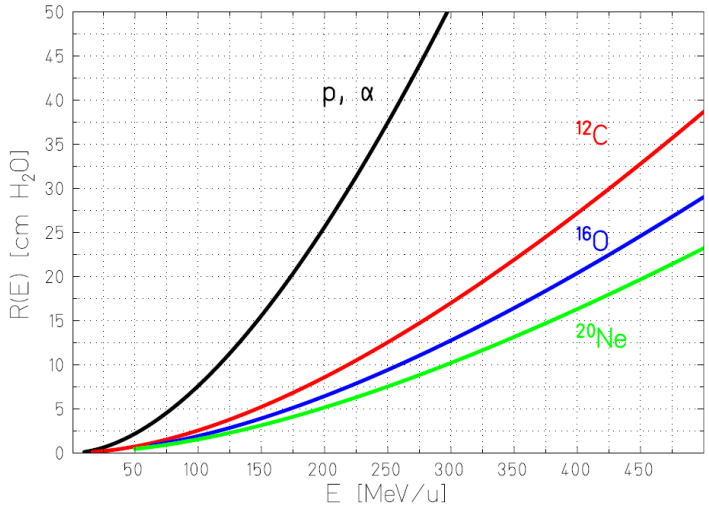

Figure 2.2. Ion ranges for different ions in water. Reprinted from Schardt et al, 2010.

2.1.2. Straggling of energy loss and of range

While losing energy, ions are slowing down until rest. It is at the end of their path where the maximum energy deposition takes place, which is well known as Bragg peak. Although the equation 2.2 is describing the energy loss of ions in a material, there are statistical fluctuations of the energy loss, the so-called energy loss straggling, affecting the Bragg peak. Such fluctuations can be described by the Vavilov distribution (Vavilov, 1957). It has to be pointed out, that the energy loss depends on the number of ion interactions within the material. From here, a discriminating parameter k is introduced and defined as the ratio of the mean energy loss of the incident ion (ΔE) and the maximum energy transferred in a single collision (E_{max}), as indicated in equation 2.6:

$$k = \frac{\overline{\Delta E}}{E_{max}}. \tag{2.6}$$

Ignoring the logarithmic term in equation 2.2, the mean energy loss (ΔE) can be approximated by the equation 2.7 (Leo, 1994):

$$\overline{\Delta E} = 0.1535 \frac{MeV cm^2}{g} \frac{Z}{A} \frac{z^2}{\beta^2} \rho x, \tag{2.7}$$

where A is the atomic weight, and ρ and x are the density and the thickness of the material in units of g/cm^3 and cm, respectively. The maximum energy transferred in a single collision is given by the equation 2.8 (Leo, 1994):

$$E_{max} = \frac{2m_e c^2}{1 + 2\left(\frac{m_e}{M}\right)} \frac{(\beta\gamma)^2}{\sqrt{1 + (\beta\gamma)^2} + \left(\frac{m_e}{M}\right)^2}, \tag{2.8}$$

where M is the mass of the incident ion and $\gamma = 1/\sqrt{1 - \beta^2}$. For discriminating parameter $k \leq 10$, the material is considered thin, and for $k > 10$ the material is thick. If this is the case ($k > 10$), the statistical fluctuations described by the Vavilov distribution can be approximated by a Gaussian distributions expressed in the equation 2.9 (Leo, 1994):

$$f(\Delta E) = \frac{1}{\sqrt{2\pi}\sigma} e^{(\Delta E - \overline{\Delta E})^2 / 2\sigma^2}, \tag{2.9}$$

where ΔE in the energy loss, $\overline{\Delta E}$ is the mean energy loss and σ is the standard deviation of the distribution. In the case of therapeutic ions (e.g. carbon ions with energies up to 430 MeV/n, corresponding to a velocity of $\beta \leq 0.7$), the standard deviation σ is approximately proportional to the thickness x, density ρ, atomic number Z and atomic weight A of the irradiated material.

The energy loss straggling directly leads to variations of the range, known as range straggling. The direct variance of the range straggling (σ_R^2) is given by equation 2.10:

$$\sigma_R^2 = \int_0^{E_0} \left(\frac{d\sigma}{dx}\right) \left(\frac{dE}{dx}\right)^{-3} dE, \tag{2.10}$$

where σ is the variance of the energy loss straggling. Nevertheless, the heavier the ion, the less is the range straggling, because of the inverse dependence on the mass of the ion M, as seen in the equation 2.11.

$$\frac{\sigma_R}{R} \propto \frac{1}{\sqrt{M}}. \tag{2.11}$$

This is the cause of a narrower Bragg peak as observed in Figure 2.3, in particular for carbon ions.

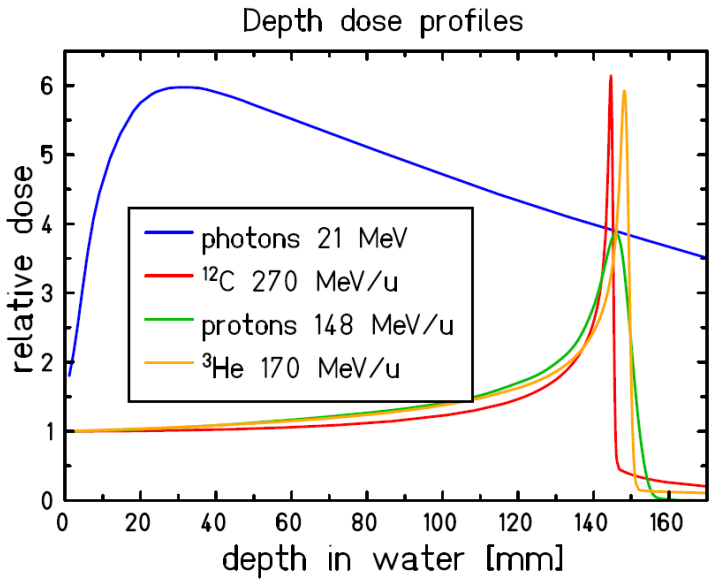

Figure 2.3 Bragg peaks of protons (green curve), helium ions (orange curve) and carbon ions (red curve) in comparison to photons (blue curve). It is seen, that the heavier the ion the sharper the Bragg peak. Adapted from Krämer et al, 2016.

2.1.3. Lateral scattering

Ions undergo Coulomb interactions with the nuclei of the target (e.g., human tissue), causing small deflections that result in the well-known multiple Coulomb scattering (MCS). This effect produces a broadening of the ion beam in the lateral directions. The Coulomb scattering is described by the Molière theory [Molière, 1948], for small scattering angles of multiple interactions. However, for larger scattering angles, the resulting distribution is more similar to that from the Rutherford scattering. An approximation can be done for small scattering angles, resulting in a Gaussian function, where its standard deviation (σ) is given by equation 2.12 [Highland, 1975]:

$$\sigma[rad] = 14.1MeV\frac{z}{p\beta c}\sqrt{\frac{d}{L}}\left[1+\frac{1}{9}log_{10}\left(\frac{d}{L}\right)\right]. \tag{2.12}$$

Here, p, βc and z stand for the momentum, the velocity and the charge of the incident ion, respectively, d is the penetration depth and L is radiation length of the target material. In this equation it is assumed, that the momentum and velocity are constant, i.e., it is only valid for the crossing of thin materials.

From equation 2.12, the heavier the incident ion is, the smaller the lateral scattering. An example of this can be seen in Figure 2.4. Comparing protons and carbon ions with the

same range in water, protons spread by a factor of three to four more than the carbon ions.

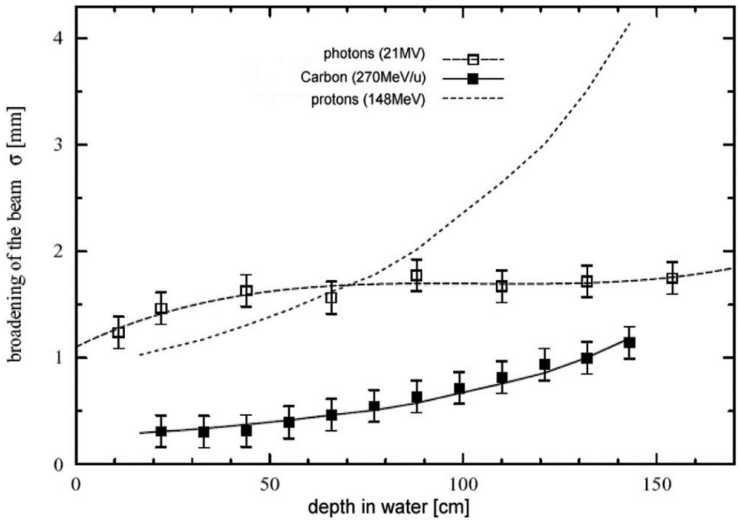

Figure 2.4. Lateral scattering for proton and carbon-ion beams in comparison to X-ray radiation as a function of depth in water. Reprinted from Jäkel, 2009.

Moreover, targets with high-charge elements cause larger angular spreads in contrast to those with low-charge elements [Schardt et al, 2010]. For targets with inhomogeneities, even small angular deflections can lead to undesirable range straggling.

2.1.4. Nuclear fragmentation

Besides the energy loss and scattering, incident ions undergo nuclear fragmentation processes while traversing human tissue or any other material in interactions with target nuclei. Here, the kinetic energy of the ion exceeds the Coulomb barrier, producing such inelastic interactions. The most frequent interactions are the peripheral interactions due to geometrical reasons [Gunzert-Marx et al, 2008; Schardt et al, 2010; Kraan, 2015].

Nuclear fragmentation depends on many factors, such as energy and charge of the incident ions, as well as thickness and chemical composition of the target material. In the nuclear fragmentation process, other particles known as secondary charged fragments are produced. These secondary fragments are forward directed and their production typically increases as the penetration depth of incident ions increases. The produced fragments are lighter than the incident ions, but have similar velocities, thus secondary fragment range is longer with respect to that of the incident ions. This leads to a characteristic fragment tail located behind the Bragg peak.

Moreover, secondary fragments can, in turn, undergo more fragmentation processes. From this, the advantages reached by ions in radiotherapy may be impaired due to these

secondary charged fragments (called secondary ions from hereon, and this terminology also includes protons). Figure 2.5 shows the so-called fragment tail behind the Bragg peak.

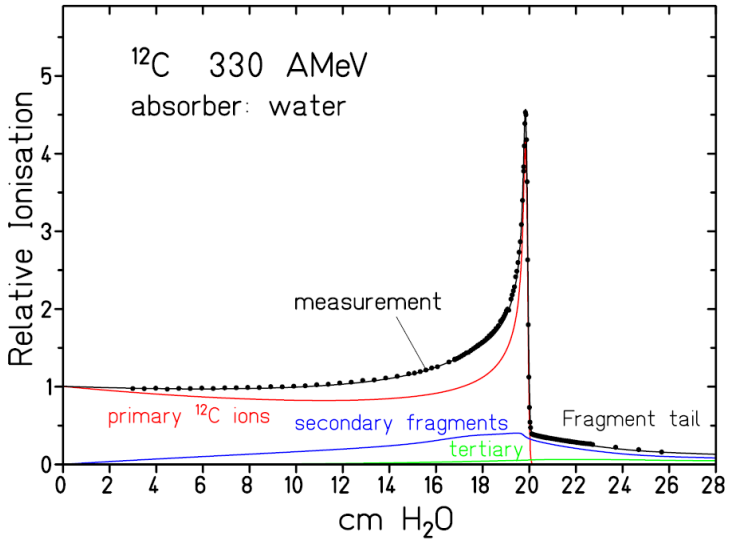

Figure 2.5. Bragg curve of carbon ions in water. The fragment tail appears due to the forward-peaked directions of the produced secondary ions. The contribution to only carbon ions is shown by the red curve. Contributions due to secondary (blue curve) and tertiary (green curve) fragments are shown. The total energy deposition is indicated by the black curve. Reprinted from Schardt, 2007.

Abrasion-ablation model

Nuclear fragmentation processes are described by the so-called abrasion-ablation model [Serber, 1947; Gaimard and Schmidt, 1965; Hüfner et al, 1975], as depicted in Figure 2.6. This model is a nucleus-nucleus interaction, when irradiating a human tissue, for example, with carbon ions.

In the interaction between the incident ion and the target nucleus, there is an overlapping region of nucleons from the ion and the nucleus. These overlapping nucleons are sheared off in an excited state. This process is the so-called abrasion (see central image in Figure 2.6), which lasts between 10^{-22} to 10^{-23} s, approximately. It has to be pointed out, that fragments have masses and charges smaller than the incident ion and target nuclei. Moreover, nucleons not involved in the overlapping region are slightly affected, and are fragments with a similar velocity and direction of the incident ions. Since they are lighter, they can reach larger ranges than the incident ions due to the dependence of the range on A/Z^2.

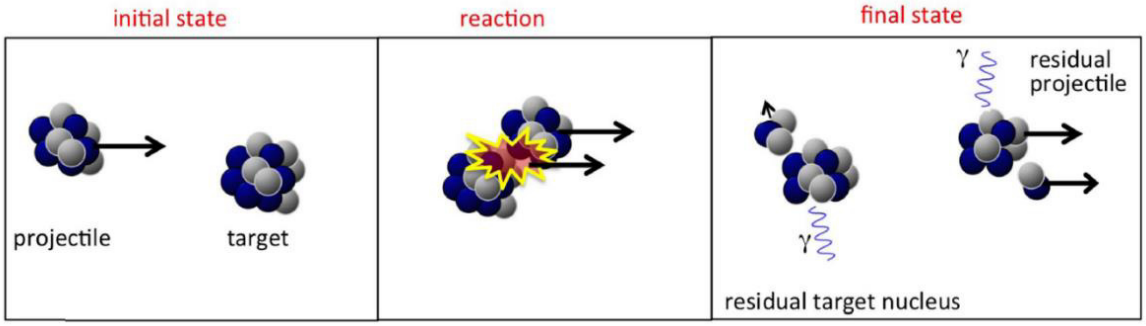

Figure 2.6. Illustration of a nucleus-nucleus interaction, e.g., a carbon ion as projectile and a nucleus of human tissue as target. After the interaction, secondary ions from both projectile and target are produced. When some secondary ions are de-excited, they can also emit photons. Reprinted and modified from Kraan, 2015.

Subsequently to the abrasion process, the remaining fragments experience de-excitation while evaporating lighter nuclei. This process is the so-called ablation and lasts between 10^{-18} to 10^{-16} s, approximately (see right image in Figure 2.6). Fragments from target nuclei may not leave the material and they can emit isotropically photons and even nucleons with lower velocities when de-excitation occurs to reach the ground state [Zeitlin and La Tessa, 2016]. Because of their low velocity, such nucleons can only locally deposit energy in the vicinity of the secondary-ion creation location.

Nuclear fragmentation cross-section of carbon ions

As the nuclear fragmentation is due to nucleus-nucleus interaction, the total cross section comprises the probability of such interactions. In general, the total cross section (σ_T) is the contribution of the elastic cross section of the incident ion and the inelastic nuclear reaction cross section. However, measuring directly the latter is challenging. For this, other quantities are measured as an appropriate estimation of the nuclear reaction cross section: charge-changing cross section and mass-changing cross section [Horst, 2019]. The former is related to the proton loss of the incident ions, whereas the latter is related to the nucleon loss. The partial charge-changing cross section (σ_{PCC}) is the parameter related to the fragment production from incident ions [Golovchenko et al, 2002]. For carbon-ion irradiations of water, experimental results have shown a constant behavior of σ_{PCC} in the range of therapeutic energies [Toshito et al 2007]. Figure 2.77 shows the partial charge-changing cross section of carbon ions irradiated on water. For the range of the therapeutic carbon-ion beam energies, as used in this thesis (see section 3.2), the cross section of carbon ions shows a constant behavior.

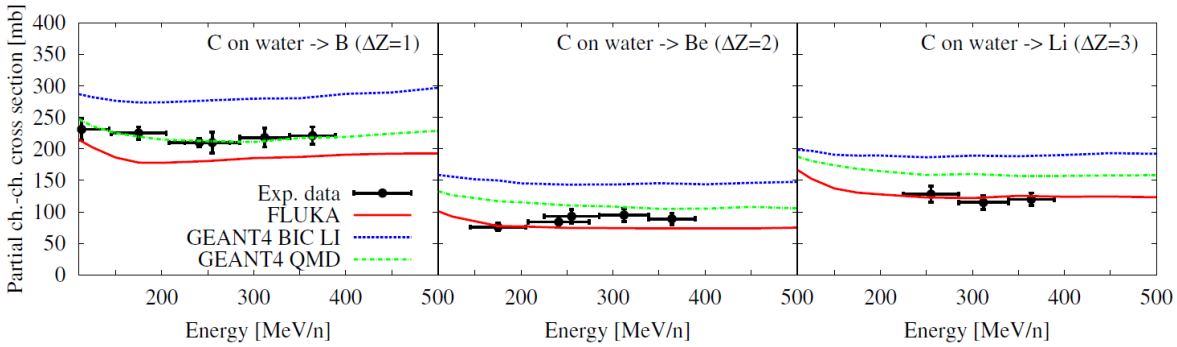

Figure 2.7. Partial charge-changing cross sections of carbon ions irradiated on water for change difference of Boron (left), Beryllium (center) and Lithium (right). Experimental data are compared with results from Monte Carlo simulations using FLUKA and GEANT4. Reprinted from Böhlen et al, 2010.

2.2. Physical advantages of carbon-ion beam radiotherapy

For each physical interaction explained in section 2.1, the consequences for the applications of carbon-ion beams in radiation therapy are described. An important physical quantity used in radiotherapy is the so-called absorbed dose in tissue (D), defined as the mean of the imparted energy by the ionizing radiation per mass unit at a specific point [ICRU85, 2011] given in Gray (Gy) units, as indicated in equation 2.13:

$$D\ [Gy] = \frac{d\bar{\varepsilon}\ [J]}{dm\ [kg]}, \tag{2.13}$$

where $d\bar{\varepsilon}$ is the energy deposited by the type of irradiation (e.g., photons or ions) in a mass element dm. For irradiations with ions, the absorbed dose can be also given by equation 2.14:

$$D\ [Gy] = 1.602 \times 10^{-9} \varphi \left[\frac{1}{cm}\right] \cdot \frac{dE}{dx}\left[\frac{MeV}{cm}\right] \cdot \frac{1}{\rho}\left[\frac{cm^3}{g}\right], \tag{2.14}$$

where φ is the fluence of incident ions, ρ is the mass density of the irradiated material and dE/dx is the stopping power of the ions.

In radiation therapy with ions, the Bragg peak described in section 2.1.2 and shown in Figure 2.3 shows a distal fall-off of the absorbed dose. This fall-off can be used for a better sparing of healthy tissue and organs at risk that surrounds the tumor region, in comparison to the conventional radiotherapy with photons. Moreover, several Bragg peaks can be superimposed in depth by varying the initial energy of the ion. This creates

a spread-out Bragg peak (SOBP) to cover the whole tumor region, leading to a better dose distribution, as shown in Figure 2.8.

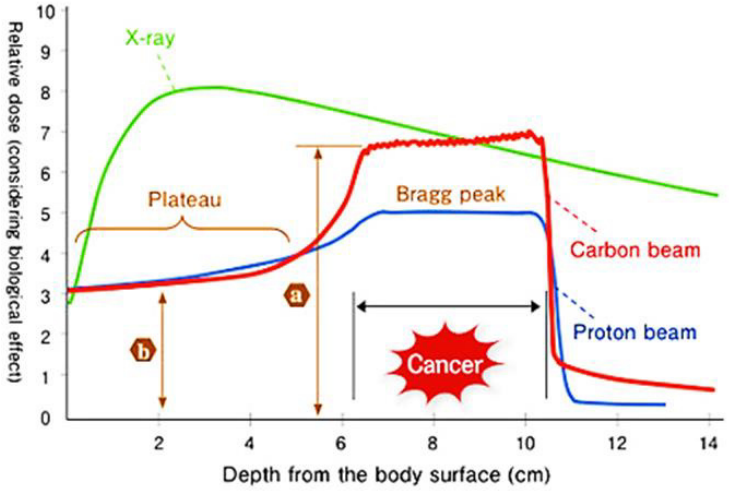

Figure 2.8. Comparison of dose-deposition curves with X-rays (green curve), protons (blue curve) and carbon ions (red curve). The SOBP is shown for proton and carbon-ion curves, covering the region where the cancer tumor is. Almost no dose is deposited after the tumor region. The values a and b are related to lethal and sub-lethal damage of cancer cells, respectively. Taken and modified from http://www.teambest.in/particle-therapy/index.html

As aforementioned, ions stop inside matter (e.g. human tissue). In the field of cancer therapy, this physical characteristic of the ions is used to tailor the distribution of radiation dose to the tumor volume, and to spare healthy tissue and critical organs surrounding the tumor. The Bragg peak positions and depths is adjusted by changing the incident ion direction and energy, and, in this manner, the tumor volume receives the entire dose prescribed by the oncologist.

The dose distribution can be affected by the range straggling. As mentioned in section 2.1.2, carbon ions exhibit less range straggling in comparison to that for protons due to the $1/\sqrt{M}$ dependence indicated in equation 2.11 [Linz, 2012]. Figure 2.9 shows the difference between carbon ions and protons concerning the range straggling.

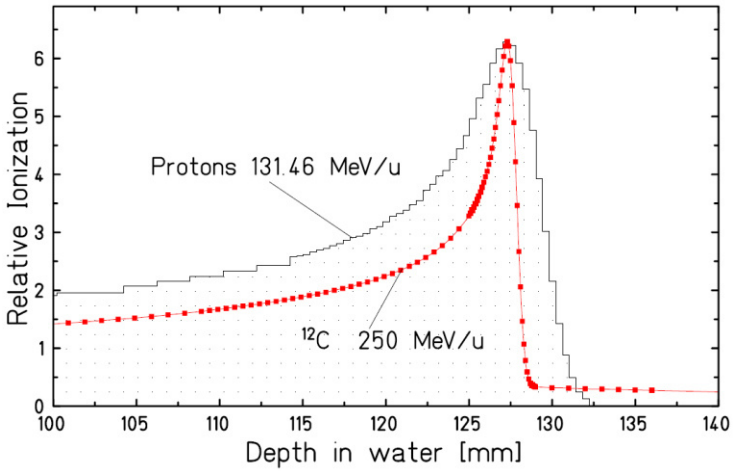

Figure 2.9. Bragg peaks of carbon-ion and proton beams with the same range in water. Range straggling is shown to be smaller for the carbon-ion beam than for proton beam. Reprinted from Schardt et al, 2010.

Carbon ions show advantages as less multiple Coulomb scattering and narrower lateral penumbra compared to protons [Weber and Kraft, 2009; Uhl et al, 2014]. Figure 2.10 shows the different lateral penumbras of a carbon-ion and proton beam.

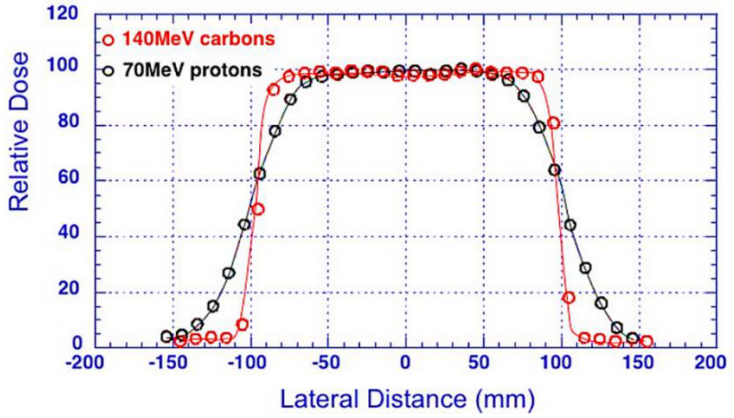

Figure 2.10. Shaper penumbra of carbon ions than penumbra of protons. Reprinted from Chu, 2006.

Moreover, as carbon ions are heavier than protons, there is less scattering inside the beam nozzle and in the patient [Schardt et al, 2010]. However, when targets with inhomogeneities are irradiated with carbon ions, even small angular scattering can lead to undesirable range straggling, which might cause under-dosage in the tumor volume or over-dosage in the healthy tissue and critical organs surrounding the tumor.

2.3. Beam monitoring of nuclear fragmentation

Nuclear fragmentation processes not only have disadvantages (e.g., extra dose deposition behind the Bragg peak). Secondary product of the nuclear processes, i.e., positron-emitting isotopes, prompt gamma rays and prompt secondary charged fragments (among them secondary ions), can also be detected and used for the verification of the ion range and the monitoring of lateral positions of the ion beam inside a patient.

Positron emission tomography

The most common verification of the ion ranges lies on the usage of positron emission tomography (PET). During the fragmentation process, radioactive isotopes (e.g., ^{15}O, ^{13}N, ^{11}C and ^{10}C) are generated, and they can emit positrons that annihilate with electrons in the material, producing two opposite gamma rays of 0.511 MeV each detected by scintillator detectors. This process is dependent of the half-life of the produces isotopes, which goes from few milliseconds up to tens of minutes. Thus, PET can produce functional 3D images that are used to verify the trajectory path of the ion [Enghardt et al, 2004; Min et al, 2013; Ferrero et al, 2018; Bisogni, 2019]. This technique was the first to be clinically implemented.

Prompt gamma rays

Another technique to verify the ion range is based on the detection of prompt gamma rays. Prompt gamma rays are due to excited states of the secondary ions produced during nuclear fragmentation. In order for the secondary ions to reach the ground state, they de-excite by emitting prompt gamma rays, which can be also detected by scintillator detectors. This technique has been also clinically used in proton beam therapy [Richter et al, 2016; Xie et al, 2017; Hueso-González et al. 2018]. Currently, prompt gamma are being detected in the frame of prompt gamma spectroscopy for verification of absolute ion range in carbon-ion beam therapy [Dal Bello et al, 2020; Magalhaes Martins, et al, 2020].

Secondary ions

Secondary ions produced during nuclear fragmentation processes, being energetic enough, can emerge from the irradiated object. Some low energetic secondary ions deposit their energy inside the material, for instance, a patient treated with carbon ions, contributing to the prescribed dose in a treatment. Studies have shown that the contribution of secondary ions to the dose-to-water depositions is about 14% and 13%, for protons and helium, respectively, being the most produced fragments; whereas the contribution of lithium, beryllium and boron is about 1.7%, 1.3% and 4.2%, respectively

[Francis et al, 2014]. Secondary ions with a linear energy transfer smaller than 100 keV/µm have the major contribution to the dose [Johnson et al, 2015].

Simulation-based and experimental studies on the angular distribution of secondary ions generated by carbon-ion beams have been also carried out [Matsufuji et al, 2005; Gunzert-Marx et al, 2008; Robert et al, 2013], which shows the angular distribution of such secondary ions getting narrower when the nuclear charge of the secondary ions increases (forward-peaked directions) [Haettner et al, 2013].

Figure 2.11 shows the angular distribution of the secondary ions produced by a 400-MeV/n carbon-ion beam irradiating a water phantom. Protons can still be detected at detection angles larger than 10°. Thus, when placing detectors at 30° with respect to the beam direction, the detected secondary ions are mainly protons [Haettner et al, 2013; Reinhart et al, 2017]. This detector-positioning angle has been employed in studies performed in our research group [Gwosch et al, 2013; Gaa et al, 2017; Félix-Bautista et al, 2019]. In the current thesis not only the detection-positioning angle at 30° was used, but also at 0° with respect to the beam direction. As expected, heavier secondary ions up to boron are also detected at 0° [Aricò et al, 2019].

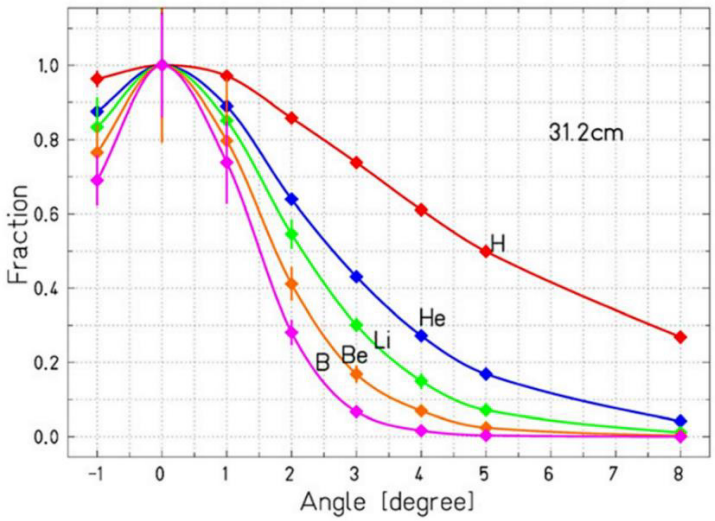

Figure 2.11. Angular distributions of secondary ions (Z = 1 to 5) produced by carbon ions of 400MeV/n irradiated in a water phantom of 31.2 cm thick. Reprinted and modified from Haettner et al, 2013.

Secondary ions have also been used for ion range verification [Dauvergne et al, 2009; Amaldi et al, 2010]. The distribution of the secondary ions along the beam direction has been studied and correlated with the position of the Beagg peak [Henriquet et al, 2012; Piersanti et al, 2014; Rucinski et al, 2018]. Recently, a trial study started using a dual-mode system for the ion beam monitoring in carbon-ion beam therapy within the INSIDE collaboration in July 2019 [Bisogni, 2019; Traini et al, 2019; Fischetti et al, 2020]. In this study, both PET- and secondary-ion-based techniques are used.

Additionally, not only the ion range, but also the lateral pencil beam positions in a clinic-like treatment delivery with carbon ions has been monitored [Gwosch et al, 2013; Félix-Bautista et al, 2019]. In December 2019, the first beam monitoring based on the detection of secondary ions using pixel semiconductor detectors has been clinically tested at the Heidelberg Ion-Beam Therapy Center in Heidelberg, Germany. Lateral positions of the ion beams and range verification were both assessed. The results of this clinical application are shown in the current thesis.

2.4. Radiobiology of ion beams in radiation therapy

2.4.1. Linear energy transfer

As briefly described in section 2.1.2, ion beams exhibit highly localized energy deposition (i.e., deposited energy in tissue), which is one of the main physical advantage of using ion beams in radiation therapy. The reason for the higher comformality of dose to the tumor compared to photon radiotherapy is that the density of ionizations strongly increases towards the end of the range of the ion, i.e., within the tumor volume after successful treatment planning. The density of ionizations around the ion tracks, or in other words, the scale of the localization of energy depositions can be described by a physical concept called linear energy transfer (LET), which is related to the radiation quality. LET is defined as the energy transferred (dE) by the incident ion to generated electrons in a path length (dl) in the irradiated material, and it is given by the equation 2.15:

$$LET = \frac{dE}{dl}. \tag{2.15}$$

However, a restriction to consider only generated electrons below a certain energy is usually introduced, and LET is known as restricted LET (LET_{Δ}). This restricted LET gives information about the ionization on a microscopic level around the path of the ion, in a cylindrical volume. In other words, delta electrons traveling further and leaving the volume defined by, e.g., a 100 μm radius around the path of the ion are neglected [Krämer and Kraft, 1994a and 1994b]. The unrestricted LET, i.e., $LET_{\Delta=\infty}$, is the stopping power (S) (see section 2.1.1).

2.4.2. Biological concepts of modeling the repair mechanisms of cells

As the aim of cancer therapy treatments is to eradicate the tumor cells avoiding complications in healthy tissue, LET plays an important role in the evaluation of the biological damages caused by ions. Both the dose depositions and the radiation quality contribute to the cell damage on a microscopic scale. The density of cell damage depends on the

amount of energy transfer, i.e., on the LET. High-LET particles (such as ions) can produce densely damage in the DNA strands, as shown in Figure 2.12.

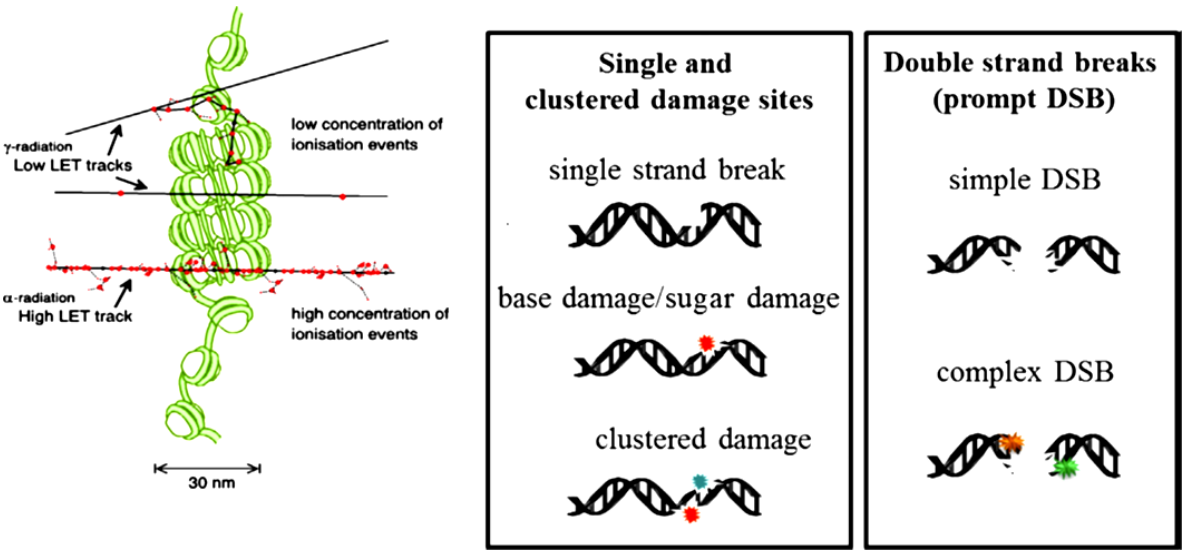

Figure 2.12. Representation of DNA damage caused by low- and high-LET radiation. They create single and double strand breaks. DNA repair mechanisms are less efficient in repairing clustered damage or double strand breaks, leading to increased cell death, compared to single strand breaks or damages of DNA bases. Reprinted from Lomax et al, 2013.

After irradiation, DNA single- (SSB) and double-strand breaks (DSB), base damages and DNA-protein cross-links are produced [Hagiwara et al, 2019]. Following DNA damage, different DNA repair mechanisms are put in place in the irradiated cells [Wozny et al, 2020]. However, complex DSBs or clustered SSBs are more difficult to repair, leading to increased cell death. The potential of cell repair is described by the equation 2.16, which is known as the cell survival probability (S) or linear-quadratic model (see Figure 2.13):

$$S(D) = e^{-(\alpha D + \beta D^2)}, \tag{2.16}$$

where D is the absorbed dose, and α and β are parameters that depend on the cell type. The ratio of these parameters is of great interest. Cells have less capacity for damage repair when the ratio α/β is small, and vice versa.

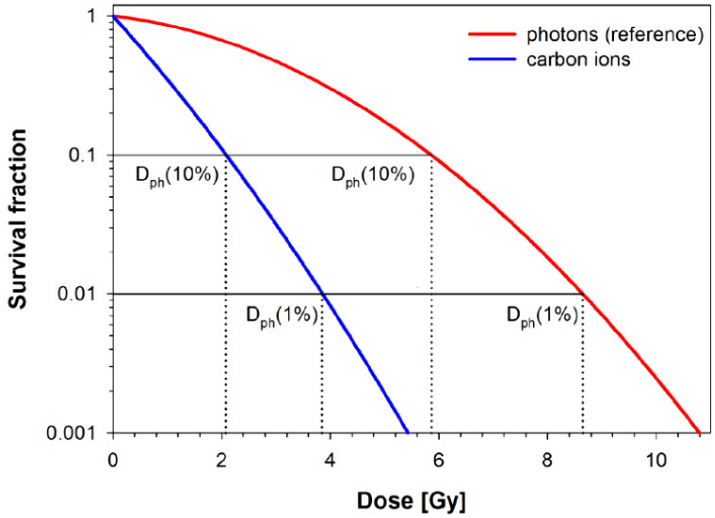

Figure 2.13. Survival fractions according to two different irradiation types: photons (red curve) and carbon ions (blue curve). Modified from Karger and Peschke, 2018.

2.4.3. Relative biological effectiveness

To evaluate the effectiveness of ions compared to photon irradiations, the concept of relative biological effectiveness (*RBE*) is introduced. *RBE* is defined as the ratio of a photon (D_{photon}) and an ion (D_{ion}) doses (see Figure 2.13), which give the same biological effect under identical conditions [Karger and Peschke, 2018], described by equation 2.17:

$$RBE = \frac{D_{photon}}{D_{ion}}\Big|_{isoeffect} . \tag{2.17}$$

This is valid for the same number of fractions of a treatment. Cell death and complications of healthy tissue can be described by the *RBE*. This *RBE* depends on different parameters such as ion type, beam quality, absorbed dose, cell cycle, tumor oxygenation, and biological endpoint, among others [Karger and Peschke, 2018].

RBE also has a dependence on LET. As LET increases for ions towards the end of their range. High-LET leads to an increase of the biological effectiveness. Therefore, the biological effectiveness increases towards the end of the ion range, e.g., inside the tumor. Thus, *RBE* increases until an optimum LET (maximum) value. However, *RBE* starts decreasing after the maximum value for higher LET values. This means, that there is a higher dose concentration that cannot cause additional cell damage. This effect is called overkill effect. Figure 2.14 shows LET and *RBE* values for different ion types.

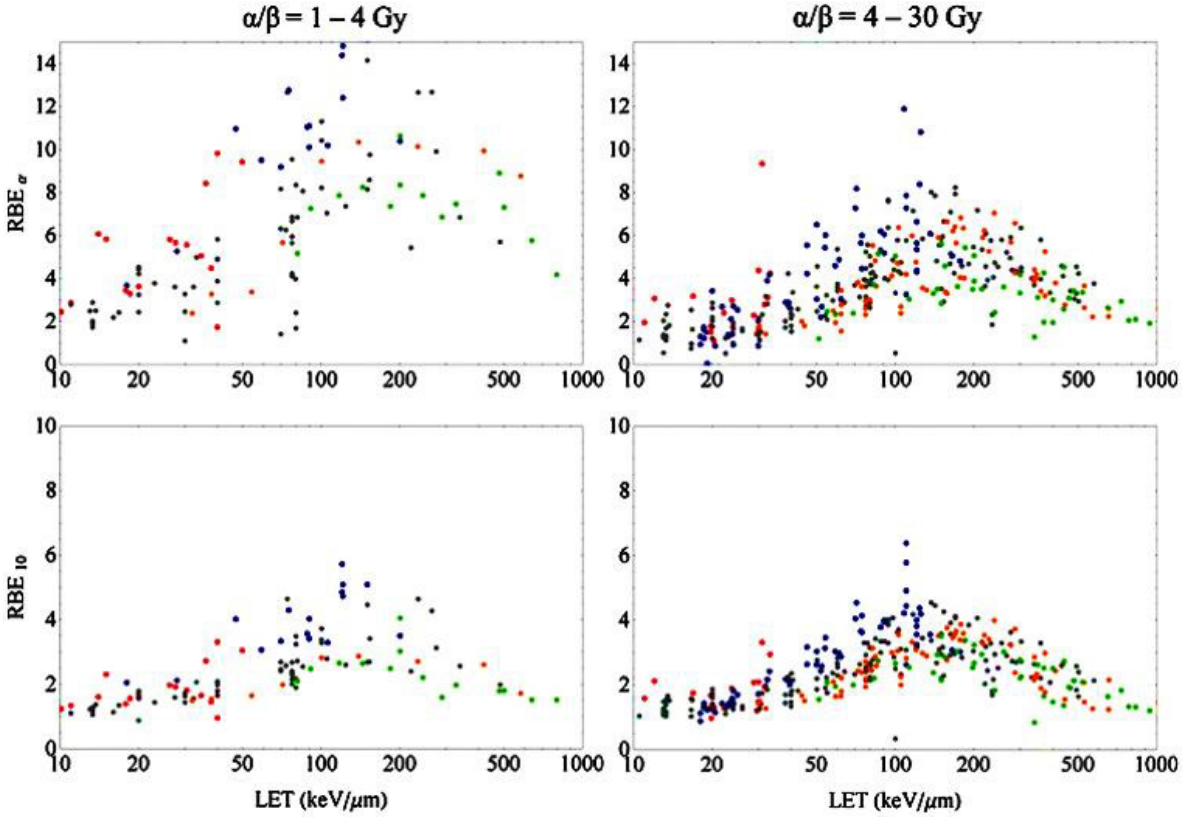

Figure 2.14. LET-dependence *RBE* for different α/β values and different ions: protons (red points), helium (blue points), carbon (gray points), neon (orange points), ions heavier than neon (green points). LET-dependence at full survival level is shown in the upper row, whereas the 10% survival level is shown in the lower row. The overkilling region (after the maximum) is shown. Reprinted from Friedrich et al, 2013.

RBE has been studied for carbon ions irradiations, showing great potential over protons and photons to be used for having higher response when treating hypoxic and heterogeneous tumors [Glowa et al, 2016; Glowa et al, 2017; Mein et al 2019]. Moreover, the prescribed dose for carbon-ion treatments is given in terms of *RBE*-weighted dose instead of absorbed dose. For that, models of *RBE*-weighted dose have to be considered. However, the modelling of *RBE*-weighted dose is not straightforward, due to dependences on the aforementioned physical and biological parameters aforementioned. The most used model at the carbon-ion facilities in Europe is the so-called local effect model developed at the Gesellschaft für Schwerionenforschung in Darmstadt, Germany [Scholz and Kraft, 1992, 1994, 1996]. Other *RBE* models are the mixed-beam model and the microdosimetric-kinetic model, both used at carbon-ion facilities in Japan [Kanai et al, 1997; Kanai et al, 1999; Kase et al, 2006; Inaniwa et al, 2010; Inaniwa et al, 2015]. A very complete review on the *RBE*-weighted dose models and their differences can be found in Karger and Peschke, 2018.

2.5. Cyclotron- and synchrotron-based therapy facilities

In particle therapy, ions have to be accelerated in order to gain enough energy to penetrate the required depth in the patient. For that, either cyclotrons or synchrotrons are needed and built in therapy facilities. Due to their relatively small size, cyclotrons can only accelerate protons to sufficiently large energies for therapy. This type of accelerator is used in most of the therapy facilities around the world. However, heavier ions (e.g., carbon ions) need synchrotrons to be accelerated to energies relevant for clinical applications, i.e., that correspond to ion ranges of several tens of centimeters. Synchrotron accelerators are used in therapy facilities in Germany, Italy, Austria, Japan and China [PTCOG Therapy Facilities].

Cyclotrons exhibit several advantages over synchrotrons related to their fixed radiofrequency and fixed magnetic field to accelerate particles, as well as a less complex operating principle with much less requirements on dynamic fine-tuning in the beam delivery system [Silari, 2011; Farr et al, 2018]. On the other hand, cyclotrons deliver a fixed beam energy, the use of degraders is needed to irradiate the entire tumor region. However, these degraders cause neutron production, leading to extra dose deposited in the patient [Fukumoto, 1995]. As activation is also present, proper degrader materials have to be chosen. Furthermore, since the beam effectivity is approximately 10% due to the energy degradation, the proton fluence is increased in order to reach the prescribed dose [Fukumoto, 1995; Coutrakon, 2007].

In contrast to cyclotrons, synchrotrons do not need energy degraders to produce the SOBP, because they provide variable ion beam energy depending on the upramping process of radiofrequency and magnetic field for the ion acceleration [Silari, 2011; Farr et al, 2018]. A disadvantage of synchrotrons over cyclotrons is their construction and size (about 20 m diameter for synchrotrons and 4.5-5 m for cyclotrons), which impacts on the cost of operation and maintenance [Peeters et al, 2010; Vanderstraeten et al, 2014], especially with superconducting technology [Peach et al, 2011; Farr et al, 2018; Mohamad et al, 2018].

Although the cost-effectivity of carbon-ion treatments (i.e., having a synchrotron) is currently discussed controversially, studies have shown high a cost-effectiveness of carbon-ion treatments for locally recurrent rectal cancer and skull base chordomas [Mobaraki et al, 2010; Sprave et al, 2018].

Additionally, the quality assurance (QA) of the lateral positions of ion beams at the isocenter is more challenging for synchrotrons than for cyclotrons. This is due to uncertainties in the beam delivery itself related to variations in the beam transport lines and in the bending and steering magnets that could be translated in beam misdirection [Farr et al, 2018; Rizzoglio et al, 2020]. If this were not corrected for in QA, it would deteriorate the delivered dose homogeneity to the entire tumor.

As mentioned in section 2.2.2, carbon ions are heavier than protons, there is less scattering in the beam nozzle and in the patient. As a consequence, carbon-ion beams are narrower than proton beams; hence, they are more prone to uncertainties in the lateral positions at the isocenter [Karger et al, 2010], the reference point of patient positioning for treatment.

Moreover, due to the distance in between the beam monitor system inside the beam nozzle and the isocenter, carbon ions have a longer path in air in synchrotron-based facilities than in cyclotron-based facilities. This distance is between 18 cm and 50 cm in proton-only facilities [Gillin et al, 2010; Langner et al, 2017; Yasui et al, 2018; Grevillot et al, 2020]. In contrast, such a distance is about 1 m in synchrotron-based facilities like HIT facility [Jelen et al, 2013; Iwata et al, 2016; Tessonier et al, 2019]. The ~60% difference of the nozzle-to-isocenter distance between cyclotron- and synchrotron-based facilities leads to a more complex extrapolation of the beam positions for synchrotrons. In this case, the two position-measuring devices inside the nozzle (multi-wire proportional chambers) cannot be used for the extrapolation. The extrapolation is performed from the virtual source, assumed to be a point source, in the middle of the deflecting magnets and the positions measured by the BAMS in the nozzle [Félix-Bautista et al, 2021]. The determination of the virtual point source depends on the ion type, beam energy and size, and this leads to an increased complexity in the method.

Although several studies have been published regarding the QA of lateral carbon-ion beam positions with different devices (namely, parallel plate ionization chambers, flat-panel detectors, scintillator detectors or radiochromic films) [Martišíková and Jäkel, 2010; Martišíková et al, 2012; Varasteh Anver et al, 2016; Russo et al, 2017], these devices are placed at the isocenter. Therefore, these devices are not suitable for future online-monitoring approaches. Moreover, verifications of the new designed treatment plans are carried out using water phantoms. Nevertheless, water phantoms do not represent the patient geometry. Hence, verifications are done in an indirect manner.

From this, complementary QA strategies to monitor the lateral positions of carbon-ion beams are of great desire, especially when such strategies can perform the monitoring at the isocenter and deal with the patient geometry. In this thesis, the proposed monitoring methodology takes into account such characteristics.

2.6. Semiconductor detectors

As aforementioned, carbon-ion beams in radiation therapy undergo nuclear fragmentation processes. If the produced secondary ions have enough energy to leave the patient, they can be detected. The type of detectors used in this thesis –a semiconductor detector– to detect the produced secondary ions is described here. This type of detectors has been commonly used in the nuclear and particle physics fields, and provide precise measurements on the position, time and energy of the detected ions [Lutz, 2007]. Silicon

and germanium are the most common elements used in semiconductor detectors. In the current thesis, silicon detectors were used (see section 3.3).

In the electronic configuration of a semiconductor detector, electrons are located at specific sites of the semiconductor lattice structure with a certain energy in the so-called valence band. Electrons can gain sufficient energy to change their sites, leaving a hole in that site and going to the so-called conduction band (see Figure 2.15). Between the valence and conduction band, there is an energy gap called forbidden band. For silicon, this forbidden gap is 1.1 eV [Bertolini and Coche, 1968].

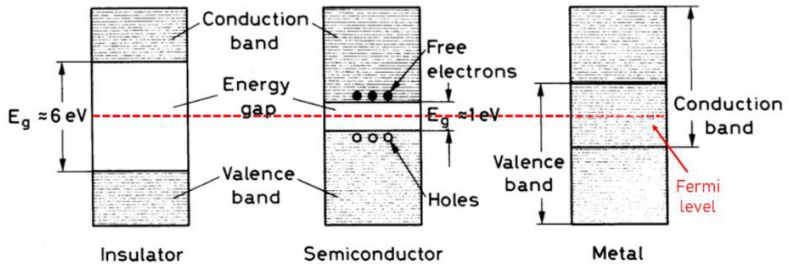

Figure 2.15. Conduction and valence bands in different materials. Modified from Leo, 1994.

Semiconductor materials can be intrinsic –creation of charge carriers by thermally or optically electronic excitation– or extrinsic – creations of charge carriers by impurities at sites in the semiconductor lattice structure–. In the latter, when there are extra electrons due to the impurities, extrinsic semiconductors are called n-type (donor). In contrast, when there are more holes than electrons due to the impurities, extrinsic semiconductors are called p-type (acceptor) [Lutz and Klanner, 2020]. Figure 2.16 exemplifies both p- and n-type extrinsic semiconductors.

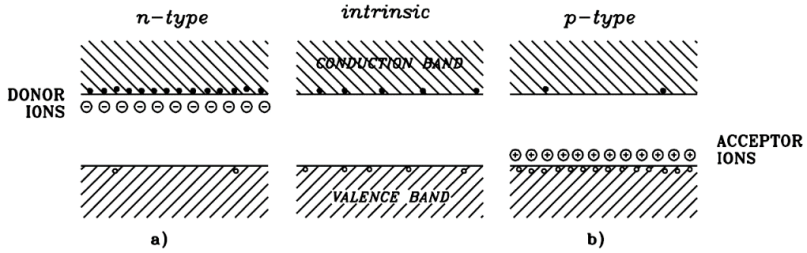

Figure 2.16. Examples of extrinsic a) n- and b) p-type semiconductors. Reprinted from Lutz, 2007.

When a p-type semiconductor is joint to a layer of the opposite semiconductor, e.g., n-type, electrons and holes sweep to the junction zone creating a surplus of negative charge on one side of the junction (p-type side) and positive charge on the other side (n-type side), as seen in Figure 2.17.

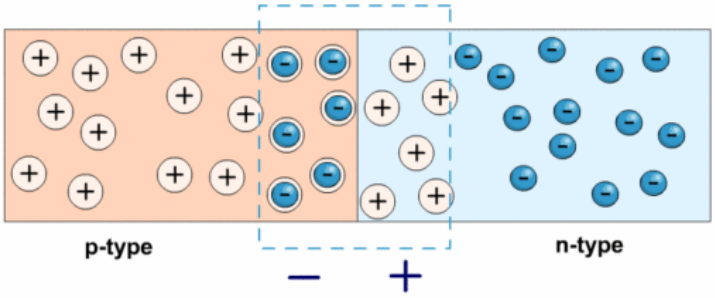

Figure 2.17. Surplus of negative and positive charge in the junction of n-type and p-type semiconductors. Taken and modified from https://electricalacademia.com/electronics/pn-junction-formation-structure/.

Thus, a thermal equilibrium is reached. The thermal equilibrium is given as the probability (f) of energy states (E) at a temperature (T), as expressed by equation 2.20:

$$f(E) = \frac{1}{1 + exp\left(\frac{E - E_f}{kT}\right)}. \tag{2.20}$$

Moreover, the diffusion of electrons and holes in the p-n junction region is counteracted by the presence of an electric field. This electric field creates a space-charge region by sweeping away both electrons and holes in the boundary region of the junction. Such a space-charged region, having two zones of non-zero electric charge, one of filled acceptor sites and other of filled empty donor sites, is so-called depletion region [Leroy and Rancoita, 2011]. When ions interact with the sensitive area of detection, they create electron-hole pairs. In the case of silicon, an energy of 3.6 eV is needed to create a single electron-hole pair [Bertolini and Coche, 1968].

The p-n junction is considered as a diode, to which "forward" of "reverse" bias voltage is applied. In the presence of a reverse bias voltage (which is the case of the used detectors in this thesis), the p-type side of the p-n junction becomes negative relative to the n-type side. Moreover, as this bias voltage increases, so does the depletion region. In this manner, the semiconductor is fully depleted [Knoll, 2010].

The applied bias voltage (V_d) required to deplete a specific thickness (T) is given by equation 2.21:

$$V_d = \frac{eNT^2}{2\epsilon}, \tag{2.21}$$

where e is the electron charge, N is the dopant concentration and ϵ is the dielectric constant of the semiconductor. The sub-index d refers to the depletion voltage.

If the voltage increases beyond the depletion voltage, it is says, that the semiconductor is over-depleted. In the particular case of the silicon semiconductor detectors used in this current thesis, they were not operated fully depleted, but partially depleted, based on previous studies concerning energy depositions in Timepix detectors [Gehrke et al, 2017]. The depletion area was about 200 μm in these detectors when applying a bias voltage of 10 V. The same voltage was used in this thesis for the Timepix3 detectors (see section 3.3). However, further investigations concerning the bias voltage in Timepix3 detectors have to be carried out to optimally operate them either partially or fully depleted.

Secondary ions produced with therapeutic carbon-ion beam energies cross the semiconductor detector, creating a uniform density of electron-hole pairs along their path, traveling with constant velocity [Knoll, 2010]. In order to track such secondary ions, pixel semiconductor detectors are more often used due to their 2D segmentation compared to strip semiconductor detectors. However, they need a large number of readout channels [Seidel, 2019]. In the case of hybrid pixel semiconductors detectors, the electronics is miniaturized, allowing each pixel to have its own readout channel via bump bounds. Timepix3 detectors belongs to this family of detectors. For more details, see section 3.3.

Chapter 3
Materials and Methods

Since this work is based on the detection and tracking of secondary ions produced in deliveries of treatment plans, here is explained the way such delivery is carried out. Ion beam therapy centers around the world are based on cyclotrons or synchrotrons to deliver the ions for treatments. Currently above 100 proton- and carbon-ion-based facilities are in operation and more than 35 facilities are under construction [PTCOG Therapy Facilities]. There are three types of facilities: 92 proton-only, 6 carbon-only and 6 facilities that offer treatments with both protons and carbon ions. Specifically for carbon ions, 12 facilities are in operation for clinical purposes, of which 8 in Asia (Japan and China) and 4 are in Europe (Germany, Austria and Italy). The Heidelberg Ion-Beam Therapy Center (HIT) performs treatments with both proton and carbon ions.

3.1. Heidelberg Ion-Beam Therapy Center

In order to accelerate ions to reach therapeutic energies, both ion accelerator types, namely cyclotrons and synchrotrons can be used for proton-based treatments. However, when treating patients with carbon ions, synchrotrons are needed. In Heidelberg, Germany, patients are treated with protons and carbon ions at the Heidelberg Ion-Beam Therapy Center (HIT). Being a hospital-based ion-beam therapy center, HIT starts clinical operation ate the end of 2009 [Combs et al, 2010]. HIT facility has a synchrotron of 20 m diameter. A LINAC with a length of 6 m pre-accelerates protons, helium, carbon and oxygen ion with an injection energy of 7 MeV/n [Haberer et al, 2004].

HIT facility has four rooms: two rooms have horizontal beam lines, one room is equipped with the first-worldwide carbon-ion rotating gantry (360°) of 600 tons weight, 25 m length and 13 m diameter. Additionally, the fourth room has a horizontal beam line used for quality assurance and research. The experiments performed in this thesis were carried out in this experimental room, since it has a beam quality as the therapeutic

horizontal beam lines. Protons and carbon ions are routinely used for treatments. Helium and oxygen ions are only used for research purposes so far. There have been studies concerning the use of helium ions for treatments [Tessonnier et al, 2017; Mein et al, 2019]. In this thesis, treatment plans for carbon ions were used.

Carbon ions can be accelerated at HIT up to an energy of 430 MeV/n, corresponding to a velocity of about 0.7*c*, and a range of 30 cm in water, at HIT. For such an energy, the beam size ranges from 3.4 mm to 15 mm FWHM at the isocenter. The carbon-ion intensities can attain 10^8 ions per second, but at therapeutic beam energies, the intensities go usually up to 8×10^7 carbon ions per second.

3.1.1. The active raster scanning technique

The ion-beam delivery technique used at HIT was developed at the Gesellschaft für SchwerIonenforschung (GSI) in Darmstadt, Germany, and it is called active raster scanning [Haberer et al, 1993]. The active raster scanning technique involves the continuous movements of the ion beam, being deflected by scanning magnets (see Figure 3.1).

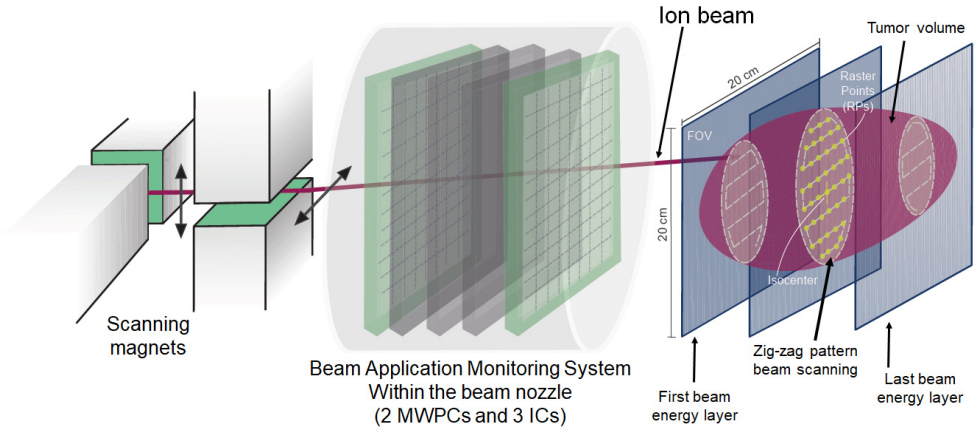

Figure 3.1. Schematic representation of a treatment delivery with ion beams at HIT. The tumor volume is virtually divided into different "slices", equally separated in depth. Scanning magnets deflect the ion beam for a lateral tumor irradiation producing a zig-zag pattern while irradiating a beam energy slice. Adapted from Magallanes-Hernández, Doctoral Dissertation, 2017.

The movement of ion beam follows a zig-zag pattern in the vertical or horizontal direction when irradiating each beam energy layer. However, the beam axis is optimize when treatment tumor volumes with irregular edges [Haberer et al, 1993], as seen in Figure 3.2 (edges in the two blue and green layers). It is observed, that the direction of the ion beam scanning changes vertically and horizontally in the beam energy layers. In the case of the treatment plans used in this thesis (see section 3.3), the spots are equally

separated in both vertical and horizontal directions, i.e., 2 mm. The beam energy layers are separated by 3 mm to each other in depth.

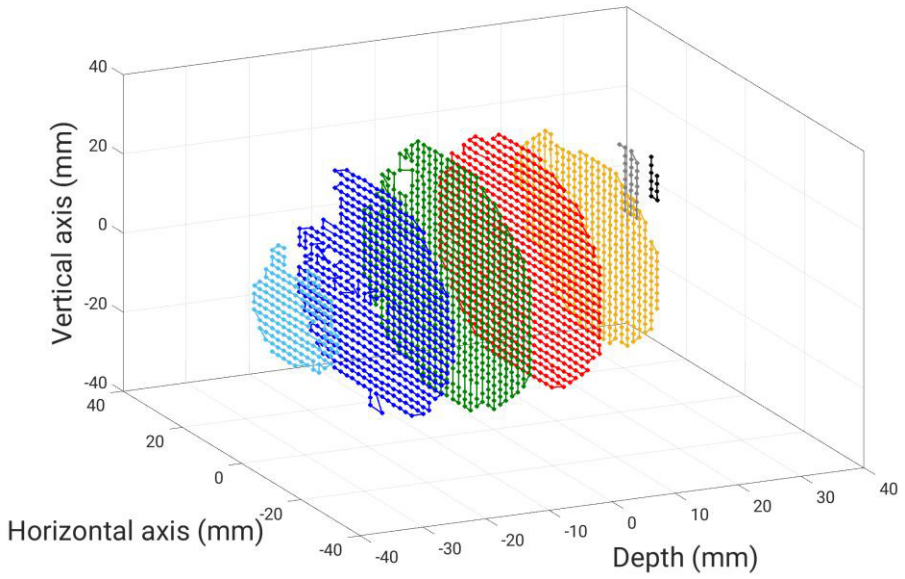

Figure 3.2. Examples of beam energy layers represented in different colors for the spot-by-spot irradiation of a tumor ion depth. These beam energies are taken from the first treatment plan used, as described in section 3.2. Lines connecting the spots represent the direction of the ion beam scanning. This means, that the scanning movement can change vertically and horizontally.

As the beam is not turned on and off during the spot-by-spot irradiation, it is controlled by an intensity-modulated technique allowing a 3D-dose spot delivery (see section 3.1.2). When treating a tumor, it is segmented into virtual slices, called beam energy layers, along the longitudinal direction. Such beam energy layers are equally separated according to the ion beam range along the tumor depth. The ion beam is delivered spot-by-spot covering the beam energy layer. By changing the ion beam energy, the irradiation is carried out layer by layer in order to cover the entire tumor region. The beam movement becomes slow when irradiating at low intensities and higher rates. For irradiations at high intensities and lower rates, the beam moves faster. It has to be pointed out, that the ion beam is continuously on during the irradiation of a beam energy layer. Only when the beam energy is changed, the ion beam is turn off.

3.1.2. Monitoring system at beam nozzle and beam record files

The ion beam is monitoring inside the beam nozzle by means of a Beam Application and Monitoring System (BAMS), consisting of three ionization chamber arrays (ICs) and

two multi-wire proportional chamber arrays (MWPCs) in order to reach the prescribed number of ions per pencil beam and the pencil beam position according to the treatment plan (see Figure 3.1). From the ICs, the ion beam intensity is obtained. The number of ions per spot and the transversal ion beam position are provided by the MWPCs. All this information is registered in the so-called beam record files [Parodi et al, 2012], i.e., two files called physical beam record and machine beam record. In this work for reference data, information concerning the irradiation time and the ion beam intensity of each spot was extracted from the machine beam records. The number of ions per spot and the transversal positions of ion beam spots, taken as reference beam positions, were extracted from the physical beam records.

A third multi-wire proportional chamber (MWPC3) array can be connected to the BAMS and placed at the isocenter in order to monitor the ion beam parameters at that reference point. From this MWPC3, another two beam record files are produced. Measurements at the isocenter are particularly important due to the fact that the tumor volume is centered with respect to the isocenter when positioning the patient by means of a laser alignment system in the treatment room. Moreover, since QA measurements in a water phantom are performed before the first treatment delivery of each patient, the MWPC3 is used when such QA measurements present outliers. Therefore, the monitoring method proposed here can be used as a complementing technique to perform an online QA during the treatment plan delivery. In this thesis, both MWPC2 and MWPC3 were used to obtain the reference beam positions, depending on the performed experiments. For more details, see section 3.4.

This feature of the method, together with the study on the expected stopping positions in the longitudinal direction, make the method stronger and unique to monitor the ion beam in the three space dimensions.

3.2. Treatment plans for the experimental configurations

In order to quantitatively evaluate the performance of the monitoring methodology proposed in this thesis, two carbon-ion treatment plans were used. The treatment plans were designed[2] using the Siemens Syngo RT planning software (Siemens Healthcare GmbH, Erlangen, Germany).

The first treatment plan (TP1) was designed to irradiate a 100-cm^3 tumor volume in the center of an anthropomorphic head phantom (see Figure 3.3 (a)). To treat this volume, one beam field is used with twenty-two carbon-ion beam energies ranging from 163.09 MeV/n to 239.45 MeV/n. Here, more than 10200 spot positions were irradiated and the total number of delivered carbon ions is 7.04×10^8. The spacing of the spot positions in

[2] The treatment plans used in this thesis were provided by Dr. Malte Ellerbrock and Dr. Marcus Winter at the HIT facility.

both X and Y coordinates is 2 mm. The use of an anthropomorphic head phantom enables us to have realistic heterogeneities as the real embedded bony structure. Despite the other materials embedded in the head phantom are not strictly tissue-equivalent materials, this allows us to mimic the treatment delivery in a closer clinical manner.

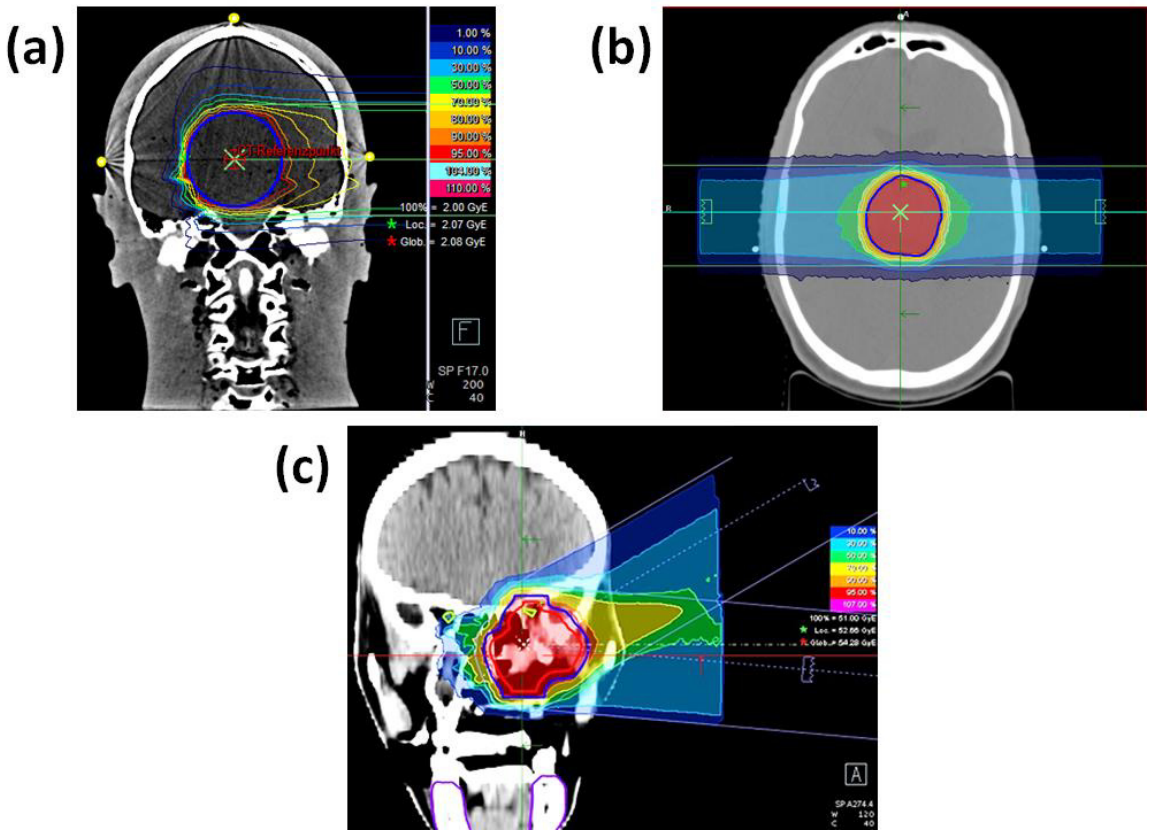

Figure 3.3. (a) Coronal plane of the treatment plan designed for the anthropomorphic head phantom. (b) Axial plane of the treatment plan designed for a real patient. (c) Coronal plane of the treatment plan used in the clinical measurement at HIT. The dose distributions is depicted for all treatment plans. For the RBE-weighted dose, the LEM1 model was used.

The second treatment plan (TP2) was designed for a real patient to treat a brain tumor of 38.6 cm^3 with two beams: at 0° and 180° (see Figure 3.3 (b)). For the experiments, only the beam positioned at 0° was used. For this beam, fifteen carbon-ion beam energies from 164.63 MeV/n to 222.31 MeV/n were used. More than 3900 spot positions, with 2-mm spacing in X and Y coordinates, were irradiated with a total number of delivered carbon ions of 1.52×10^8.

Since the long term goal of the current project is the implementation of the proposed monitoring methodology in clinics, measurements during a treatment of a real patient was performed in December 2019. This was the first time that a clinical beam monitoring based on secondary ion detection was performed at HIT. The delivered treatment plan

consists of two beam fields at 5° and 330° to treat a head-and-neck tumor of 73.85 cm^3 (see Figure 3.3 (c)). Only the beam at 5° was only investigated. This beam field consists of twenty-three carbon-ion beam energies, ranging from 95.67 MeV/n to 204.27 MeV/n and more than 5700 spot positions to be irradiated.

3.3. Secondary ion tracking system

The system used to detect and track the secondary ions leaving the head phantom was based on two AdvaPIX TPX3 modules operated in synchronization (see Figure 3.4). They were operated using the Pixet software[3] by connecting both modules to a standard notebook via USD 3.0 ports. The modules exhibit high efficiency to detect charged particles close to 100% [Soukup et al. 2011].

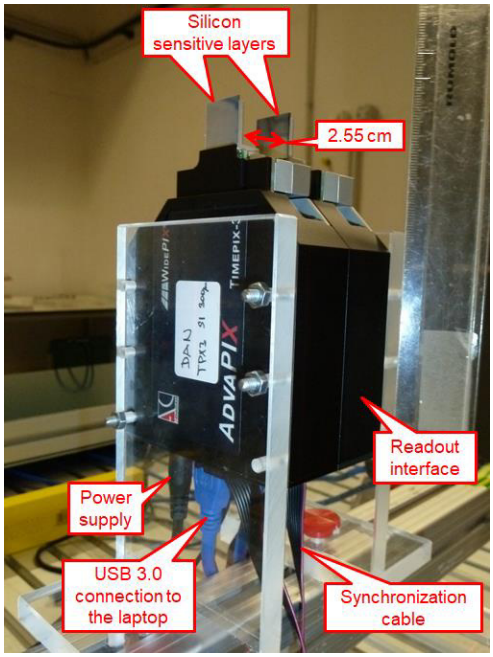

Figure 3.4. Tracking system used in the experiments of this thesis, based on Timepix3 detectors. The distance between both sensitive detection layers is 2.55 cm. Modified from Félix-Bautista et al, 2019.

Each module uses a hybrid pixel semiconductor detector based on the Timepix3 technology, developed at CERN within the Medipix3 Collaboration [Poikela et al. 2014]. In this thesis, the thickness of both sensitive silicon detection areas was 300 µm with an area of detection of 1.98 cm^2, divided into 256×256 pixels with a pitch of 55 µm. Each pixel is individually connected to its own electronic circuit: a preamplifier, a discrimination and a counter in the read-out chip (see Figure 3.5).

[3] Pixet, version 1.5.0.

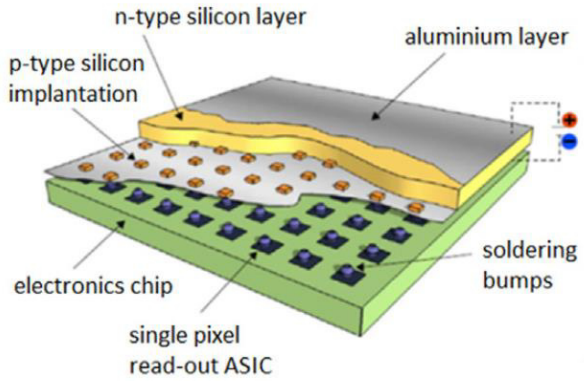

Figure 3.5. Representation of the hybrid pixel semiconductor Timepix3 detector, showing the silicon sensitive layer and the readout chip. Modified from Granja et al, 2021.

Timepix3 detectors also have a combination of a slow digital counter (40 MHz) and a fast digital counter (640 MHz) to provide a fine time stamping (1.56 ns time resolution). The time of arrival related to the slow digital counter and the fast time of arrival (FToA) related to the fast counter enables us to calculate the time-related pixel signal (t), by the equation 3.1:

$$t = ToA \cdot 25ns - FToA \cdot 1.56ns, \tag{3.1}$$

where 25 ns is the time resolution given by the slow digital counter. The energy deposition (Δ_{ToT}), is calculated from the ToT values using the equation 3.2:

$$\Delta_{ToT} = ToT \cdot 25ns. \tag{3.1}$$

When a secondary ion crosses the sensitive silicon detection areas, hole-electron pairs are created and collected by the electric voltage applied (see Figure 3.6 (a)). The generated charge might be collected by multiple pixels adjacent to the hit point of the secondary ion.

Diffusion process taking place during the charge collection, which depends on the bias voltage, is well-known as charge sharing effect [Jakubek, 2009], as shown in Figure 3.6 (b). The group of pixels that collects charge is so-called cluster. The cluster size is defined as the number of pixels that form a cluster. The cluster volume is the sum of all energy-calibrated signals measured by cluster pixels (see Figure 3.7). These two cluster characteristics depend on parameters such as the applied bias voltage, the energy threshold, the type of radiation, the deposited energy and the thickness of the sensitive detection area, among others.

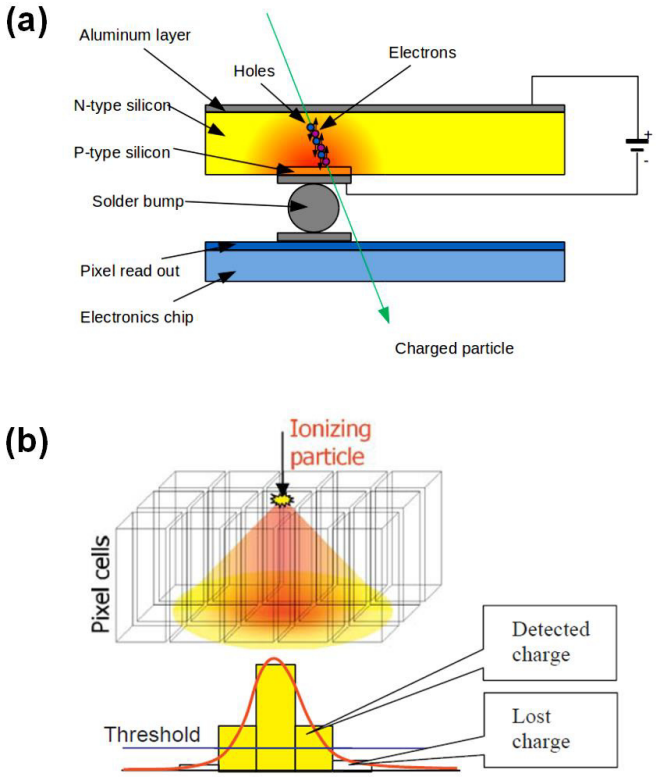

Figure 3.6. (a) Ion interaction with the sensitive silicon detection layer creating hole-electron pairs to be collected by the applied voltage. Reprinted from Reimold, Master thesis, 2017. (b) Example of the charge sharing effect with the pixels collecting the generated charge. Reprinted from Jakubek, 2009.

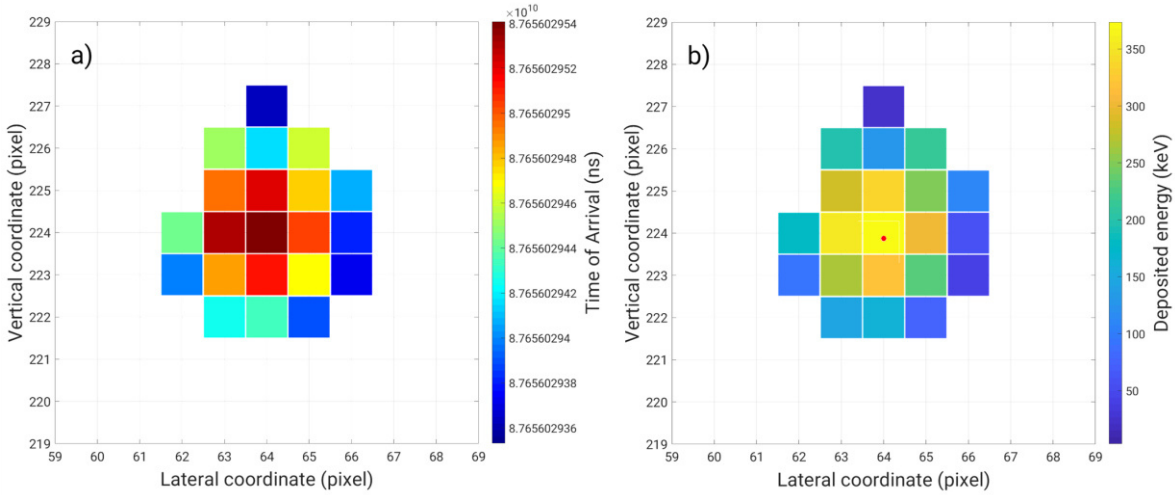

Figure 3.7. Example of neighboring pixels forming a cluster with the information about (a) time of arrival and (b) time-over-threshold acquisition. The red point in (b) represents the center of mass of the cluster. This indicates the hit position of the secondary ion.

Compared to Timepix detector [Llopart et al, 2007], Timepix3 detectors enables us to simultaneously acquire information regarding time of arrival (ToA) and energy deposition (ToT) in each pixel. Moreover, they have no dead-time, what makes them suitable for tracking secondary ion for monitoring purposes due to the dead-time free given by the data-driven readout, as previously investigated [Reimold, 2018; Félix-Bautista et al, 2019]. In these previous investigations, the capabilities of detecting secondary ions produced in carbon-ion irradiations at therapeutic beam energies, clinical doses and dose rate have shown.

In this thesis, the AdvaPIX TPX3 modules were operated at a bias voltage of 10 V, which improves the accuracy of the measured deposited energy of secondary ions [Gehrke et al, 2017] in contrast to higher voltages. Moreover, the energy threshold value plays an important role in the signal generation, because the signal readout takes place only when it is above such a threshold. This helps to reduce possible electronic noise. In this thesis, the energy threshold was set to 3 keV for the monitoring at 30° relative to the beam axis and the measurements of a clinical application of the method (see sections 3.4.1 ad 3.4.3).

Due to the high secondary-ion fluence rate faced in the measurements where the tracking system was placed at 0° relative to the beam axis, improvements in the hardware and the operational parameters of the detectors were performed.

Concerning the hardware of the AdvaPIX TPX3 modules used in this thesis, the chip board for the synchronization was improved by ADVACAM s.r.o.. By using this new board, the trigger signals were optimized changing from CMOS logic to LVDS and by optimizing the terminations of the signals. Moreover, a device-ready signal was added.

Concerning the operation parameters, the energy threshold was set to 12 keV for the monitoring at 0° relative to the beam axis (see section 3.4.2), in order to overcome signal saturation by reducing the cluster sizes. The corresponding energy calibration for this energy threshold was performed. This energy calibration is needed for the time-over-threshold information related to the deposited energy of the ions. The energy deposition information was used to find the center of mass of each cluster to reconstruct the ion tracks, as explained in section 3.5.1. It has to be recalled, that each pixel is individually pixel-wise calibrated in terms of deposited energy. The energy calibration is specific for each energy threshold and each detector.

The energy calibration is performed by using γ-emitter sources, as ^{55}Fe (5.9 keV) and ^{241}Am (59.5 keV), and different x-ray fluorescent materials with energy from 6 keV to 24 keV [Jakubek, 2011]. The calibration function (f) is parametrized as indicated by equation 3.3:

$$f(E) = aE + b - \frac{c}{E - t}, \tag{3.3}$$

where E is the deposited energy, a, b, c, t are parameters determined by per-pixel least-squares fit. The resulting calibration curve presents the behavior as shown in Figure 3.8: at low energies is the curve nonlinear, and at high energies linear.

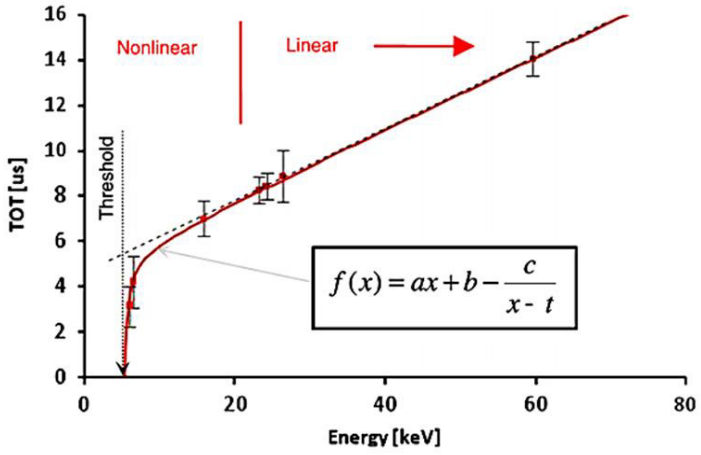

Figure 3.8. Curve of the per-pixel energy calibration process. Reprinted from Jakubek, 2011.

3.4. Experimental configurations for the pencil beam monitoring

The experiments were performed in the experimental room at the HIT facility under clinic-like conditions. These experiments are divided into two main cases in order to investigate the performance of the proposed monitoring methods under different situations. First, the treatment plan for the head phantom was delivered, with the tracking system positioned at 30° relative to the beam axis. Second, the tracking system was positioned at 0° relative to the beam axis in order to compare the results with those from the monitoring with the tracking system at 30° from the beam axis. Moreover, the performance of the presented methodology was exploited using a treatment plan of a real patient. Third, measurements were performed during the first clinical application of the presented method.

3.4.1. Tracking system positioned at 30°

For the measurements in this case, the head phantom was aligned with respect to the isocenter, since the center of the tumor volume coincided with the center of the head phantom. The tracking system was positioned at 30° with respect to the beam axis, at 12 cm away from the isocenter, as shown in Figure 3.9 (a). This angle was chosen as a the compromise between the yield of detected secondary ions and the precision of the track back-projection performed to find its most probable origin in the lateral coordinates. This angle was also used in previous investigations in our research group for range

monitoring purposes [Gwosch et al, 2013; Gaa et al, 2017]. Moreover, information on the pencil beam positions in plane transverse to the beam axis and the range-related information in depth could in principle be obtained simultaneously. However, this thesis is focused only on the lateral positions of the pencil beams.

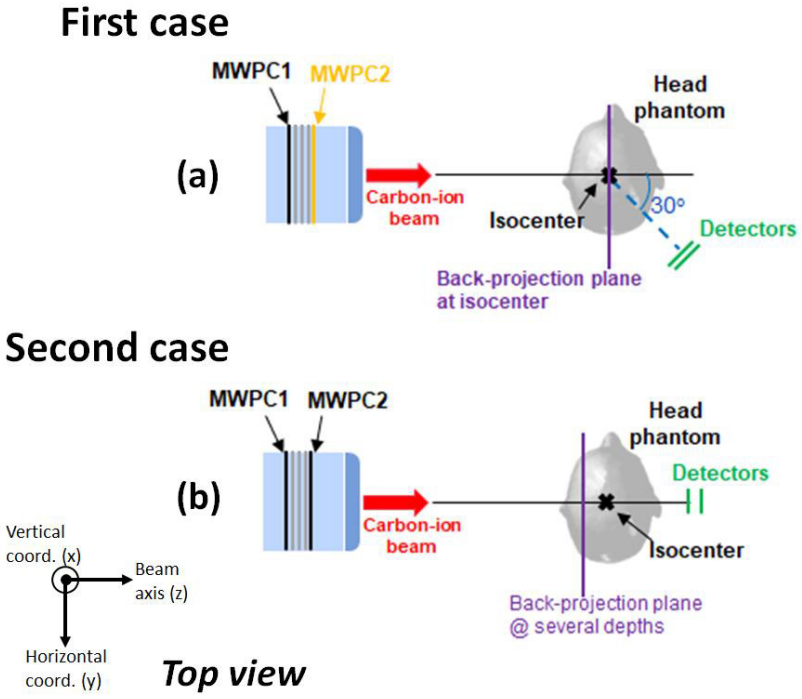

Figure 3.9. (a) Experimental setup built to irradiate the TP1 in the monitoring at 30° relative to the beam axis. The tracking system is at 12 cm from the isocenter. (b) Experimental configuration to irradiate the TP2 in the monitoring at the beam axis (0°). A first irradiation was performed with the MWPC3 at the isocenter. The tracking system is located at 28 cm downstream of the isocenter.

Six irradiation of the TP1 were performed to evaluate the proposed methodology to monitor the lateral pencil beam positions. In this case, the reference lateral beam positions were obtained from the MWPC2 located in the beam nozzle.

3.4.2. Tracking system positioned at the beam axis (0°)

The experimental setup used in this investigation with the tracking system positioned at 0° relative to the beam axis is shown in Figure 3.9 (b). Here, twofold investigation was carried out: comparison of the results for tracking system positions at 30° and 0° and performance of the method for a real clinical treatment plan.

Comparison of the results for tracking system positions at 30° and 0°

The first part consists of a comparison with the results from the measurements (see section 3.4.1) when positioning the tracking system at 0° with respect the beam axis and at 35 cm downstream of the isocenter. The same data analysis performed in the monitoring with the tracking system positioned at 30° was performed here, i.e., references lateral beam positions were taken from the MWPC2.

Performance of the method for a real clinical treatment plan

In this part, the TP2 is delivered with the head phantom located at the isocenter and the tracking system was located at 28 cm downstream of the isocenter, and at 0° relative to the beam axis (see Figure 3.9 (b)).

Afterwards, the head phantom was replaced by the MWPC3 and the TP2 was delivered once more. This was done in order to obtain the reference lateral beam positions at the isocenter form the MWPC3. The importance of these lateral beam positions is given in chapters 1 and 2.

3.4.3. Measurements of real–patient treatment delivery

The measurements performed in the first clinical secondary-ion-based beam monitoring at HIT were performed with the tracking system positioned at 30° from the beam axis. Figure 3.10 (a) shows the device for holding the tracking system and cables during the clinical measurement.

The Siemens medical cart consisting of a drawer and lock system in its four wheels. A robust aluminum arm was incorporated to the cart in order to hold the tracking system[4], composed of two AdvaPIX TPX3 modules (see section 3.3) and to reach the desired position with respect to the isocenter (see Figure 3.10 (b)). The tracking system is protected by a 3D-printed box located at the distal edge of the aluminum arm. This box is already rotated by an angle of 30° with respect to the beam axis. The distance between the tracking system and the isocenter was 16 cm (see Figure 3.10 (c)). The center of the frontal sensitive detection area was positioned at the height of the isocenter. This 16-cm distance was chosen as a compromise to avoid any interference with the patient and to maximize the yield of detected secondary ions.

An alignment system of the medical cart is mounted in the aluminum arm. It consists of three ruler to indicate the desired position of the tracking system with respect to the

[4] This arm was built and integrated to the medical cart by the Medical Engineering group in the Department of Medical Physics in Radiation Oncology at the German Cancer Research Center (DKFZ).

laser system inside the treatment room, which is also used for patient positioning (Figure 3.10 (c)).

The detectors of the tracking system were operated at 10 V bias voltage and the energy threshold in the pixels was set to 3 keV.

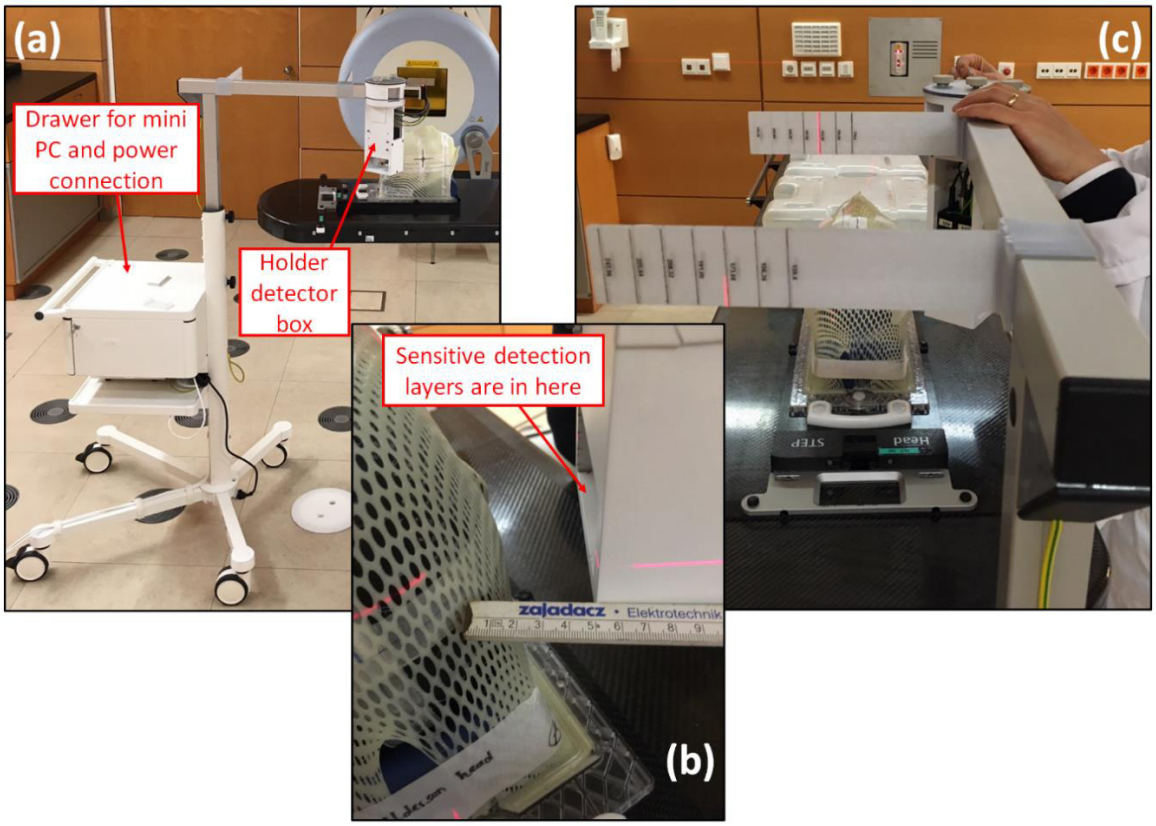

Figure 3.10. (a) Medical cart used to position the tracking system at 30° with respect to the beam axis. The detectors were connected to a mini PC located inside the drawer of the medical cart in order to be remotely operated. (b) Ruler indicators for the alignment of the medical cart with respect to the laser system of the treatment room. (c) Position of the tracking system with respect to the head of the patient.

The detectors of the tracking system are connected to the mini PC inside the drawer with USB3.0 cables, which are inside the aluminum arm, together with the corresponding cables of the power supply. These cables are connected to an electric connection mounted inside the drawer. In order to prevent any interference due to the electricity, each part in the medical cart has been grounded. The remote connection to operate the tracking system is performed by an Ethernet connection. Moreover, the Ethernet connection to the mini PC is done by a network medical isolator device (see Figure 3.11).

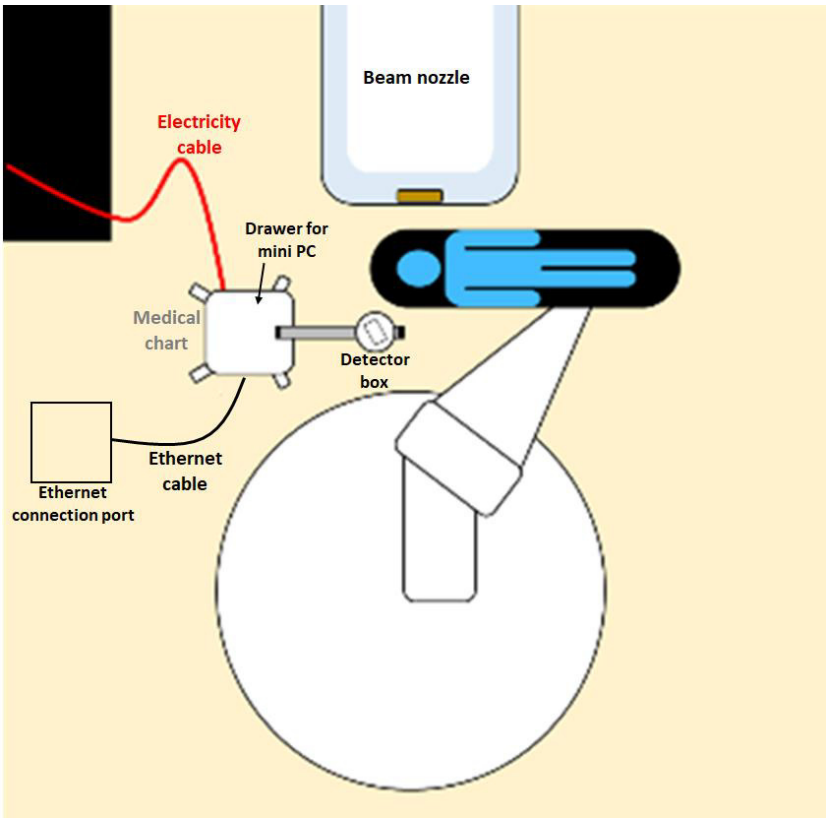

Figure 3.11. Sketch of the medical cart setup in the treatment room at the HIT facility. The mini PC is remotely operated via the Ethernet connection. Courtesy of Laura Ghesquière-Diérickx.

3.5. Data processing and analysis

Two ASCII files were obtained from the data acquisition during the measurements. These files contain pixel information such as the coordinate of the hit pixel, the time of arrival and the energy deposition of the impinging ion. The pixel information was further processed and analyzed by in-house written C++ and MATLAB[5] routines, as explained in the following.

3.5.1. Clusterization and coincidence processes

As the raw data is given in terms of pixel information, all pixels belonging to the hit by a single ion have to be found first. For this, a so-called clusterization process (i.e., cluster creation) was performed. Here, an iterative process is performed based on time difference between the spatially neighboring pixels. If the time difference between pixels is below 150 ns, they are considered to be part of the same cluster. Time for the collection

[5] MATLAB, version 9.3.0 (R2017b). The MathWorks, Inc., Natick, Massachusetts, USA.

charge is also considered in this time difference [Reimold, 2019]. Afterwards, the earliest pixel hit in the cluster is taken as the time of arrival (ToA) of the secondary ion. This information is the basis for finding the coincidences. Figure 3.12 illustrates the signal distribution of the pixels of a cluster according to the time of arrival.

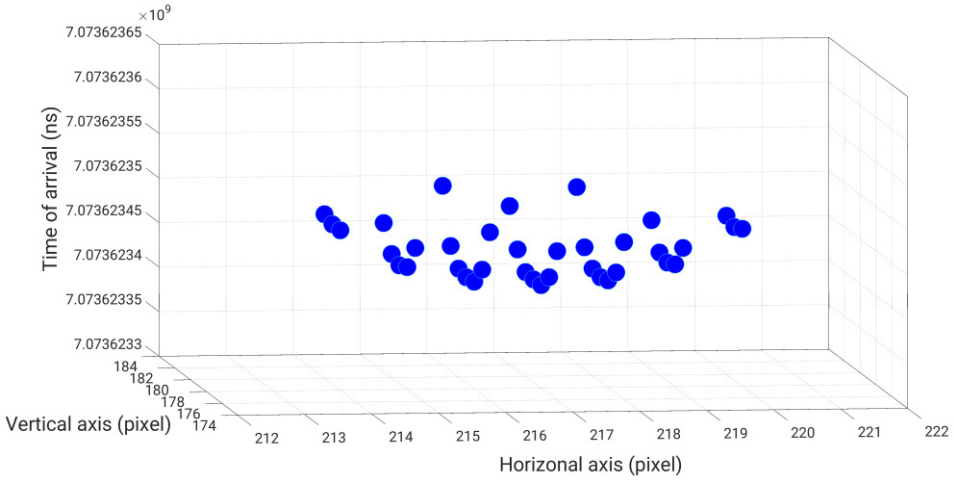

Figure 3.12. Distribution of the ToA signal in the pixels of a cluster.

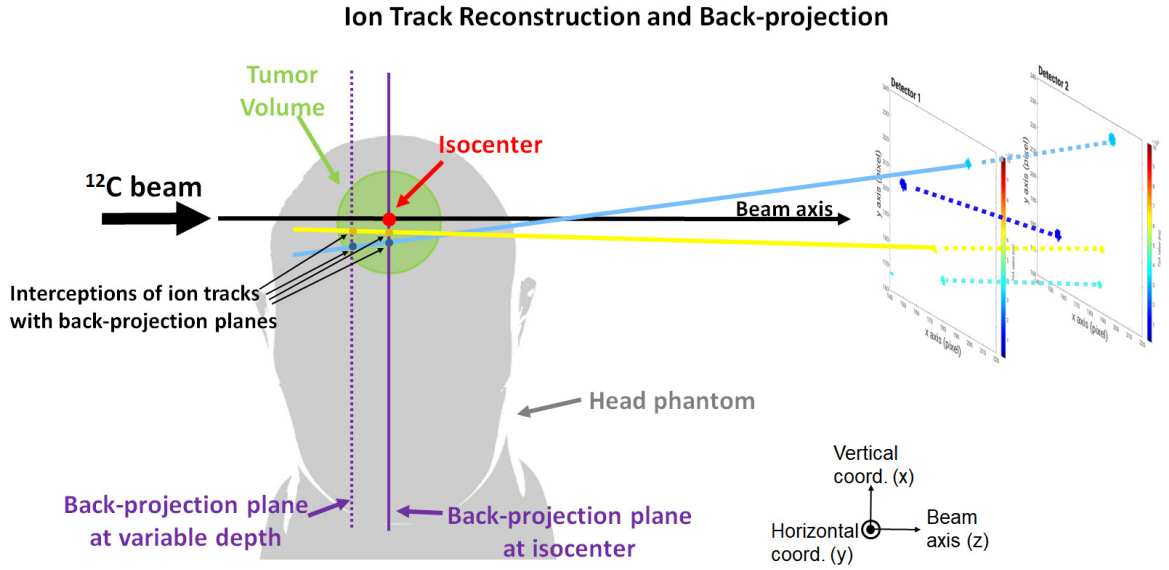

Figure 3.13. Cluster coincidence finding and reconstruction of ion tracks (dashed color lines) based on the arrival time of the clusters. The color bar indicates the arrival time. Examples of the back-projection of the ion tracks onto the transverse plane located at the isocenter of different depth are indicated by the solid color lines. The tumor volume is represented by the green circle. Modified from Félix-Bautista et al., 2021.

In order to reconstruct the secondary ion track, a cluster coincidence finding process is performed based on the ToA of the clusters in both sensitive detection areas. The ToA of the cluster pair in the two in both sensitive areas has to be close enough in time in order the same to be considered as the result of the interaction of the same secondary ion. The coincidence time window was set to ±50 ns. The fine time stamp of the detectors, the synchronization between the detectors and the charge collection are considered in this coincidence time window value. An example of the reconstruction of ion tracks is illustrated in Figure 3.13.

In order to cope with ambiguities in the coincidence finding, comparison of similarities between the cluster parameters is considered in both sensitive detection areas. In particular, when the tracking system is positioned 0° relative to the beam axis, the secondary-ion fluence rate is high (up to about 1.5×10^5 ions/s/cm^2), because direction of the most of the produced secondary ions is forward directed. Therefore, resolving ambiguities plays there a particularly important role. The used resolving algorithm is based on ten different parameters related to the clusters: deposited energy, maximum energy (cluster height), weighted center, axis and polar angle, linearity, border and inner pixels, thickness and thinness, curliness, roundness and length [Marek, 2020]. From this, information dissimilarities between clusters are calculated and then the coincident clusters with the lowest dissimilarities are matched. A boundary of 2σ has been introduced as a constraint on the maximum dissimilarity.

Having found the matching clusters, secondary ion tracks are reconstructed using a straight line between the centers of mass calculated in the clusters. This straight line is then back-projected to the phantom volume in order to find an approximation of their origins in the lateral coordinates with respect to the beam direction. A single plane transverse to the beam axis is used for the entire treatment plan. The depth of the transverse plane differs for the tracking system position at 30° and 0° with respect to the beam axis.

3.5.2. Analysis of ion tracks

In order to find the measured lateral pencil beam positions, all the tracks measured during the delivery of that particular pencil beam were fond, based on the time information of the measured data and the beam record files. The reconstructed ion tracks were back-projected onto a plane transverse to the beam axis. The depth location of the transverse plane was different according to the measurement case under investigation. For the tracking system at 30° relative to the beam axis, the back-projection plane was located at 0 mm (isocenter). For the tracking system at 0° relative to the beam axis, the back-projection plane was located at five additional depths upstream of the isocenter: 30 mm, 40 mm, 50 mm, 60 mm and 70 mm. Figure 3.13 shows an example of a back-projected ion track onto the transverse plane at the isocenter.

The back-projected ion tracks were separated in time that corresponds to the duration of the irradiation for each pencil beam. This time was extracted from the beam record

files. Figure 3.14 shows two examples of the back-projected ion tracks for two different pencil beam positions belonging to two beam energies of the TP2.

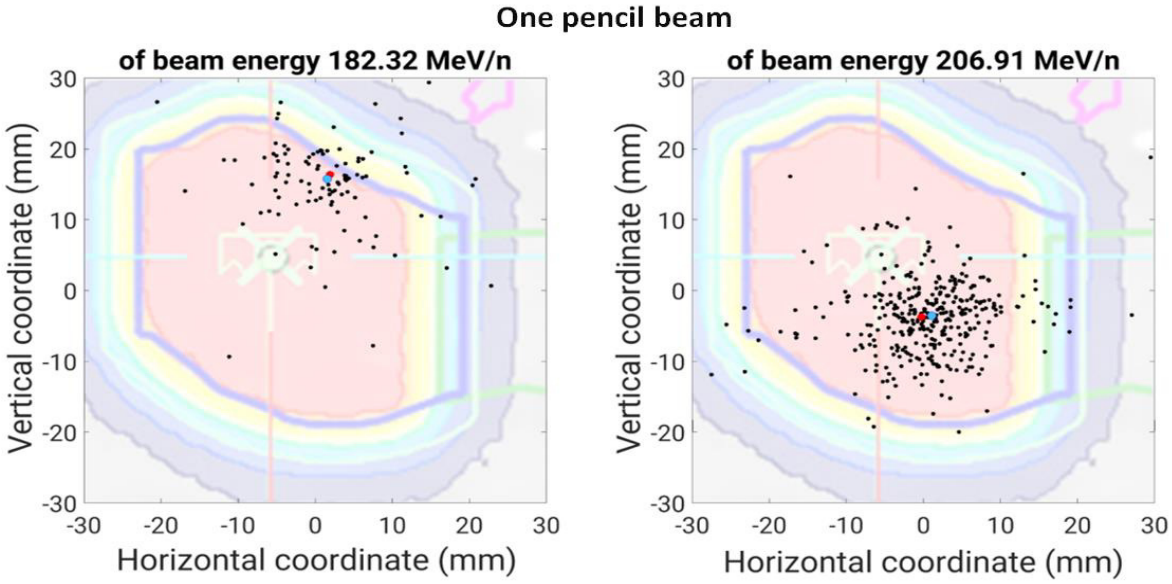

Figure 3.14. Two examples of the back-projected ion tracks (black points) belonging to two different pencil beam positions. Median values are represented by the blue points, which are referring to the measured pencil beam positions. Red points indicate the reference beam positions measured by the monitoring chambers in the nozzle. The planning tumor volume of the TP2 (sagittal plane) is indicated by the solid blue line. The isocenter is indicated by the green cross. Reprinted from Félix-Bautista et al., 2021.

The measured pencil beam positions were derived from the back-proejcted ion tracks by the median value of the distribution in both vertical and horizontal coordinates. The calculation of the median value reduces the influence of outliers. These outliers can be caused by the scaterring process that secondary ions undergo inside the phantom.

3.5.3. Effectivity, precision and accuracy of the method

The quantitative evaluation of the performance of the proposed monitoring methodology is based on three values: effectivity, precision and accuracy. These values are the results of the comparison between the measured and reference beam positions. The evaluation was performed in both vertical and horizontal coordinates separately. Figure 3.15 illustrates the comparison between the measured and the reference beam positions.

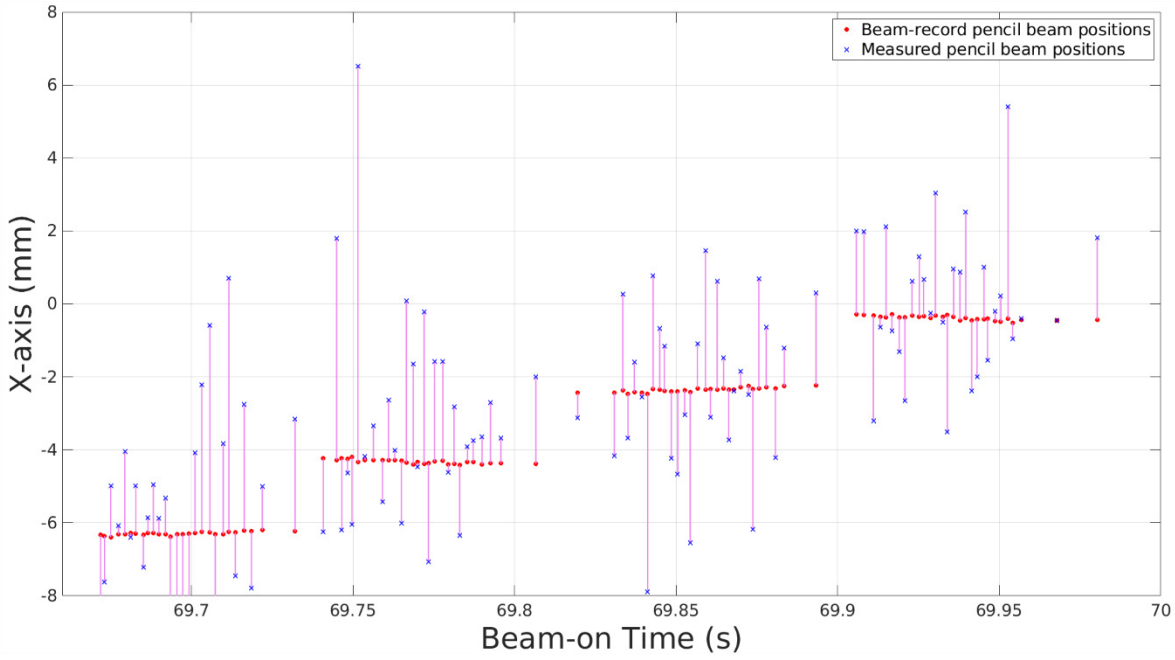

Figure 3.15. Illustration of the comparison between the measured (blue points) and the reference pencil beam positions (red points). Reprinted from Félix-Bautista et al, 2019.

The effectivity is defined as the number of analyzed pencil beam positions over the total number of beam positions within the entire treatment plan. The precision is the standard deviation of signed differences between measured and reference beam positions. Finally, the accuracy is defined as the mean value of the absolute differences between the measured and reference beam positions. The uncertainty of the accuracy (σ_{acc}) was calculated by the equation 3.4:

$$\sigma_{acc} = \sqrt{\frac{\sum_{i=1}^{n}(x_i - \bar{x})^2}{n(n-1)}} \tag{3.4}$$

where $\bar{x}$ is the mean of the absolute distances in each beam energy, x_i stands for the *ith*-absolute difference and n is the total number of pencil beam positions that were compared in each beam energy. Examples of the difference distributions are shown in Figure 3.16.

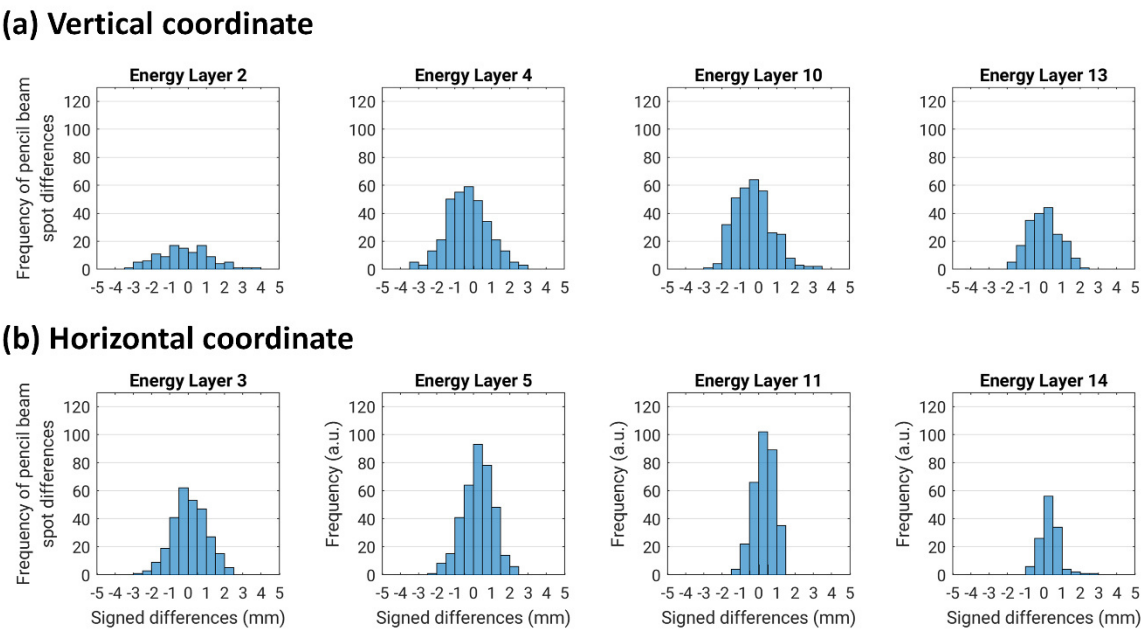

Figure 3.16. Examples of difference distributions for the comparison between measured and reference pencil beam positions for each beam energy layer separately of the TP2. Precision and accuracy were calculated from such difference distributions.

Chapter 4
Results and Discussion

In this thesis, a methodology to monitor the lateral positions of carbon-ion beams was developed and evaluated under clinical conditions. Quantitative evaluations of the performance of the methodology were based on precision, accuracy and effectivity (see section 3.5.3). Firstly, the experimental verification of the proposed methodology in a clinic-like carbon-ion treatment delivery with the tracking system positioned at 30° from the beam axis (see section 4.1). Secondly, this methodology was applied for measurements with the tracking system at both 0° and 30° relative to the beam axis (see section 4.2). Thirdly, for measurements concerning the first clinical application of the method (see section 4.3).

The results of the experimental measurements are presented in this chapter in the following order:

i) Experiments in a head phantom with the tracking system positioned at 30° relative to the beam axis (12 cm from the isocenter, treatment plan TP1, reference lateral beam positions from the MWPC2) (see section 4.1).

ii) Experiments in the head phantom with the tracking system positioned at 0° relative to the beam axis (see section 4.2). These measurements are divided in two parts:
   a. Comparison with the experiments performed at 30° (treatment plan TP1, tracking system at 35 cm downstream of the isocenter, reference lateral beam positions from the MWPC2).
   b. Measurements to assess the capabilities of the monitoring methodology using a real patient treatment plan (treatment plan TP2, tracking system at 28 cm downstream the isocenter, reference 16 cm from isocenter, reference lateral beam positions from the MWPC3).

iii) First clinical application of the proposed monitoring methodology. Measurements were performed during a patient treatment with the tracking system

positioned at 30° relative to the beam axis (treatment plan TP3, tracking system at 16 cm from). (see section 4.3).

Measurements in points i) and ii) were conducted at the experimental room under clinic-like conditions. The measurement in point iii) was performed in one of the treatment rooms during a real treatment delivery.

4.1. Pencil beam monitoring with the tracking system positioned at 30°: experimental evaluation of the performance

The monitoring methodology was assessed in terms of precision, reproducibility and accuracy reached in these measurements. The used carbon-ion TP1 was specifically designed for an anthropomorphic head phantom (see section 3.2.).

The secondary ion tracks were measured during six irradiations of the TP1. A first delivery was carried out in order to evaluate the method in terms of precision. To determine the measured lateral beam positions, al the ion tracks were back-projected onto the plane transverse to the beam axis located at the isocenter. Subsequently, the back-projected ion tracks were separate into groups belonging to single pencil beams as detailed in section 3.5.2. A constraint in the number of ion tracks per pencil beam was introduced, considering more than eight ion tracks per pencil beam. Only 2% of pencil beams with less than eight ion tracks were neglected. This procedure was performed in order to reduce the impact of uncertainties coming from the low statistics for some pencil beam, in particular for the low beam energies.

4.1.1. Comparison between measured and reference lateral beam positions

For each pencil beam, the median position of all tracks where they intersect the back-projection plane was then calculated (see Figure 3.14 for visual explanation) in both vertical and horizontal coordinates to obtain the coordinates of the measured lateral pencil beam positions. Afterwards, the measured lateral beam positions were compared with the reference lateral beam positions, as shown in Figure 4.1.

The delivery of the treatment plan took almost 110 seconds. Twenty two groups can be seen in Figure 4.1, that corresponds to the twenty two carbon-ion beam energies used along the treatment to cover the tumor volume in this treatment plan. Since the production of secondary ions takes place only during the time when the ion beam is on, naturally there are no measured points during spill pauses. This explains the gaps in between the groups. The beam-off time was about 1.5 min for this case. It has to be pointed out, that the ion beam is inactive during 4 s approximately, time needed for the accelerator to change the ion beam energy.

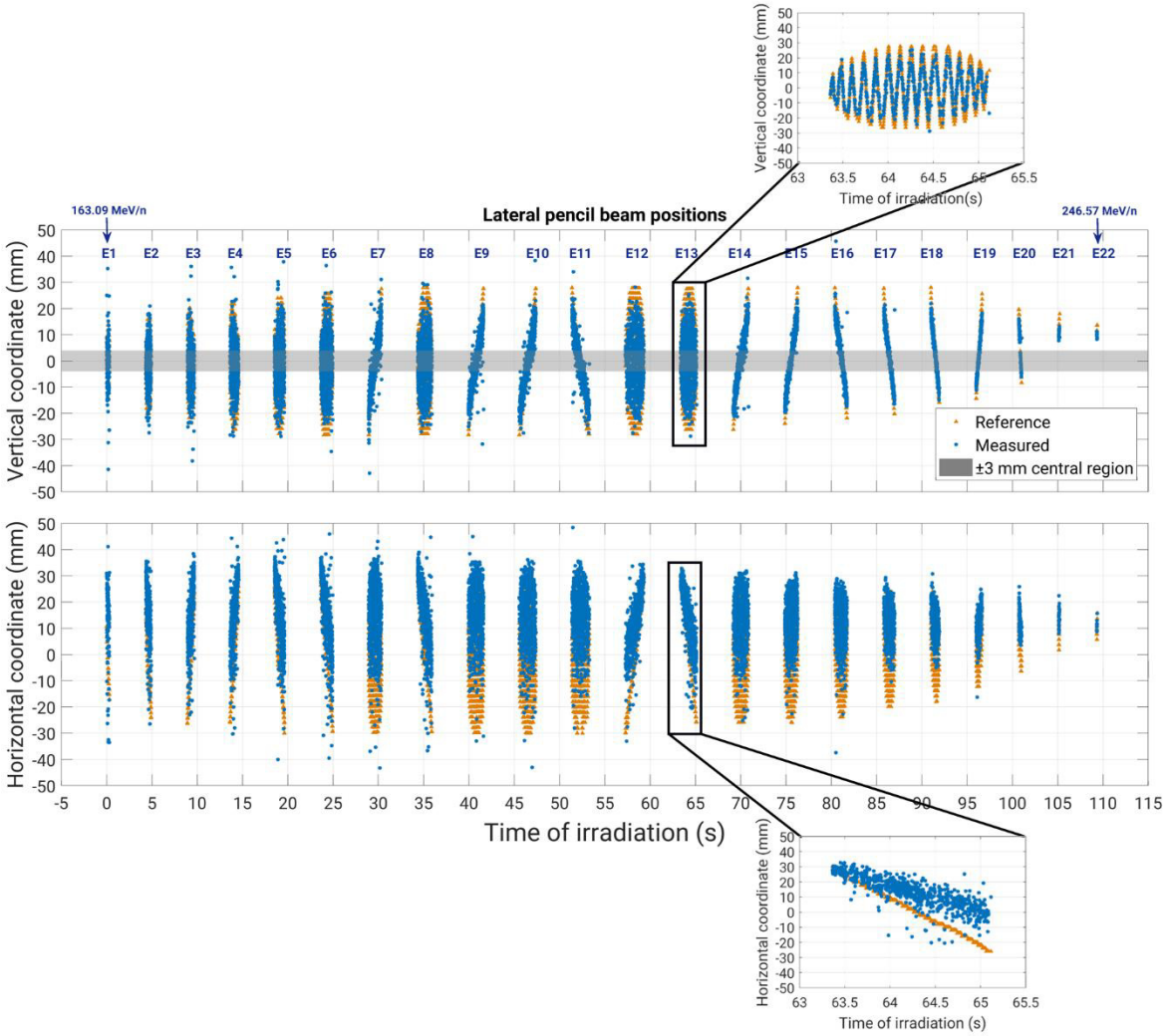

Figure 4.1. Comparison of reference (orange triangles) and measured (blue points) lateral pencil beam positions in (a) vertical and (b) horizontal coordinates. Shaded grey area in (a) indicates the evaluated ±3-mm central region. Zoom images correspond to the beam energy of 221.05 MeV/n, showing fast and slow beam scanning movements, as mentioned in section 3.1.1.

The pattern corresponding to the beam scanning movement can be clearly seen. The measured lateral beam positions also present the same movement behavior. The beam scanning movement is "slow" when irradiating at low intensities and higher rates (see vertical coordinate in upper zoomed plot in Figure 4.1). In contrast, the movement is "fast" when irradiating at high intensities and lower rates (see horizontal coordinate in lower zoomed plot in Figure 4.1). From this, the monitoring methodology is capable of follow the entire pattern of the beam scanning along the treatment delivery in the vertical and horizontal coordinates (see Figures 4.1 (a) and (b), respectively).

A shift of the measured lateral beam positions is seen in Figure 4.1 (b). The reason of this is the geometry of the experimental configuration. As shown in Figure 3.9 (a), the

position of the tracking system is in the positive direction of the horizontal coordinate. Therefore, the quantitative assessment was only performed on the vertical coordinate.

4.1.2. Precision and accuracy of the monitoring method

The evaluation of the precision of the method was based on the calculation of the distances between the measured and the reference lateral beam positions, as mentioned in section 3.5.3. From here on, the distance differences are called signed differences.

As seen in Figure 4.1 (a), the distribution of measured lateral beam positions is "shrunk" with respect to the reference positions. This is due to the location of the back-projection plane at the isocenter, leading to a systematic underestimation of the pencil beam positions located at the outer edges of the treatment field, far away from the central beam axis. In order to exclude the affected data region, reference lateral beam positions within a central region of ±3 mm around the central beam axis were selected for the analysis of signed differences, as shown in Figure 4.2 (a).

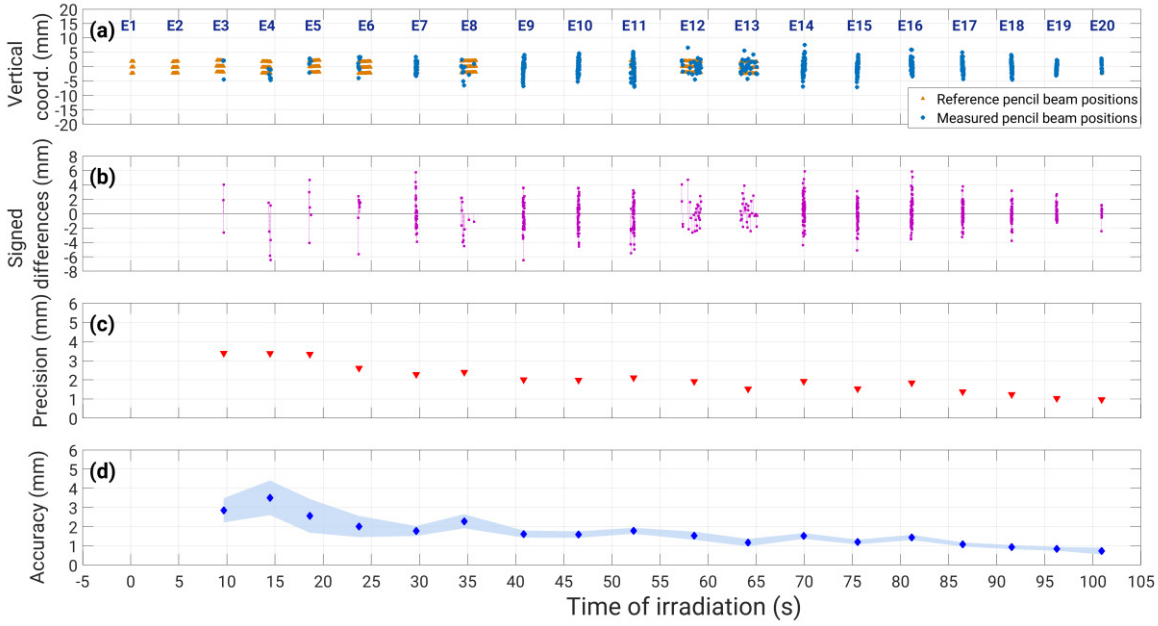

Figure 4.2. (a) Comparison of reference (black triangles) and measured (blue points) pencil beam positions within the selected central region of ±3 mm. (b) Signed distance differences between reference and measured pencil beam positions. (c) Precision and (d) accuracy of the method within the selected central region. Shaded blue area in (d) indicates the uncertainty of accuracy.

Due to the applied constraint on the number of eight ion tracks per pencil beam aforementioned, the first two beam energies (E1 and E2) show no measured pencil beam positions.

The signed differences for the single pencil beams are shown in Figure 4.2 (b). The standard deviation of the difference distributions with each beam energy was calculated (see section 3.5.3), giving the value of the precision in each beam energy. The obtained precision values are shown in Figure 4.2 (c), and they go from 0.98 mm to 3.39 mm. Due to the selection of the ±3-mm central region and the applied constraint to the number of ion tracks per pencil beam, the last two beam energies (E21 and E22) are not taking part of the analyzing. Furthermore, the total number of tracked secondary ions per delivered primary carbon ion was also calculated. It was found to be on average 0.00024 for the delivered TP1.

Figure 4.2 (d) shows the accuracy. It was obtained by calculated the mean of the absolute distance differences in each beam energy. Uncertainties of the accuracy are shown by the shaded area. The obtained accuracy values range from 0.75 mm to 3.51 mm. The value of 0.75 mm also corresponds to the highest beam energy evaluated (E20).

The decreased precision and accuracy values as seen for the lowest beam energies are due to the low amount of detected secondary ions coming from these beam energies and the increased scattering than these secondary ions undergo inside the head phantom. By increasing the sensitive detection areas [Jakubek et al, 2014], the amount of detected secondary ions can increase.

4.1.3. Reproducibility of the monitoring method

Six deliveries of the same treatment plan (TP1) were carried out in order to investigate the uncertainty of the precision and the reproducibility of the results. Separately for each delivery, the difference distributions were obtained in each beam energy, followed by the calculation of the standard deviation of difference distributions in each beam energy for each repetition. Afterwards, the mean of the six calculated standard deviations was obtained for each beam energy. The resulting values are shown in Figure 4.3, where the points represent the mean precision and the uncertainty bars indicate the reproducibility. In this situation, the precision values range from 0.84 mm to 2.59 mm.

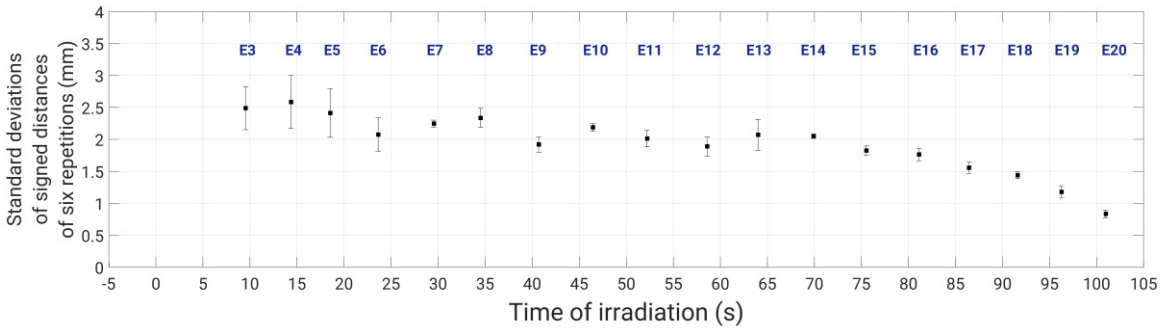

Figure 4.3. Standard deviations of signed distances for the six deliveries of the TP1. The calculation was done within the selected central region of ±3 mm.

To mimic a situation in which the tracking system consist of six pairs of AdvaPIX TPX3 modules with sensitive detection areas of 2 cm^2, the results of the six measurements were added together. Compared to the obtained values for one repetition only, the precision improved from 14% to 24% by assuming that five more tracking systems were added to the first system. With this configuration, the precision could be improve, showing that the main issue for the proposed methodology is related to the yield of secondary ions detected and tracked and to the size of the sensitive detection area.

4.1.4. Investigation on the sensitivity of the method

Each time a treatment is delivered, the ion beam is monitored by the BAMS in the nozzle and beam record files are generated. These files contain the coordinates of the reference lateral beam positions. Ideally, the contained information in the beam record files should be the same for several deliveries of the same treatment plan. However, this is different in reality, since spill-to-spill variations in the pencil beam parameters as beam intensity, size and positions are present. To evaluate the effect of such variations, the method was assessed in terms of sensitivity. This assessment consisted in the comparison of the measured lateral beam positions obtained in first delivery of the treatment plan with the reference lateral beam positions obtained in the five subsequent deliveries of the same treatment plan.

Figure 4.4 shows the accuracy when comparing the measured lateral beam positions with the incorrect reference positions of the different deliveries. The shaded areas indicate the uncertainty of the obtained values.

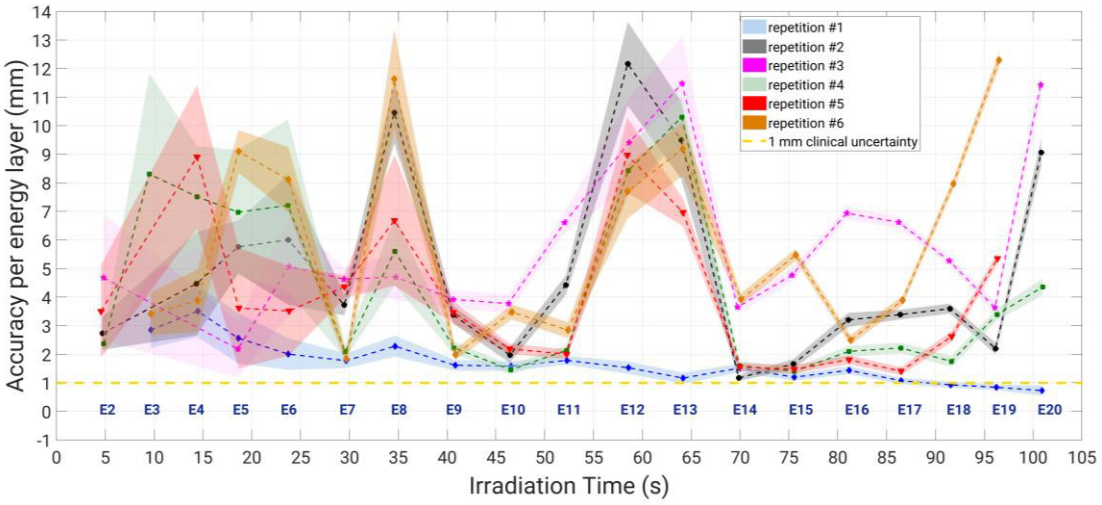

Figure 4.4. Accuracy of the method when comparing measured pencil beam positions with reference positions of different deliveries of the TP1. Blue curve is the accuracy of measured pencil beam positions compared to its corresponding reference positions. The other curves indicate accuracy values obtained when combining the measured positions (first delivery of the TP1) with the beam positions measured by the BAMS for different deliveries of the same treatment plan. Shaded color areas indicate the uncertainties.

The accuracy of the measured lateral beam positions that were compared with their corresponding reference positions is shown by the blue curve. It is apparent, that the accuracy values increase significantly when comparing the measured pencil beam positions with the reference pencil beam positions as measured by the BAMS for other deliveries of the same treatment plan.

Focusing on one typical beam energy, for instance, beam energy 16 (224.81 MeV/n), the time structure differences in the reference positions can be visualized in Figures 4.5 (a) and (b). The time structure varies from one delivery to another of the same treatment plan. This is manly caused by fluctuations of the beam intensity, reflected in the time needed to deliver required number of ions per spot.

When comparing the reference positions of the first delivery with the reference positions of the third delivery, accuracy differences are about 7.47 mm (see Figure 4.5 (a)). When comparing the reference positions between the first and fifth delivery, accuracy differences are 0.34 mm (see Figure 4.5 (b)). This means that variations in treatment delivery can be detected with the proposed monitoring method. Therefore, the sensitivity of the monitoring method is not enough to detect such small differences.

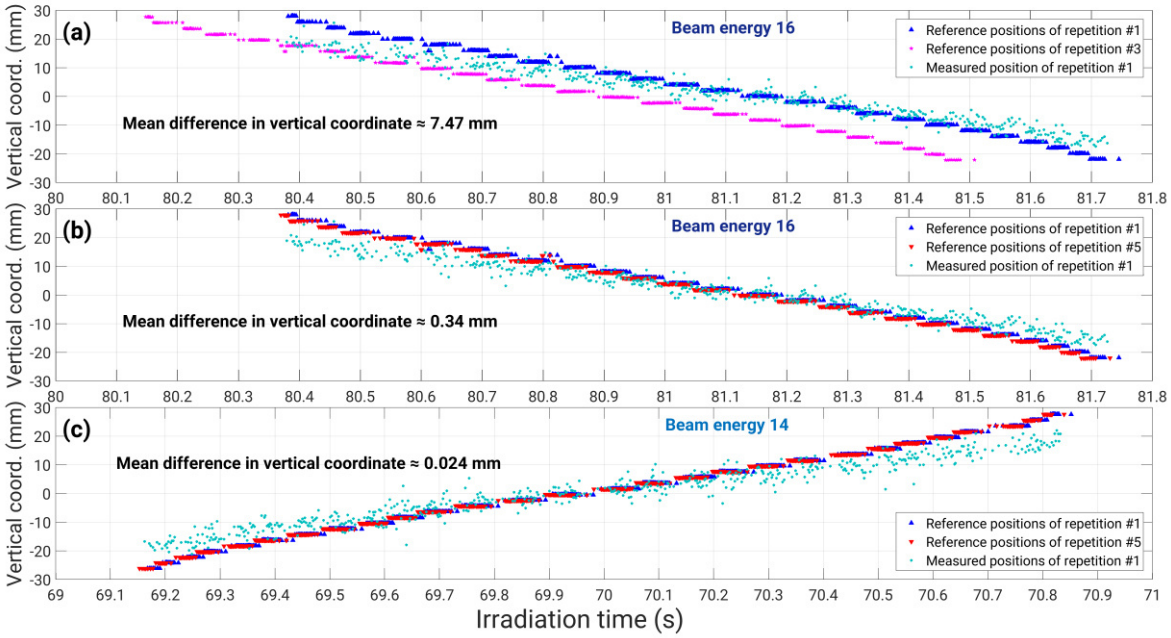

Figure 4.5. Time structure fluctuations due to synchrotron variations between (a) the first and third delivery and (b) the first and fifth delivery of the TP1 in the beam energy 16 (224.81 MeV/n). (c) Time structure of the first and fifth delivery of the TP1 in the beam energy 14 (217.25 MeV/n).

Not only there are large differences in the accuracy values, but also in their uncertainties increase, in particular for the lowest beam energies (irradiation times between 5 s and 35 s). In contrast, from higher beam energies (irradiation times greater than 40 s) the

uncertainties were found to be around ±5% on average, with decreased accuracy values. For the beam energies E12 and 13 (see Figure 4.4), the uncertainties were found to be ±14% on average.

4.1.5. Influence of the alignment of the tracking system on the results

The alignment of the tracking system in this study was not performed with respect to the laser system in the experimental room, since the geometry of the experimental configuration was not symmetric. Therefore, the fine residual alignment corrections were performed offline during the data analysis. A tilting on the b coordinate of the sensitive detection area was optimized (see Figure 4.6 (a)). The tilting affects the vertical coordinate obtained from the data analysis, as can be seen in Figure 4.6 (b).

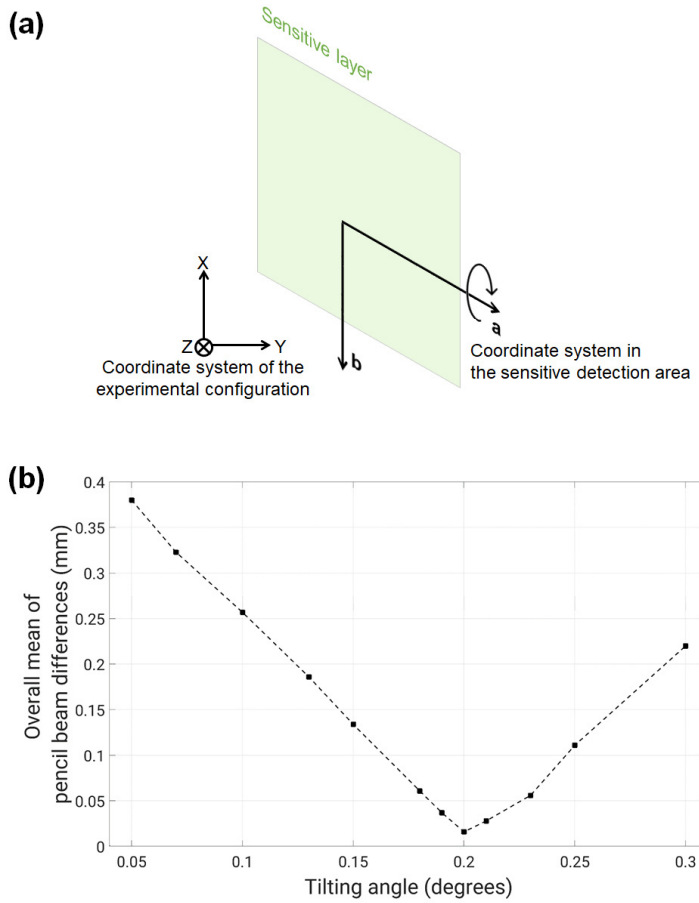

Figure 4.6. (a) Scheme of the applied tilting angle on a-axis of the sensitive detection area. (b) Overall mean absolute differences of measured and reference pencil beam positions. The minimum overall mean differences was found at a tilting angle of 0.2°.

In order to find the optimal tilting angle to compensate for a minor residual misalignment, the minimum overall value of the precision was found. For that, twelve values of the tilting angle between 0.05° and 0.3° were analyzed. The minimum overall value was found to occur at the tilting angle of 0.2°, as shown in Figure 4.6 (b). The tilting correction was applied only for the vertical coordinate and not for the horizontal coordinate, since it was not evaluated for the reasons aforementioned. It has to be pointed out, that all the results presented above were already plotted with the actual tilting correction. In the following sections of this chapter, the corresponding alignment of the tracking system is explained.

4.1.6. Discussion to the monitoring performance with tracking system positioned at 30°

In Figure 4.2 (c), the precision value of 0.98 mm corresponds to the highest beam energy evaluated (E20), since the number of delivered primary carbon ions was the highest (~400,000 carbon ions per pencil beam), allowing the highest number of secondary ion tracks per pencil beam to be detected. Moreover, the energy of the secondary ions is the highest, minimizing the multiple Coulomb scattering in the head phantom.

The found total number of tracked secondary ions per delivered primary carbon in this experiment was 0.00024. In Rucinski et al, 2018, a homogeneous PMMA phantom was irradiated with monoenergetic helium- and carbon-ion beams in a single beam position. Although the detection angles were 60° and 90° relative to the beam axis, production of secondary ions was reported to be between 0.5 to 17.5×10^{-3} per primary ion per steradian, depending on the incident ion beam. Considering the solid angle of 0.014 sr for the tracking system placed at 12 cm from the isocenter in this current study of the thesis, the found value of secondary ions per primary ion per steradian was 17.1×10^{-3}, which is in the order of the value reported in Rucinski et al, 2018. Since the yield of detected secondary ions decreases as the detection angle increases [Gwosch et al, 2013; Haettner et al, 2013; Robert et al 2013], the value of 17.1×10^{-3} seems smaller when placing the tracking system at 30°, in contrast to that for detection angle at 60° and 90°. It is recalled, that the size of the sensitive detection area used in this thesis is 1.4×1.4 cm^2, in contrast to 20×20 cm^2 reported in previous studies [Piersanti et al, 2014; Traini et al, 2017; Rucinski et al, 2018].

The use of larger areas of detection [Jakubek et al, 2014] and the future development of a tracking system consisting of several sensitive detection areas at different positioning angles can increase the yield of detected secondary ions, in particular those coming from lower beam energies, and, thus, the improvement of the precision of the method.

Furthermore, the location of the back-projection plane has to be optimized in order to avoid the "shrinkage" of the measured lateral pencil beam distribution. Thus, we could

obtain the most adequate back-projection plane when several treatment plans are analyzed.

Published studies of other authors regarding the monitoring of the ion beam, specifically, ion range monitoring, have extra material between the beam nozzle and the irradiated object [Agodi et al, 2012; Henriquet et al, 2012; Piersanti et al, 2014; Toppi et al, 2016; Rucinski et al, 2018]. This material is a thin plastic scintillator used as start counter (to measure the primary carbon ions), which can introduce scattering of the primary ion beam, potentially impacting the conformation of the dose to the target volume. Furthermore, a beam hodoscope, consisted of square scintillating fibers, between the beam nozzle and the irradiated object is required in the interaction vertex imaging (IVI) technique, to tag the incoming carbon ions and to determine their trajectories [Henriquet et al 2012]. This beam hodoscope can also introduce scattering of the primary carbon-ion beam.

In contrast to the techniques mentioned above, the proposed monitoring methodology does not require any extra material in the primary beam. Thus, our methodology is more clinically acceptable.

4.2. Pencil beam monitoring with the tracking system positioned at the beam axis (0°): experimental evaluation of the performance

In contrast to the measurements at 30° from the beam axis (see section 4.1), the tracking system was positioned at 0°, i.e., on the beam axis, in order to improve the precision and accuracy values. The aim of this experimental configuration was to minimize both statistical and geometrical uncertainties, and to monitor both vertical and horizontal coordinates. However, several major technical issues were faced with the new configuration. They were related to the high secondary-ion fluence rate due to the forward direction of most of the secondary ions in the nuclear fragmentations. The detected fluence rate was up to 1.5×10^5 ions/s/cm^2, overtaking the speed of data readout and causing strong pile-up signals. In particular, signal clusters related to different ions could not be separated. Figure 4.7 shows the effect of the high fluence rate for the evaluation of the lateral pencil beam positions.

The beam energy E18 shows only few measured pencil beam positions, whereas the last four beam energy show no measured beam positions at all. This is due to the effect of the high secondary-ion fluence rate on the sensitive detection areas. This high fluence rate saturates the detectors while processing the acquired information, impeding the acquisition of more signal beyond at certain value. In this case was after irradiation time of 90. Moreover, for these last beam energies, the number of primary carbon ions sent per spot is greater than that for the lower beam energies, which causes the production of more secondary ions.

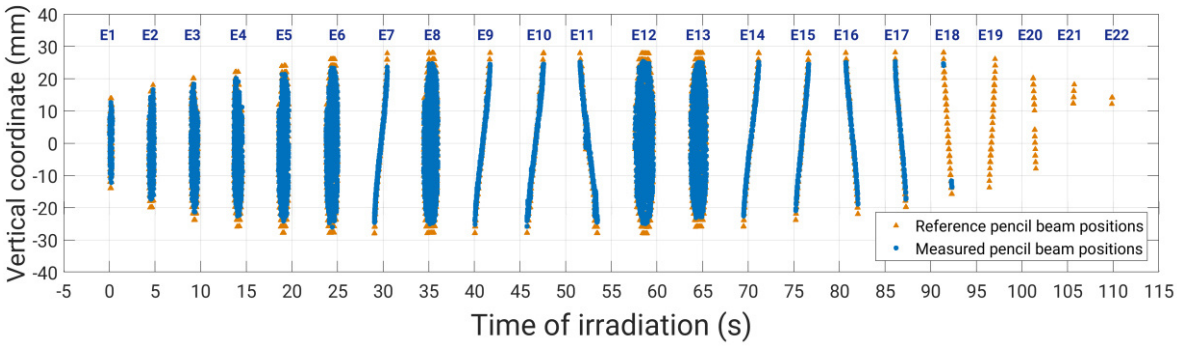

Figure 4.7. Comparison of measured (blue points) and reference (orange triangles) pencil beam positions in the vertical coordinate. The lack of measured beam position is visible due to the high fluence rate detected.

With this situation, only 9538 out of 10218 pencil beam positions with measured ion tracks were compared. Thus this situation was the motivation for optimizing the distance between the tracking system and the isocenter and for improving both hardware and software to reach an optimal operation to detect the secondary ions and to evaluate the performance of the method.

In order to overcome these issues, improvements in the hardware of the detector and in the data analysis algorithms were performed. The improvements are listed as follows:

a) **Hardware-related improvements:**
   - The synchronization chip board of both AdvaPIX TPX3 modules was changed for a new PCB board. This board was designed and manufactured by ADVACAM s.r.o., located in Prague, Czech Republic.
   - With the new chip board, the trigger signals were changed from CMOS (Complementary Metal-Oxide-Semiconductor) logic to LVDS (Low-Voltage Differential Signaling) for a robust synchronization, where the edge speed in the 20% to 90% rise/fall time, in contrast to that for CMOS logic of 10% and 90% rise/fall time. The terminations of the signals were also improved.
   - A device-ready signal device was introduced. This device allows the modules to start in an arbitrary order, with the master module waiting for the slave module to be ready for data acquisition.

b) **Software-related improvements:**
   - The clusterization algorithm was improved. The time window was set to 150 ns, which is the time difference limit between the pixels to be considered as part of the same cluster.
   - The coincidence finding process was also improved based on ten parameters of the clusters. The coincidence time window was set to ±50 ns.

- The ten cluster parameters were used to discriminate and resolve ambiguous coincidences. In the case of the acquired data from the TP2 delivery, Figure 4.7 shows the efficiency of resolving ambiguous coincidences according to different coincidence time windows.

In order to find the optimal performance of the improved coincidence algorithm, different coincidence time windows were evaluated. In Figure 4.8. (a), the amount of single- and multi-clusters coincidence is shown. Considering the plateau region of the amount of matched single clusters (blue curve), the coincidence time window of ±50 ns was chosen. Figure 4.8 (b) shows the amount of matched multi-clusters that were resolved according to the ten cluster parameters mentioned in section 3.5.1. With a coincidence time window of ±50 ns, it is possible to resolve 95% of the matched multi-clusters. The efficiency of the improved coincidence algorithm is shown in Figure 4.8 (c). For coincidence time windows greater than 80 s, the efficiency of matching single clusters decreases. This means, that different single clusters can be mistakenly evaluated as one bigger cluster.

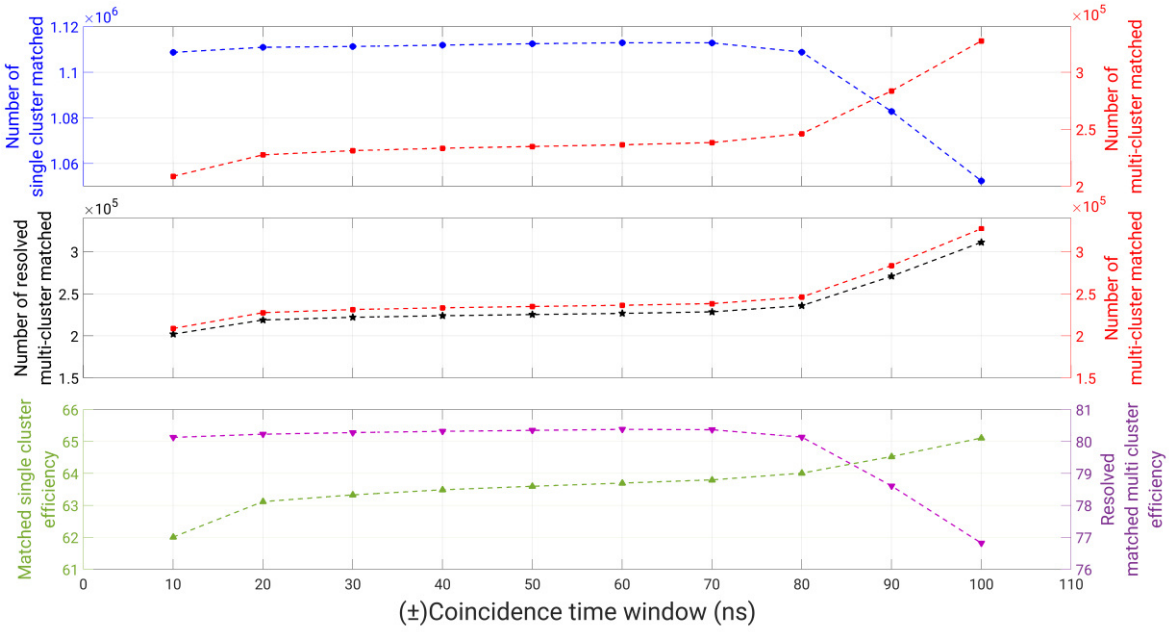

Figure 4.8. (a) Single and multi-clusters in the coincidence process. (b) Matched multi-clusters resolved with the improved coincidence algorithm. (c) Efficiency of the improved coincidence algorithm to resolve multi-clusters. Different coincidence time windows were evaluated.

As seen in Figure 4.8, the coincidence time window of ±80 ns is apparently a breaking point for all the distributions. This is due to the fact that two or more clusters can be taken as one single cluster, which is reflected in the decreasing number of matched single clusters part of the blue curve in Figure 4.8 (a). Although the resolved matched

multi-clusters increases as shown in the black curve in Figure 4.8 (b), the number of matched multi-clusters also increases as seen in the red curve in Figure 4.8 (b). Furthermore, as the coincidence time window increases, the efficiency of resolving matched multi-clusters decreases, because more clusters are considered as one. Therefore, the coincidence time windows of ±50 ns was chosen.

The distance optimization was performed in order to avoid future technical issues due to the secondary-ion signal, since the total number of beam energies in each treatment plan differs according to the tumor volume: 22 and 15 beam energies for the TP1 and TP2, respectively. The number of beam energies depends on the tumor size in order to properly cover it. The found results in this experiment were analyzed with the improvements in both hardware and software.

4.2.1. Comparison of the results with the tracking system positioned at 30° and 0° relative to the beam axis

The measured lateral beam positions when positioning the tracking system at 0° relative to the beam axis were compared to those for the tracking system placed at 30° relative to the beam axis, found in section 4.1. Here, the TP1 was compared. Table 4.1 shows the parameters used this comparison. In order to avoid pile-up effect of the signals due to the extremely high fluence rates, the distance of the tracking system to the isocenter was increased 3 times, and the coincidence window was decreased.

Table 4.1 Parameters used in the comparison of the results for the positioning angle of the tracking system of 30° and 0° relative to the beam axis.

	Tracking system position relative to the beam axis	
Parameter	**30°**	**0°**
Coincidence analysis	Based on arrival time	Based on arrival time and dissimilarities
Coincidence time window (ns)	±75	±50
Distance to isocenter (mm)	12	35
Reference pencil beam positions	MWPC2	
Back-projection plane location	Isocenter	
Analyzed coordinate	Vertical	
Analyzed central region (mm)	±3	
Constraint in number of tracks per time group	< 8	None

The number of ambiguous coincidences at the positioning angle of 0° is up to 18% higher than that at 30°. Moreover, in order to assess the improvements introduced by the new coincidence algorithm (see section 3.5.1), the measured lateral beam positions with the

tracking system placed at 0° were analyzed with both new and old coincidence algorithms. Afterwards, the quantitative comparison of the measured lateral beam positions with the tracking system in both positions was performed. Figure 4.9 shows the precision and accuracy found in this comparison.

As seen in Figures 4.9 (a) and (b), the positioning angle of the tracking system at 0° relative to the beam axis has an impact on both precision and accuracy values. On the first look it apparent, that while the majority of the precision and accuracy values are below the clinically accepted uncertainties of 1 mm, only the two points belonging to the last two energy layers are close to this value.

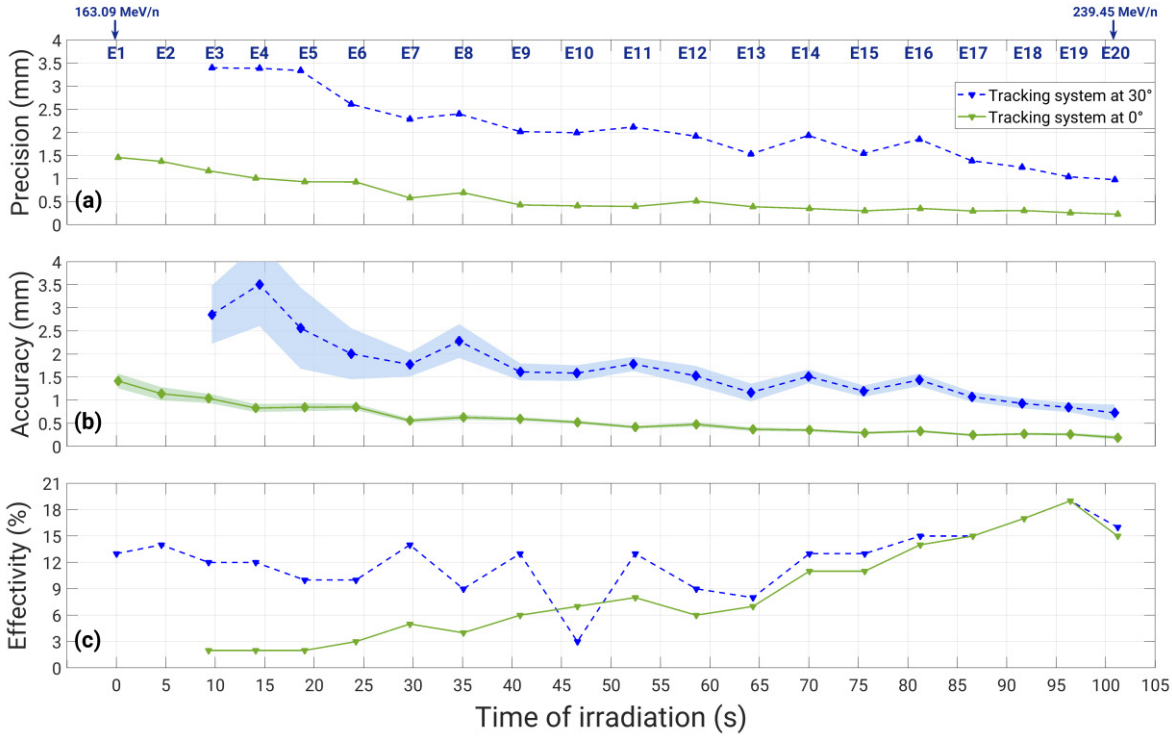

Figure 4.9. Comparison of measured lateral beam positions within the ±3-mm central region at positioning angles at 0° (solid green lines) and 30° (dashed blue lines), in terms of (a) precision and (b) accuracy. Shaded color areas indicate the uncertainties of the accuracy. (c) Effectivity of the method in each beam energy in terms of percentage of accessible pencil beams.

According to Figure 4.9 (a), the precision ranges from 0.23 mm to 1.46 mm (green upward triangles) with the tracking system at 0°, compared to precision at 30° ranging from 0.98 mm to 3.39 mm (blue upward triangles). This represent an improvement up to a factor of 4. At positioning angle of 0°, the accuracy shown in Figure 4.9 (b) goes from 0.19 mm to 1.41 mm (green diamonds), in contrast to the accuracy at 30° that ranges 0.75 mm to 3.51 mm (blue diamonds). The found values translate to an improvement up to a factor of 7.

The number of tracked secondary ion at 0° is one order of magnitude higher than that at 30°. This is reflected in the decrease of the statistical uncertainties of the data. Moreover, the first two beam energies can be accessed.

In addition, the effectivity (percentage of analyzed beam positions over the total number of beam positions) within the selected central region is shown in Figure 4.9 (c). It can be seen an increase of analyzed lateral beam positions up to 8 times more when placing the tracking system at 0° (green downward triangles) compared to 30° (blue downward triangles). The average effectivity was found to increase from 9% (tracking system at 30°) to 13% (tracking system at 0°). This is a consequence of the increase of the number of measured secondary ion tracks by more than one order of magnitude. Therefore, only by changing the position of the tracking system and optimally adjusting the isocenter-to-tracking system distance, an increase overall of 44% in the effectivity could be reached.

4.2.2. Performance of the method for a real clinical treatment plan

In order to further evaluate the capabilities of the proposed monitoring methodology, a treatment plan designed for a clinical delivery to a real patient was used (see section 3.2).

In this study, the tracking system was positioned at 28 cm downstream of the isocenter. Different back-projection planes transverse to the beam axis were considered to evaluate the impact of the back-projection plane depth on both precision and accuracy values. Besides the located plane at the isocenter, depths at 30 mm, 40 mm, 50 mm, 60 mm and 70 mm were assessed.

As mentioned in section 4.1.2, a "shrinkage" of the data points which are most distant from the isocenter is seen when ion tracks are back-projected onto the transverse plane located at the isocenter.

In Figure 4.10 (a), the "shrunk" distribution of measured lateral beam positions (blue points) is seen, with respect to the reference lateral beam positions (black triangles), for the back-projection plane at the isocenter. By back-projecting the ion tracks onto the transverse plane at 50 mm upstream the isocenter, the systematic underestimation of the pencil beam positions located at the outer edges of the treatment field due to the "shrinkage" is overcome, as shown in Figure 4.10. (b). Hence, no central region is needed to be selected for the analysis anymore. This, together with the very much-increased number of ion tracks for the pencil beam positions, allowed us to analyze all pencil beam positions within the entire tumor volume, according to the field under investigation (field at 0° as mentioned in section 3.2).

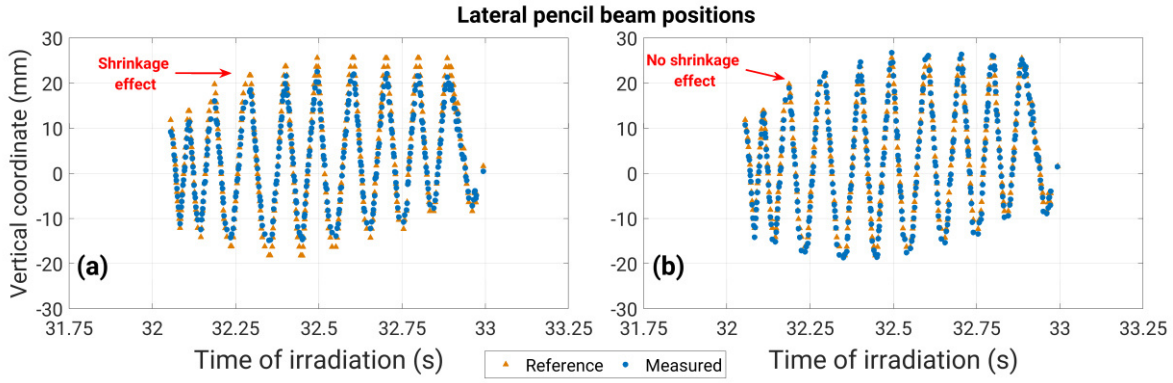

Figure 4.10. Distribution of measured (blue points) and reference (black triangles) lateral beam positions using back-projection planes located at (a) the isocenter and (b) at 50 mm upstream of the isocenter. The depicted beam energy is the corresponding to a value of 194.87 MeV/n of the TP2.

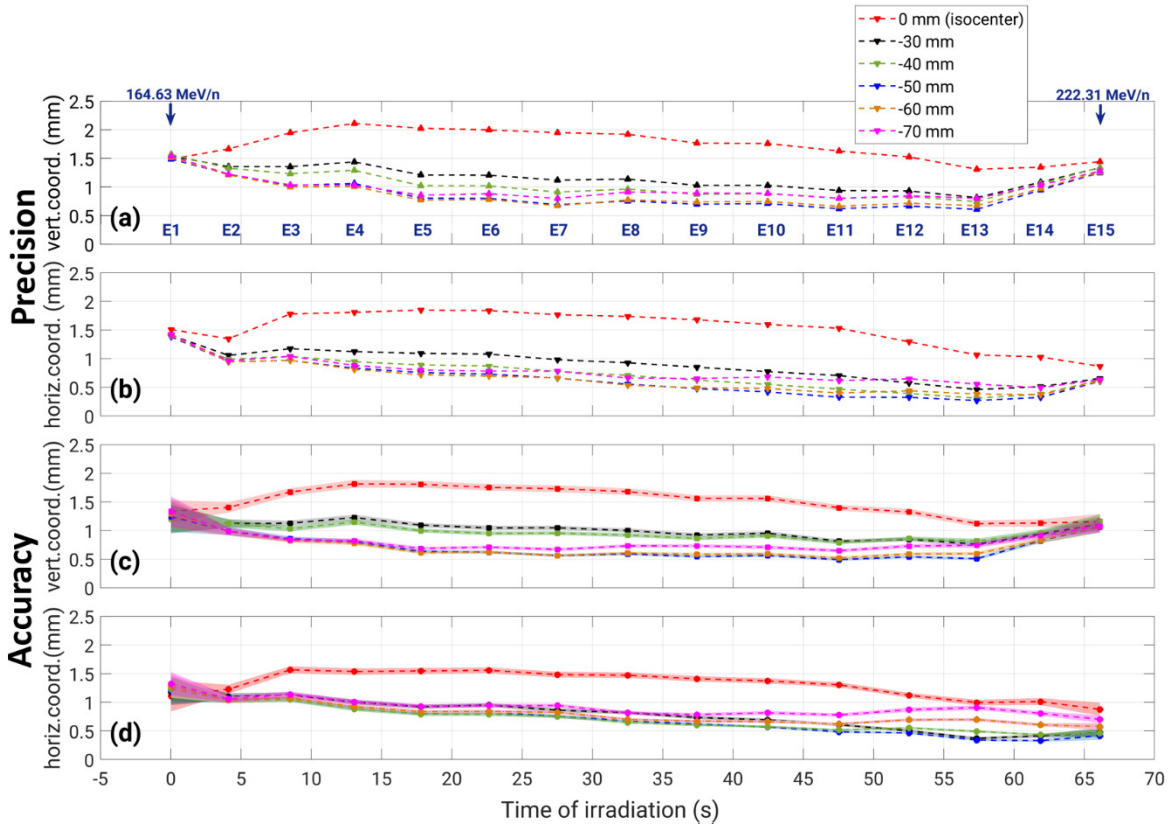

Figure 4.11. Precision in the (a) vertical and (b) horizontal coordinates. Accuracy in the (c) vertical and (d) horizontal coordinates. Shaded color areas indicate the uncertainty of the accuracy. The direction upstream of the isocenter is indicated by the minus sign in the legend.

The precision and accuracy of the method were then evaluated using different positions of the back-projection planes, which are always perpendicular to the beam axis. In Figure 4.11, it can be clearly seen that the plane at -50 cm provides the best precision and

accuracy values, while at the isocenter (red curves), shows the most decreased precision and accuracy. The values of precision and accuracy are given in Table 4.2. The precision values for ten out of fifteen beam energies (irradiation times from 15 s to 65 s) are within the clinically accepted uncertainty of 1 mm (see Figure 4.11 (a)). In the case of the horizontal coordinate, the precision values are within the clinically accepted uncertainties for all beam energies, except for the lowest beam energy (see Figure 4.11 (b)).

In the accuracy of the vertical coordinate (see Figure 4.11 (c)) the values corresponding to the lowest and highest beam energy are above 1 mm. The rest of them (thirteen beam energies) are within the clinically accepted uncertainties. In the horizontal axis (see Figure 4.11 (d)), the accuracy values for fourteen out of fifteen beam energies are below 1 mm, except for the lowest beam energy.

Table 4.2. Ranges of precision and accuracy values at different depths of back-projection planes transverse to the beam axis. Highest values are indicated in blue, corresponding to back-projection plane located at 50 mm upstream of the isocenter.

Parameter	**Depth of back-projection plane with respect to isocenter (mm)**					
	0	**-30**	**-40**	**-50**	**-60**	**-70**
Precision in vertical axis (mm)	1.31 to 2.11	0.82 to 1.55	0.75 to 1.57	0.61 to 1.49	0.67 to 1.52	0.80 to 1.54
Precision in horiz axis (mm)	0.87 to 1.85	0.46 to 1.41	0.31 to 1.40	0.27 to 1.39	0.37 to 1.41	0.50 to 1.43
Accuracy in vertical axis (mm)	1.12 to 1.82	0.82 to 1.23	0.79 to 1.20	0.49 to 1.23	0.52 to 1.29	0.65 to 1.33
Accuracy in horiz axis (mm)	0.88 to 1.57	0.37 to 1.18	0.43 to 1.23	0.33 to 1.20	0.58 to 1.28	0.70 to 1.33

Figure 4.12 shows the minimum and maximum values for the precision and the accuracy. It is clearly seen, that the back-projection plane at the depth of 50 mm upstream of the isocenter gives the highest minimum and maximum values of the precision in both the vertical and horizontal coordinates (see Figure 4.12 left). The highest minimum and maximum values of the accuracy for both coordinates are reached at this back-projection of 50 mm (see figure 4.12 right). This plane provides the highest precision and accuracy values of the monitoring method for the specific treatment plan (TP2). Therefore, the positioning of the tracking system at the beam axis and the optimized depth of the back-projection plane (50 mm upstream of the isocenter), allow us to cover the entire treatment volume with only a 2-cm^2 sensitive detection area, and to improve the precision and the accuracy in 71% and 85%, respectively, compared to the tracking system positioned at 30° from the beam axis.

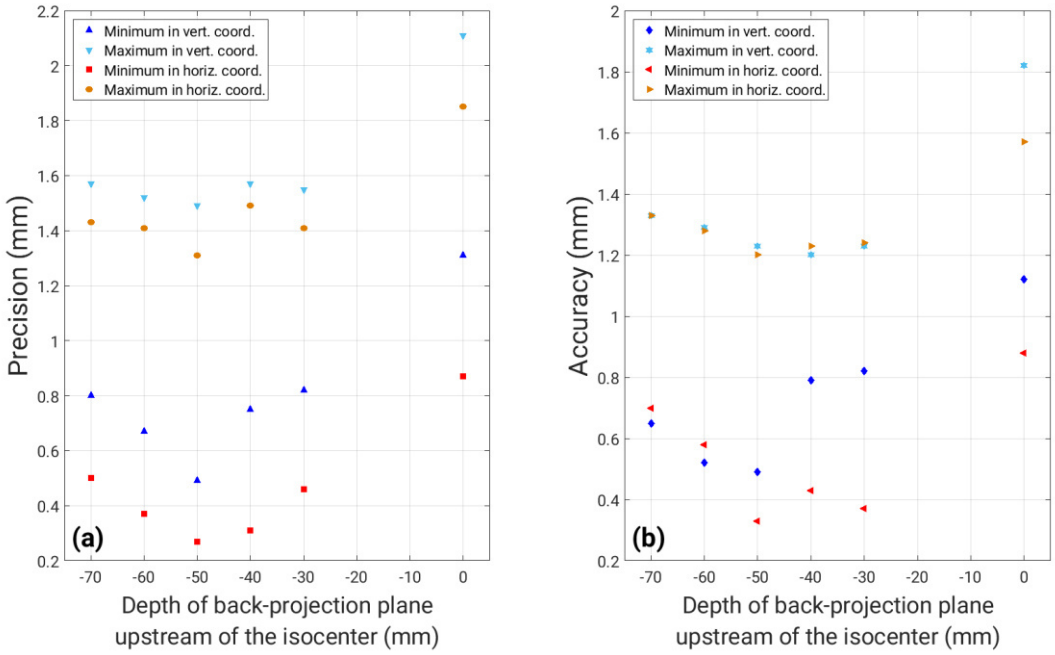

Figure 4.12. Minimum and maximum values of precision (left) and accuracy (right) of the method for the treatment plan TP2.

The access to pencil beam positions located in the lowest beam energies is possible in contrast to the tracking system positioned at 30° from the beam axis (see section 4.1). Moreover, the position of the tracking system at the beam axis allowed a quantitative evaluation of both vertical and horizontal coordinates, which was not possible in section 4.1 due to geometrical uncertainties when positioning the tracking system at 30°.

The effectivity of the method is shown in Figure 4.13 (blue curve). The 100% of pencil beam positions were successfully analyzed for all beam energies, which means that the assessment could be performed over the entire tumor volume. This result supports the motivation of positioning the tracking system directly at the beam axis.

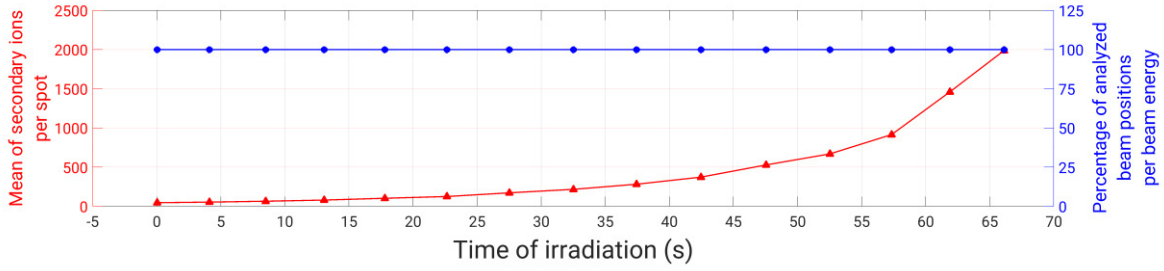

Figure 4.13. Effectivity (blue curve) in terms of successfully accessed pencil beams, which is 100% for all beam energies. Mean of tracked secondary ions per spot position (red curve).

The mean number of tracked secondary ions per position was also quantified. As seen in Figure 4.13 (red curve), an increasing trends when increasing the beam energy is clearly observed. This is related to the increased number of delivered primary carbon ions at the distal boundary of the tumor volume.

In addition, the measured and reference lateral beam positions were compared in the transverse plane to the beam axis. Figure 4.14 shows the beam's eye view of each beam energy used in the TP2. In Figure 4.14, the pattern that follows the beam scanning is seen. Moreover, the measured lateral beam positions reproduce that pattern very well. According to the reference positions, some beam energies exhibit a vertical scanning movement, and other beam energies present a horizontal movement. The measured lateral beam positions follow these direction changes. Thus, the proposed monitoring methodology is capable of reproducing the changes in the beam scanning direction during the treatment delivery.

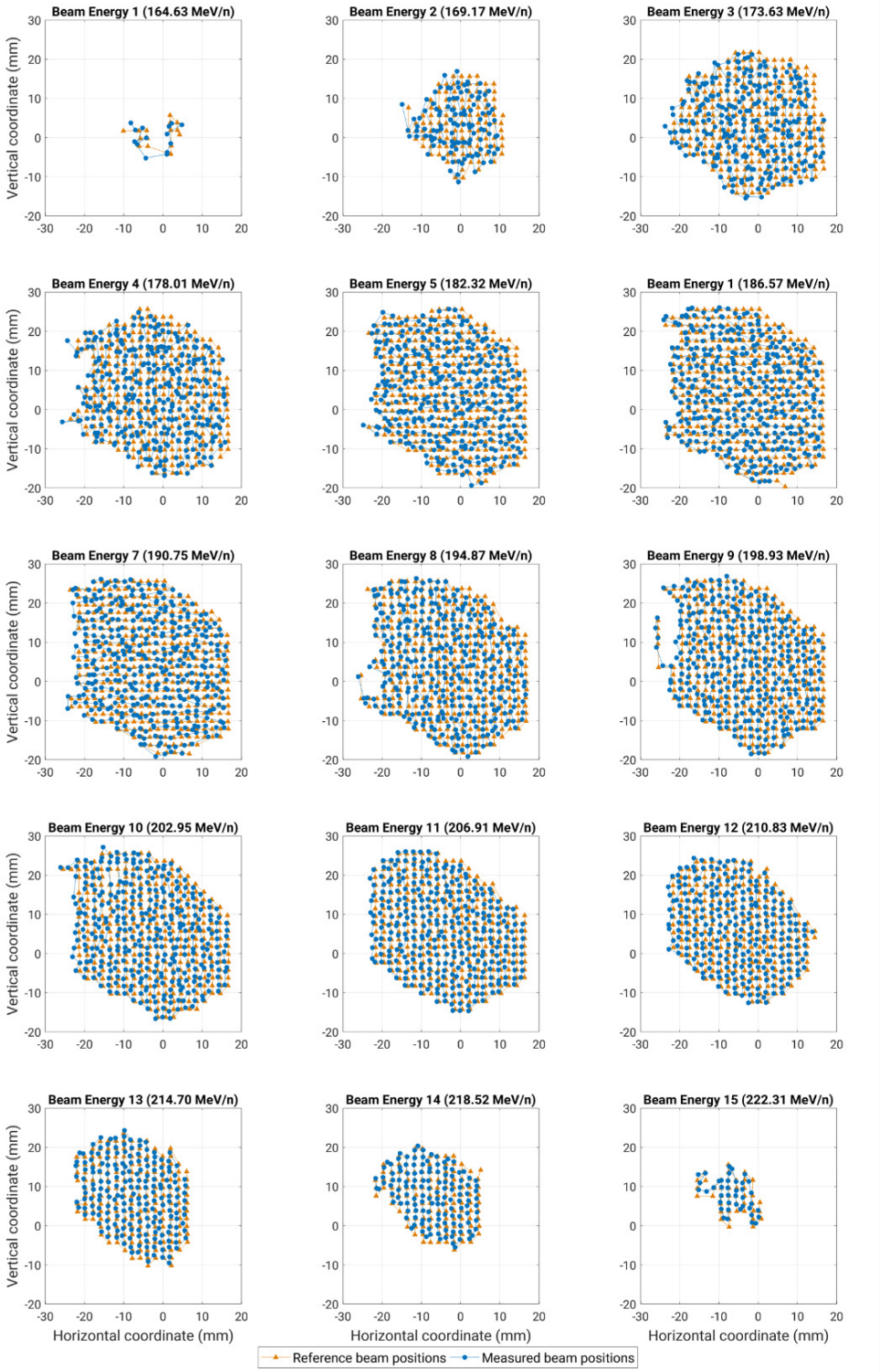

Figure 4.14. Beam's eye view of measured (blue points) and reference (orange triangles) lateral beam positions for each beam energy used in the evaluated treatment plan TP2. The back-projection plane is located at a depth of 50 mm upstream of the isocenter. The beam scanning movement (horizontal or vertical) can be clearly distinguished.

4.2.3. Discussion to the monitoring performance with tracking system positioned at 0°

Part A: Comparison of the results for tracking system positions at 30° and 0°

The improvements found for the tracking system at 0° compared to the monitoring at 30° have shown great benefit in the performance of the method.

The 98% of the ambiguous coincides (due to the higher secondary-ion fluence rate at the detector-positioning angle of 0° relative to the beam axis) could be resolved with the new coincidence algorithm. In doing so, the improvement in precision and accuracy values increases by 15% and 9%, respectively (see section 4.2.1 and Figure 4.9).

Moreover, with the tracking system at 0°, the beam energies E1 and E2, which in the first experiment could not be analyzed, were now accessible evaluated.

The number of tracked secondary ions per primary carbon ion was quantified. With the positioning angle at 30° relative to the beam axis, 17.1×10^{-3} tracked secondary ions per primary carbon ion per solid angle were measured at 12 cm from the isocenter. With the positioning angle at 0°, 4.63 tracked secondary ions per primary carbon ion per solid angle were measured at 35 cm. This represents an increase by a factor of 271.

The 100% of the pencil beam positions within the selected central region of ±3 mm were evaluated. As seen in Figure 4.9 (a) and (b), the precision and accuracy values are below the clinically accepted uncertainties of ±1 mm. Only for the first three beam energies, these values are above 1 mm. This is due to the low amount of tracked secondary ions from these beam energies. The use of larger sensitive detection areas to increase the number of detected secondary ions could eventually improve the precision and accuracy values for the lowest beam energies.

Furthermore, the positioning of the tracking system at 0° gives the possibility to measure not only the vertical coordinate, but also the horizontal coordinate simultaneously.

Part B: Performance of the method with a clinical treatment plan

In comparison to the results obtained when positioning the tracking system at 30° relative to the beam axis, the evaluation of the performance of the method was possible for both coordinates (vertical and horizontal) simultaneously with the tracking system positioned at 0° relative to the beam axis. All the pencil beam positions within the central region under investigation could be assessed. The precision and accuracy reached values in line with the clinically accepted uncertainties of ±1 mm. However, this does not hold true for the first two beam energies of the treatment plan TP1. In order to improve the precision and accuracy in these beam energies, larger detection areas have to be considered. The trend shown in Figures 4.9 (a) and (b) indicate the highest values of precision and accuracy, respectively, as the beam energy increases.

An optimization of the back-projection plane depth was performed for the monitoring at 0° for the delivery of the treatment plan TP2. Further improvements were reached by an optimization of the position of the back-projection plane along the beam axis. At the back-projection plane located at 50 cm upstream of the isocenter, it was possible to reach the highest values of precision and accuracy for both coordinates, enabling us to evaluate the 100% of the total pencil beam positions of the treatment plan (TP2), i.e., in the entire tumor volume. Thus, by using this real clinical treatment plan TP2 delivered to a head phantom, with different internal structures and inhomogeneities, the performance of the method was tested in a worst-case scenario.

The situation of delivering a real clinical treatment plan to the head phantom translate in uncertainties in the rising part observed in Figures 4.14 (a) and (b), belonging to the beam energies E13 to E15. Another reason of the decreased precision and accuracy in the vertical coordinate might be the suboptimal location of the back-projection plane compared to the generation point of most of the detected secondary ions of this specific beam energy. This issue could eventually be overcome by an optimization of black-projection planes for each individual beam energy separately. This issue could be eventually overcome under the consideration of black-projection planes for each individual beam energy.

For the first beam energies of the treatment plan TP2 shown in Figure 4.11, the obtained values of precision an accuracy in both coordinates are in the order of those values obtained in the comparison of the monitoring at 30° and 0°. The cause of the decreased precision an accuracy is related to the low number of tracked secondary ions. This is due to the low total number of secondary ions created and their decreased range in the phantom caused by their low velocities at the time of their production. Moreover, the angular distribution of these secondary ions is at broadest due to the angular distribution originating from the nuclear interaction and the increased multiple Coulomb scattering in the phantom given by their low energies. This issue can be improved by the use of larger sensitive detection areas in the tracking system.

Some systematic uncertainties can be observed in the last subplots of Figure 4.14 that correspond to beam energies 11-15. These systematic uncertainties could be due to minor remaining uncertainties in the detector alignment, which is a very sensitive parameter of the experimental setup. Another source of uncertainties is the different internal geometry between a patient and the head phantom for the planning and the delivery of the treatment plan. Nevertheless, when the treatment plan is delivered, which not correspond to the irradiated geometry, the proposed method exhibited a well performance for this situation. Hence, it is expected this methodology to reach an optimal performance on a wide range of variety of real patient treatment plan and geometries.

As aforementioned, the observed remaining uncertainties could potentially be overcome by using optimized back-projection planes for each single beam energy. With this, precision and accuracy could be further improved, reaching values within the clinically accepted uncertainties for all beam energies.

From the findings of the monitoring at 0° relative to the beam axis, the developed methodology has been shown to deliver a clinically relevant information with a clinically relevant performance even though a worst-case scenario is being evaluated. Thus, the method is an independent and complementary technique to monitor the lateral pencil beam positions in a non-invasive manner.

4.3. First clinical measurement during a patient treatment

The performance of the proposed methodology was evaluated in the first clinical monitoring of lateral pencil beam positions by means of secondary ion tracking at the Heidelberg Ion-Beam Therapy Center. This clinical application was measured in a head-and-neck patient with a tumor volume of 73.85 cm^3 treated with two fields at the angles of 5° and 330°. The field at 5° was assessed.

4.3.1. Testing the influence of the monitoring system on the beam monitoring system

Prior to the clinical application, measurements to investigate the possible influence of the medical cart, containing the hardware for a remote operation and carrying the tracking system (see section 3.4.3), on the BAMS inside the beam nozzle were carried out. The medical cart was placed as close as possible to the beam nozzle, in contrast to the later clinical situation, as shown in Figure 4.15.

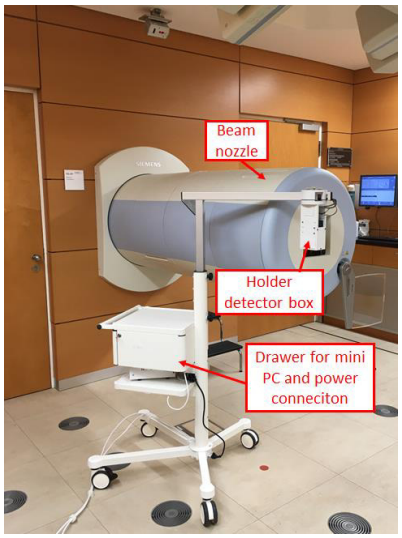

Figure 4.15. Position of the medical cart with respect to the beam nozzle for testing the influence on the beam monitoring system. These measurements were performed in one of the treatment rooms at the HIT facility.

During the irradiation, the BAMS signal was monitored continuously using the EtherCAT system in order to detect possible anomalies, in particular peaks or oscillations in

the signal. Afterwards, the acquired results were compared to results of reference measurements where the medical cart was not located inside the treatment room. These measurements and their analysis were supported by medical physicist of the HIT facility

The resulting differences in terms of beam size and beam position were found to be in the range of the usual fluctuations, as shown in Figure 4.16. Beam sizes and positions were also measured by the MWPC3. No significant influences of the medical cart on the BAMS were found. Moreover, no significant changes on the offsets and thresholds of the ionization chambers were found.

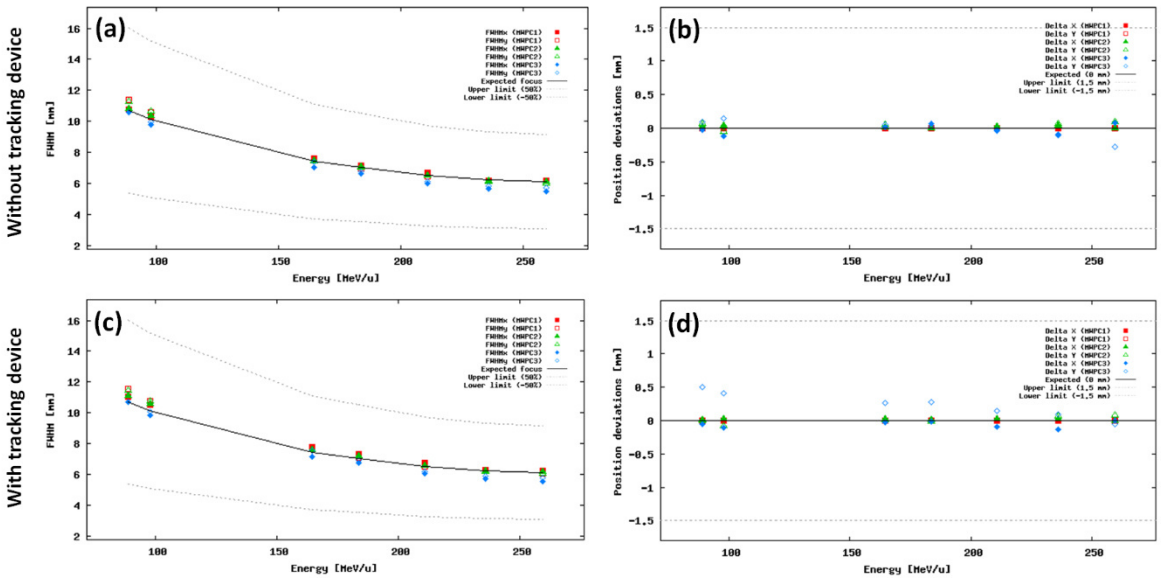

Figure 4.16. Influence measurements on the (a) beam size and (b) beam positions when the medical cart is not at the treatment room. Measurements of (c) beam size and (d) beam positions with the medical cart next to the beam nozzle. Dashed lines indicate the tolerance limits in these influence measurements. Solid black lines indicate the expected values. The beam energy ranges correspond to the used beam energies in the clinical treatment delivery. Courtesy of Dr. Marcus Winter.

4.3.2. Delivery of the treatment plan to the patient

Having fulfilled the requirements concerning the influence on the BAMS, as well as safety electrical protection of the medical cart and each device within it, the tracking device was accepted to be used during the clinical treatment delivery. As the patient measurements was performed before the methodology for the measurement at the beam was developed, the tracking system was positioned at 30° relative to the beam axis. The distance to the isocenter was 16 cm. This gave us a distance window of 5 cm between the head of the patient and the tracking system cover (see Figure 3.10). This distance window was the minimum allowed by the medical physicists. The references pencil

beam positions were obtained from the MWPC3 measurements at the isocenter, which were performed one day before the patient treatment.

As explained in section 4.1.1, due to the geometry of the experimental configuration at 30°, the analysis of the lateral pencil beam positions was performed in the vertical coordinate only. The calculation of the measured lateral beam positions was performed in the same manner as described in detail in section 4.1 (also see section 3.5). The constraint of eight ion tracks per pencil beam was also applied in this case. Figure 4.17 shows the comparison of measured and reference lateral pencil beam positions.

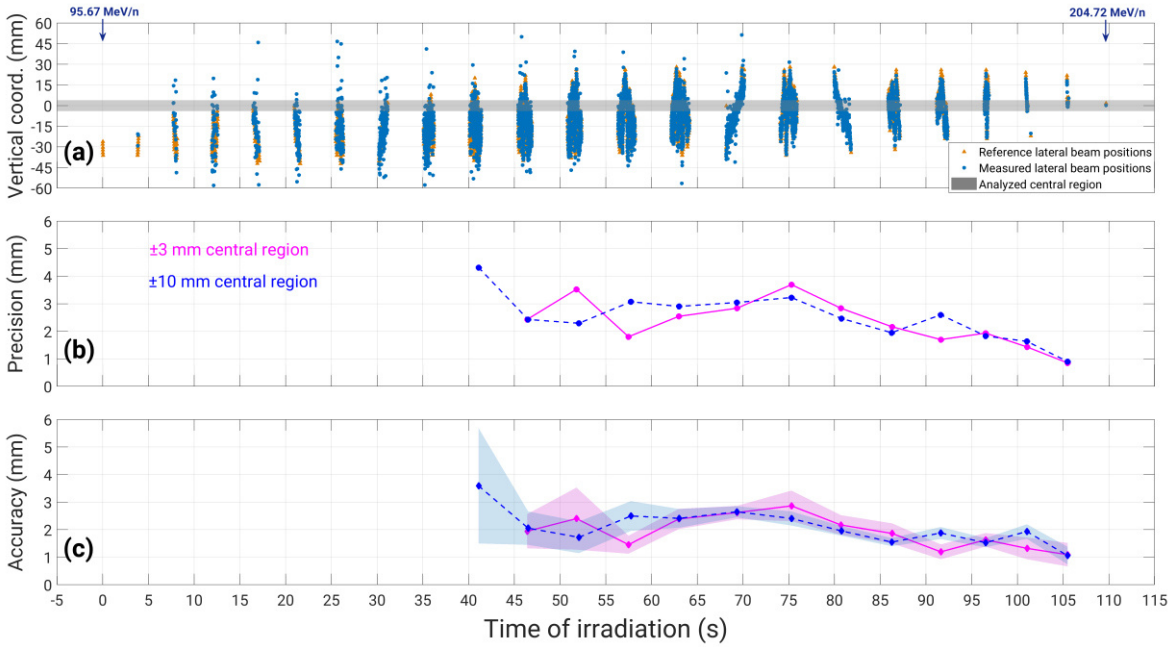

Figure 4.17. (a) Comparison of reference (black triangles) and measured (blue points) pencil beam positions in the vertical coordinate. Shaded area represents the ±10 mm central region under investigation. (b) Precision and (c) accuracy when considering pencil beam positions in central region of ±3 mm (pink curves) and ±10 mm (blue curves). Beam energies with irradiation times before 40 s are not evaluated due to applied constraint in the number of tracks per pencil beam.

The twenty-three beam energies can be clearly seen in Figure 4.17 (a). As in section 4.1.2, the pencil beams with positions in a central region were selected for the evaluation of the method in terms of precision and accuracy, as shown by the shaded pink area in Figure 4.17 (a). For that, two sizes of central regions were investigated: ±3 mm and ±10 mm.

Differences between reference and measured lateral beam positions were calculated for each beam energy. From the difference distributions, precision and accuracy were cal-

culated (see section 3.5.3). Figures 4.17 (b) and (c) shows the obtained precision and accuracy, respectively, for the selected central regions of ±3 mm (pink curves) and ±10 mm (blue curves).

Only few measured lateral beam positions are present in irradiation times between 0 s and 5 s. The reason is the low energy of the incoming beam (95.67 MeV/n and 102.22 MeV/n), where less secondary ions are produced and most of them could not leave the head.

Due to the selected central regions and the applied constraint on the track number per pencil beam, beam energies below irradiation times of 40 s could not be analyzed. For the analyzed beam energies, precision values for the ±3-mm central region were found to range from 0.85 mm to 3.69 mm. For the ±10-mm central region, the values go from 0.90 mm to 4.31 mm. In the case of accuracy, it ranges from 1.09 mm to 2.87 mm within the ±3-mm central region, and from 1.06 mm to 3.59 mm in the ±10-mm central region.

The obtained precision and accuracy values are similar to the results from the monitoring at 30° (see section 4.1.2), reaching the clinically accepted uncertainties (±1 mm) in the highest beam energy evaluated. Moreover, the reference pencil beam positions that were measured the day before the treatment delivery (with the MWPC3 placed at the isocenter) could be the reason for remaining uncertainties.

4.3.3. Discussion to the findings of the first clinical application of the method

In this measurement, the developed methodology was investigated for the first time during a real clinical patient treatment.

The obtained precision and accuracy values within the assessed central regions are in agreement with those obtained in section 4.1 (see Figure 4.17 (b) and (c)). In particular, the precision and accuracy for the highest beam energies (E21 and E22) are in line with the clinically accepted uncertainties.

In general, when the tracking system is positioned at 30° from the beam axis, the low amount of tracked secondary ions coming from the lowest beam energies is the main drawback. The shallow location of the tumor volume, as shown in the CT image in Figure 3.3 (c) of this clinical treatment plan represented a particularly challenge for the configuration for pencil beam monitoring. The low yield of tracked secondary ions was found between the beam energies E1 to E8 with values of 95.67 MeV/n to 136.92 MeV/n. No secondary ion tracks were detected from the first beam energy. Moreover, secondary ion tracks were detected for only three pencil beam positions in the second beam energy. This can be explained by the low number and the low energy of secondary ions produced at those beam energies that could not leave the patient. Another contribution to this effect is that the secondary ions that could leave the patient were stronger affected by multiple Coulomb scattering due to the lower secondary ion energies, and they could

not reach the sensitive detection areas. The low number of secondary ions could eventually be increased by decreasing the positioning angle of the tracking system relative to the beam axis.

Although the position of the tracking system for the first and second experiment was investigated for the specific location of the tumor according to the TP1 and TP2 (30° and 0° from the beam axis, respectively), the position of the tracking system for this clinical treatment delivery was not the optimal due to the shallow location of the tumor. For all tumor positions and shapes, the positioning of the tracking system at the beam axis (0°) will be the best. At this initial stage of the performance of this monitoring methodology, further clinical measurements should be performed with a tumor location similar to the presented in the TP2. Still, the position of the tracking system has to be further investigated.

4.4. Overall discussion and outlook

For the presented monitoring methodology, the found values of precision and accuracy were superior when the tracking system was positioned at 0° relative to the beam axis, compared to the results at 30°. Moreover, they are within the clinically accepted uncertainties of ±1 mm, even in a worst-case scenario (see section 4.2).

For the tracking system positioned at 30° from the beam axis (see sections 4.1 and 4.3), the precision and accuracy were in line with the clinically accepted uncertainties only for the highest beam energies. The main reason of the increased values at lower beam energies is the low number of detected secondary ions due to the small sensitive detection area (2 cm^2). Moreover, the number of produced secondary ions is lower due to the number of primary carbon ions sent per spot in those beam energies. Additionally, the energy of the secondary ions is lower due to the low energy of the primary carbon ions. Therefore, most of the produced secondary ions are stopped within the patient and the remaining ions undergo increased multiple Coulomb scattering due to their low energy. The precision and accuracy values can potentially be improved by increasing the sensitive detection area. This can be reached by constructing a detector with a larger detection area, e.g., using laterally touching mini-trackers. Interestingly, the larger areas are needed just to increase the amount of secondary ions, not to increase the effectivity of the method in terms of accessible pencil beams, since this has already reached the 100% with the used mini tracking system (2 cm^2) positioned at the beam axis. Positioning tracking systems off the beam axis would lead to a decreased number of secondary ions, but the beam range could potentially be monitored [Dauvergne et al, 2009; Amaldi et al, 2010; Gwosch et al, 2013; Piersanti et al, 2014; Gaa et al, 2017; Reinhart et al, 2017; Bisogni, 2019; Félix-Bautista et al, 2019].

In the frame of hypofractionated carbon-ion beam radiotherapy, higher fraction doses (8 Gy(RBE)) are delivered compared to standard fraction doses (3 Gy (RBE)) [Jensen et

al, 2011]. In this case, an increased number of primary carbon ions are delivered per spot, which can be translated into an increased yield of secondary ions. This higher number of secondary ions can potentially improve the precision and accuracy of the method.

The alignment of the tracking system positioned at 30° relative to the beam axis (see section 4.1) could not performed with the laser system of the experimental room in a straightforward way. Instead, the fine alignment of the detection layers was performed offline by tilting the sensitive areas of detection to compensate the minor residual misalignments. In section 4.2 corresponding to the tracking system positioned at 0° relative to the beam axis, the alignment was performed according to the laser system of the experimental room. Moreover, a carbon-ion beam with the highest energy available at HIT (430 MeV/n) was delivered at the isocenter (0,0) for a fine alignment of both sensitive detection layers of the tracking system. For the beam monitoring during the patient treatment (see section 4.3), the alignment in the treatment room was performed by using rulers attached to the arm of the monitoring system with respect to the laser system in the treatment room. A more dedicated alignment system could potentially improve the performance of the method for both positions of the tracking system.

In this thesis, the performance of the method was investigated on three treatment plans – a simple one (TP1), a realistic one (TP3) and the worse case (TP2). In future clinical measurements the values of precision and accuracy could be different due to different tumor locations and sizes, and the number of primary ions sent per spot. For instance, at low beam energies, some secondary ions either can stop inside the patient or can leave the patient in directions different to the detector position due to the multiple Coulomb scattering, as mentioned in section 4.3. Another reason could be the heterogeneity inside the patient, especially for head-and-neck tumors, where air cavities are present. Here, the secondary ion detection based on Timepix3 detectors could be combined with the detection of prompt photons as a possibility to complement the information on the pencil beam positions at low beam energies.

Since the Timepix3 detectors have the advantage of simultaneous measurements of ion's arrival time and energy deposition, they are an attractive tool for the beam monitoring. Scintillators detectors [Henriquet et al, 2012; Rucinsky et al, 2018, Traini et al, 2019; Bisogni, 2019] and monolithic pixel detectors [Spiriti et al, 2017; Reidel et al, 2019] have been used experiments for ion beam range monitoring to track secondary ions in carbon-ion irradiations. Nevertheless, compared to the number of sensitive layers used in Reidel et al, 2019 and Traini et al, 2019, for the scintillating detector fiber trackers, the advantage of Timepix detector family is the use of two sensitive layers in the minitracker, which are sufficient for tracking. This is due to the 2-dimentional information (pixels), fine-timing information and hit detection efficiency close to 100%.

So far, there are no reported techniques to independently monitor the lateral pencil beam positions in the patient during treatment deliveries of carbon-ion beam radiotherapy. The existing techniques based on secondary radiation detection, like PET-signal,

prompt gamma and secondary ions, are being evaluated ion range verification [Kraan, 2015; Muraro et al, 2016]. A lateral pencil beam monitoring is currently not feasible due to a spot-by-spot information loss, as reported for proton beam therapy [Richter et al, 2016]. A recent study reported the possibility of a spot-by-spot ion beam range verification based on prompt gamma detection [Xie et al, 2020]. In principle, the presented methodology in this thesis could be used as a spot-by-spot evaluation with the tracking system place at 0°, instead of obtaining the mean spot position in each beam energy layer. Thus, a spot-by-spot beam monitoring could be feasible laterally and longitudinally to the beam axis, since the presented method has the possibility to be applied for the purpose of the ion range verification, as mentioned above.

Since secondary ions are produced for all primary ions heavier than protons, in future research it has to be investigated whether this methodology could be used for the beam monitoring in helium- or oxygen-ion beam therapy. The helium-ion beam treatments are planned to start at the HIT facility in the near future. In this case, the presented monitoring methodology could eventually be integrated together with the workflow of helium-ion radiography [Gehrke et al, 2018; Martišíková et al, 2018].

The developed monitoring methodology presented in this thesis has shown results of clinical relevance and is ready to evaluate its performance with different tumor locations within a large group of patients in a clinical study in the future. Moreover, this monitoring methodology can potentially be upgraded for an online monitoring in the future. For that, an automatic interlock can be integrated in the future into the accelerator system, in order to stop the beam in case of larger differences of the pencil beam positions with respect to the planned values. For online monitoring, the fast development of the state-of-the-art computational devices in technological and computer sciences could be used in the future to provide sufficient speed for the performance of online data evaluation [Fiorino et al, 2020].

Chapter 5

Summary

In this thesis, the development of a methodology to monitor the lateral pencil beam positions based on the tracking of secondary ion leaving an irradiated object is presented. Aiming at the monitoring of the ion beam scanning at the room isocenter, three main investigations were performed:

i. Experiments in a head phantom with the tracking system positioned at 30° relative to the beam axis
ii. Experiments in the head phantom with the tracking system positioned at 0° relative to the beam axis, divided in two parts:
    a. Comparison with the experiments performed at 30°.
    b. Measurements to assess the capabilities of the monitoring methodology using a real patient treatment plan, presenting a worst-case scenario.
iii. First clinical application during a patient treatment with the tracking system positioned at 30° relative to the beam axis.

Different realistic tumor volumes and geometries were investigated in patient-like models under clinic-like conditions, including typical clinical fraction doses and dose rate. Moreover, the performance of the method was tested in a clinical real patient treatment for the first time. The workflow described in chapter 3 was used in the assessment of the performance of the method in all three aforementioned investigations. The most significant results attained in the investigations are briefly summarized in the following:

Investigation I: Using a tracking system at 30° relative to the beam axis, pencil beams within a central region of ±3 mm were monitored, for the vertical scanning beam direction.

> The **precision** was found to improve as the beam energy increases, ranging from 0.98 mm to 3.39 mm for a single measurement. When six measurements were summed up, mimicking a larger detector area, the precision ranged from 0.84 mm to 2.59 mm, indicating an **improvement from 14% to 24%** compared to those for a single measurement.

The **accuracy** ranged from 0.75 mm to 3.51 mm, when considering a single measurement, and from 2.17 mm to 0.77 mm, when considering six measurements. Additionally, the **reproducibility** ranged from ±0.42 mm up to ±0.07 mm, for the statistics of six measurements.
The method was found to be **capable of detecting differences** between the measured and reference pencil beam positions **down to 0.3 mm**, and has shown **capabilities** of reaching clinically accepted uncertainties of ±1 mm for the highest beam energies. Part of the results of this investigation were already published [Félix-Bautista et al, 2019].

Investigation II: The tracking system was positioned directly at the beam axis downstream of the isocenter.

The technical challenges concerning the high secondary-ion fluence rate were successfully solved. The algorithms for data analysis were also improved.
When comparing the results to the tracking system positioned at 30°, an increase of the number of tracks measured by a factor of **30** was found. At 0°, **both scanning beam directions** –vertical and horizontal– could be evaluated. **Improvements of 71% and 85%** for the precision and accuracy, respectively, were reached.
Moreover, the location of the **back-projection plane** was optimized. For the plane at the depth of **50 mm** upstream of the isocenter, the highest values of precision and accuracy values were reached. Overall **improvements** of 54% and 49% for precision and accuracy, respectively were reached. The method was found to be robust for different depths of the back-projection planes.
For the **vertical** scanning beam direction, the **precision** of 0.61 mm – 1.49 mm, and the **accuracy** of 0.49 mm – 1.24 mm, were found. For the **horizontal** scanning beam direction, the **precision** of 0.27 mm – 1.39 mm, and the **accuracy** of 0.34 mm – 1.20 mm, were found
Additionally, the **sufficient efficiency** was found to access the 100% of all pencil beam positions, i.e., covering the entire tumor volume.
The presented results of precision and accuracy are in line with clinically accepted uncertainties. These results are part of an already provisionally accepted manuscript [Félix-Bautista et al, 2021].

Investigation III: Measurements during a patient treatment. The tracking system was positioned at 30° from the beam axis, as in Investigation I. All technical issues concerning the used of the tracking system during the patient treatment were resolved.

Within the **±3-mm** central region, the **precision** of 0.85 mm – 3.69 mm, and the **accuracy** of 1.09 mm – 2.87 mm, were found. Within the **±10 mm** central region, the **precision** of 0.90 mm – 4.31 mm, and the **accuracy** of 1.06 mm – 3.59 mm, were found.
The shallow tumor site impeded the evaluation of precision and accuracy of low beam energies of the treatment plan.

Overall, the found performance of the new method presented in the investigations of this thesis are in line with the clinically acceptable uncertainties of ±1 mm for the majority of the lateral pencil beam positions for synchrotron-based HIT facility [Jäkel et al, 2001].

Chapter 6
Conclusions

Radiation therapy with ions enables an enhanced conformality of the physical dose distribution to the tumor volume compared to photon radiotherapy. The narrow carbon ions used to decrease the lateral penumbra lead to an increased sensitivity of the dose distribution to fluctuations of the lateral pencil beam positions. This can appear due to the very sensitive beam delivery caused by the required fine-tuning of multiple beam line elements for synchrotrons. Moreover, the limited precision of the position-measuring devices in the beam nozzle is enlarged by the extrapolation of pencil beam positions to the room isocenter, which is larger in synchrotron-based facilities compared to those with cyclotrons. These fluctuations could impair the beam positions at the isocenter affecting the quality of the desired dose distribution. In the frame of adaptive radiotherapy, the beam position measurements are also of great interest, since QA measurements to verify adapted treatment plans are time-consuming. Therefore, new techniques independent of the existing beam monitoring systems are desired to monitor the lateral positions of carbon-ion pencil beams at the room isocenter during treatment deliveries.

The proposed methodology and investigated is an independent strategy to monitor the lateral beam positions at the isocenter. It is based on the detection and tracking of charged nuclear fragments leaving the patient, in order to evaluated the differences between the measured and the reference pencil beam positions in terms of precision, accuracy and effectivity.

In this thesis, a mini-tracker composed of two Timepix3 detectors was used to track the secondary ions. Experiments were designed to mimic realistic situations using a, anthropomorphic head phantom. Moreover, a worst-case scenario was also investigated. For this, treatment plans with realistic tumor volumes, typical clinical fraction doses and dose rates were used. The methodology was also tested in a clinical real patient treatment delivery for the first time at the HIT facility in Heidelberg, Germany.

The obtained results show that the tracking system positioned at 0° provides superior values of precision and accuracy compared to the position at 30° relative from the beam axis. Moreover, the first clinical application of the presented monitoring methodology was carried out. The performance of the developed methodology was found to be in line with the clinical uncertainties of ±1 mm for lateral pencil beam positions accepted at the synchrotron-based HIT facility. Moreover, this methodology has the potential of being included in the QA procedure as a complementary and independent verification of the lateral pencil beam positions during the treatment delivery. Further investigations to improve both precision and accuracy values for the lowest beam energies can be performed with tracking systems with larger detection areas and an optimized back-projection plane for each beam energy layer separately.

Overall, clinically relevant results have been demonstrated for the non-invasive methodology proposed in this thesis to monitor the lateral beam positions in carbon-ion treatment deliveries. It is ready to be further investigated on a wide range of target positions, sizes and doses within a future clinical study. The ethical burden of such a study is particularly low, since the method uses a by-product radiation of the treatment and does not interfere with the clinical devices. An evaluation of this methodology on a larger patient group in a clinical trial is thus the next step in the near future, as well as the upgrade of the system towards an online monitoring.

Bibliography

Actis, O., Meer, D., & König, S. (2014). Precise on-line position measurement for particle therapy. In Journal of Instrumentation (Vol. 9). Institute of Physics Publishing.

Agodi, C., Battistoni, G., Bellini, F., Cirrone, G. A. P., Collamati, F., Cuttone, G., … Voena, C. (2012). Charged particle's flux measurement from PMMA irradiated by 80 MeV/u carbon ion beam. Physics in Medicine and Biology, 57(18), 5667–5678.

Amaldi, U., Hajdas, W., Iliescu, S., Malakhov, N., Samarati, J., Sauli, F., & Watts, D. (2010). Advanced quality assurance for CNAO. In Nuclear Instruments and Methods in Physics Research, Section A: Accelerators, Spectrometers, Detectors and Associated Equipment (Vol. 617, pp. 248–249). Elsevier B.V.

Aricò, G., Gehrke, T., Gallas, R., Mairani, A., Jäkel, O., & Martišíková, M. (2019). Investigation of single carbon ion fragmentation in water and PMMA for hadron therapy. Physics in Medicine and Biology, 64(5).

Battistoni, G., Bellini, F., Bini, F., Collamati, F., Collini, F., De Lucia, E., … Voena, C. (2015). Measurement of charged particle yields from therapeutic beams in view of the design of an innovative hadrontherapy dose monitor. In Journal of Instrumentation (Vol. 10). Institute of Physics Publishing.

Bertolini, G. and Coche, A. Semiconductor Detectors. North-Holland Pub. Co., Amsterdam, 1968.

Bethe, H. (1930). Zur Theorie des Durchgangs schneller Korpuskularstrahlen durch Materie. Annalen Der Physik, 397(3), 325–400.

Bisogni, M. (2019). The INSIDE bimodal system for range monitoring in particle therapy toward clinical validation. Nuclear Instruments and Methods in Physics Research, Section A: Accelerators, Spectrometers, Detectors and Associated Equipment 936, 73–74.

Bizzocchi, N., Fracchiolla, F., Schwarz, M., & Algranati, C. (2017). A fast and reliable method for daily quality assurance in spot scanning proton therapy with a compact and inexpensive phantom. Medical Dosimetry, 42(3), 238–246.

Bloch, F. (1933). Zur Bremsung rasch bewegter Teilchen beim Durchgang durch Materie. Annalen Der Physik, 408(3), 285–320.

Böhlen, T. T., Cerutti, F., Dosanjh, M., Ferrari, A., Gudowska, I., Mairani, A., & Quesada, J. M. (2010). Benchmarking nuclear models of FLUKA and GEANT4 for carbon ion therapy. Physics in Medicine and Biology, 55(19), 5833–5847.

Chu W. T. (2006). Overview of Light-Ion Beam Therapy. ICRU-IAEA Meeting, 16th Jun 2006.

Combs, S.E., Jäkel, O., Haberer, T., and Debus, J. (2010). Particle therapy at the Heidelberg Ion Therapy Center (HIT) - Integrated research-driven university-hospital-based radiation oncology service in Heidelberg, Germany. Radiotherapy and Oncology 95, 41–44.

Combs, S. E., Kessel, K. A., Herfarth, K., Jensen, A., Oertel, S., Blattmann, C., … Debus, J. (2012). Treatment of pediatric patients and young adults with particle therapy at the Heidelberg Ion Therapy Center (HIT): establishment of workflow and initial clinical data. Radiation Oncology, 7(1).

Coutrakon, G. B. (2007). Accelerators for heavy-charged-particle radiation therapy. In Technology in Cancer Research and Treatment (Vol. 6, pp. 49–54). Adenine Press.

Dal Bello, R., Magalhaes Martins, P., Brons, S., Hermann, G., Kihm, T., Seimetz, M., & Seco, J. (2020). Prompt gamma spectroscopy for absolute range verification of 12C ions at synchrotron-based facilities. Physics in Medicine and Biology, 65(9).

Dauvergne, D., Battaglia, M., Montarou, G., & Testa, E. (2009). New methods of real-time control imaging for ion therapy. 1st NIRS-ETOILE Symposium, 154–160.

Durante, M., and Debus, J. (2018). Heavy Charged Particles: Does Improved Precision and Higher Biological Effectiveness Translate to Better Outcome in Patients? Seminars in Radiation Oncology 28, 160–167.

Eley, J. G., Newhauser, W. D., Richter, D., Lüchtenborg, R., Saito, N., & Bert, C. (2015). Robustness of target dose coverage to motion uncertainties for scanned carbon ion beam tracking therapy of moving tumors. Physics in Medicine and Biology, 60(4), 1717–1740.

Enghardt, W., Crespo, P., Fiedler, F., Hinz, R., Parodi, K., Pawelke, J., & Pönisch, F. (2004). Charged hadron tumour therapy monitoring by means of PET. In Nuclear Instruments and Methods in Physics Research, Section A: Accelerators, Spectrometers, Detectors and Associated Equipment, Vol. 525, pp. 284–288.

Fano, U. (1963). Penetration of Protons, Alpha Particles, and Mesons. Annual Review of Nuclear Science, 13(1), 1–66.

Farr, J. B., Flanz, J. B., Gerbershagen, A., & Moyers, M. F. (2018). New horizons in particle therapy systems. In Medical Physics (Vol. 45, pp. e953–e983). John Wiley and Sons Ltd.

Félix-Bautista, R., Gehrke, T., Ghesquiere-Diérickx, L., Reimold, M., Amato, C., Turecek, D., … Martišiková, M. (2019). Experimental verification of a non-invasive method to monitor the lateral pencil beam position in an anthropomorphic phantom for carbon-ion radiotherapy. Physics in Medicine and Biology, 64(17).

Félix-Bautista, R., Ghesquiere-Diérickx, L., Marek, L., Granja, C., Soukup, P., … Martišiková, M. (2021). Quality assurance method for monitoring of lateral pencil beam positions in scanned carbon-ion radiotherapy using tracking of secondary ions. Provisionally accepted in Medical Physics.

Ferrero, V., Fiorina, E., Morrocchi, M., Pennazio, F., Baroni, G., Battistoni, G., … Bisogni, M. G. (2018). Online proton therapy monitoring: Clinical test of a Silicon-photodetector-based in-beam PET. Scientific Reports, 8(1)

Fiorino, C., Guckemberger, M., Schwarz, M., van der Heide, U.A., and Heijmen, B. (2020). Technology-driven research for radiotherapy innovation. Molecular Oncology 14, 1500–1513.

Fischetti, M., Baroni, G., Battistoni, G., Bisogni, G., Cerello, P., Ciocca, M., … Sarti, A. (2020). Inter-fractional monitoring of 12 C ions treatments: results from a clinical trial at the CNAO facility. Scientific Reports, 10(1).

FitzGerald, T. J., Bishop-Jodoin, M., Laurie, F., O'Meara, E., Davis, C., Bogart, J., … Cicchetti, M. G. (2018). The Importance of Imaging in Radiation Oncology for National Clinical Trials Network Protocols. International Journal of Radiation Oncology Biology Physics, 102(4), 775–782.

Francis, Z., Seif, E., Incerti, S., Champion, C., Karamitros, M., Bernal, M. A., … El Bitar, Z. (2014). Carbon ion fragmentation effects on the nanometric level behind the Bragg peak depth. Physics in Medicine and Biology, 59(24), 7691–7702.

Fukumoto, S. (1995). Cyclotron Versus Synchrotron for Proton Beam Therapy. Proceedings of the 14th International Conference on Cyclotrons and Their Applications, 533–536.

Gaa, T., Reinhart, M., Hartmann, B., Jakubek, J., Soukup, P., Jäkel, O., & Martišíková, M. (2017). Visualization of air and metal inhomogeneities in phantoms irradiated by carbon ion beams using prompt secondary ions. Physica Medica, 38, 140–147.

Gaimard, J. J., & Schmidt, K. H. (1991). A reexamination of the abrasion-ablation model for the description of the nuclear fragmentation reaction. Nuclear Physics, Section A, 531(3–4), 709–745.

Gehrke, T., Burigo, L., Arico, G., Berke, S., Jakubek, J., Turecek, D., … Martišíková, M. (2017). Energy deposition measurements of single 1H, 4He and 12C ions of therapeutic energies in a silicon pixel detector. Journal of Instrumentation, 12(4).

Gehrke, T., Gallas, R., Jäkel, O., & Martišíková, M. (2018). Proof of principle of helium-beam radiography using silicon pixel detectors for energy deposition measurement, identification, and tracking of single ions: Medical Physics, 45(2), 817–829.

Giap, H., and Giap, B. (2012). Historical perspective and evolution of charged particle beam therapy. Translational Cancer Research 1, 127–136.

Gillin, M. T., Sahoo, N., Bues, M., Ciangaru, G., Sawakuchi, G., Poenisch, F., … Zhu, X. R. (2010). Commissioning of the discrete spot scanning proton beam delivery system at the

University of Texas M.D. Anderson Cancer Center, Proton Therapy Center, Houston. Medical Physics, 37(1), 154–163.

Glowa, C., Karger, C. P., Brons, S., Zhao, D., Mason, R. P., Huber, P. E., … Peschke, P. (2016). Carbon ion radiotherapy decreases the impact of tumor heterogeneity on radiation response in experimental prostate tumors. Cancer Letters, 378(2), 97–103.

Glowa, C., Peschke, P., Brons, S., Neels, O. C., Kopka, K., Debus, J., & Karger, C. P. (2017). Carbon ion radiotherapy: Impact of tumor differentiation on local control in experimental prostate carcinomas. Radiation Oncology, 12(1).

Golovchenko, A. N., Skvarč, J., Yasuda, N., Giacomelli, M., Tretyakova, S. P., Ilić, R., … Murakami, T. (2002). Total charge-changing and partial cross-section measurements in the reactions of ~100-250 MeV/nucleon ^{12}C in carbon, paraffin, and water. Physical Review C - Nuclear Physics, 66(1), 8.

Granja, C., Oancea, C., Jakubek, J., Marek, L., Benton, E., Kodaira, S., … Krist, P. (2021). Wide-range tracking and LET-spectra of energetic light and heavy charged particles. Nuclear Instruments and Methods in Physics Research, Section A: Accelerators, Spectrometers, Detectors and Associated Equipment, 988.

Grau, C., Durante, M., Georg, D., Langendijk, J. A., & Weber, D. C. (2020, July 1). Particle therapy in Europe. Molecular Oncology. John Wiley and Sons Ltd.

Grevillot, L., Osorio Moreno, J., Letellier, V., Dreindl, R., Elia, A., Fuchs, H., … Stock, M. (2020). Clinical implementation and commissioning of the MedAustron Particle Therapy Accelerator for non-isocentric scanned proton beam treatments. Medical Physics, 47(2), 380–392.

Gunzert-Marx, K., Iwase, H., Schardt, D., & Simon, R. S. (2008). Secondary beam fragments produced by 200 MeV u-1 12C ions in water and their dose contributions in carbon ion radiotherapy. New Journal of Physics, 10.

Gwosch, K., Hartmann, B., Jakubek, J., Granja, C., Soukup, P., Jäkel, O., & Martišíková, M. (2013). Non-invasive monitoring of therapeutic carbon ion beams in a homogeneous phantom by tracking of secondary ions. Physics in Medicine and Biology, 58(11), 3755–3773.

Haberer, T., Becher, W., Schardt, D., & Kraft, G. (1993). Magnetic scanning system for heavy ion therapy. Nuclear Inst. and Methods in Physics Research, A, 330(1–2), 296–305.

Haberer, T., Debus, J., Eickhoff, H., Jäkel, O., Schulz-Ertner, D., & Weber, U. (2004). The Heidelberg ion therapy center. In Radiotherapy and Oncology (Vol. 73). Elsevier Ireland Ltd.

Haettner, E., Iwase, H., Krämer, M., Kraft, G., & Schardt, D. (2013). Experimental study of nuclear fragmentation of 200 and 400 MeV/u 12C ions in water for applications in particle therapy. Physics in Medicine and Biology, 58(23), 8265–8279.

Hagiwara, Y., Oike, T., Niimi, A., Yamauchi, M., Sato, H., Limsirichaikul, S., … Shibata, A. (2019). Clustered DNA double-strand break formation and the repair pathway following heavy-ion irradiation. Journal of Radiation Research, 60(1), 69–79.

Henriquet, P., Testa, E., Chevallier, M., Dauvergne, D., Dedes, G., Freud, N., … Sauli, F. (2012). Interaction vertex imaging (IVI) for carbon ion therapy monitoring: A feasibility study. Physics in Medicine and Biology, 57(14), 4655–4669.

Highland, V. L. (1975). Some practical remarks on multiple scattering. Nuclear Instruments and Methods, 129(2), 497–499.

Hofmann, T., Pinto, M., Mohammadi, A., Nitta, M., Nishikido, F., Iwao, Y., … Parodi, K. (2019). Dose reconstruction from PET images in carbon ion therapy: A deconvolution approach. Physics in Medicine and Biology, 64(2).

Horst, F. (2019). Measurement of Nuclear Reaction Cross Sections for Applications in Radiotherapy with Protons, Helium and Carbon Ions. Doctoral Dissertation, Justus-Liebig-Universität, Giessen, Germany.

Hueso-González, F., Rabe, M., Ruggieri, T. A., Bortfeld, T., & Verburg, J. M. (2018). A full-scale clinical prototype for proton range verification using prompt gamma-ray spectroscopy. Physics in Medicine and Biology, 63(18).

Hüfner, J., Schäfer, K., & Schürmann, B. (1975). Abrasion-ablation in reactions between relativistic heavy ions. Physical Review C, 12(6), 1888–1898.

ICRU85. ICRU Report 85a - Fundamental Quantities And Units For Ionizing Radiation. Journal of the ICRU, 11(1):1–35, 2011.

Inaniwa, T., Furukawa, T., Kase, Y., Matsufuji, N., Toshito, T., Matsumoto, Y., … Noda, K. (2010). Treatment planning for a scanned carbon beam with a modified microdosimetric kinetic model. Physics in Medicine and Biology, 55(22), 6721–6737.

Inaniwa, T., Kanematsu, N., Matsufuji, N., Kanai, T., Shirai, T., Noda, K., … Tsujii, H. (2015). Reformulation of a clinical-dose system for carbon-ion radiotherapy treatment planning at the National Institute of Radiological Sciences, Japan. Physics in Medicine and Biology, 60(8), 3271–3286.

Iwata, Y., Fujimoto, T., Matsuba, S., Fujita, T., Sato, S., Furukawa, T., … Noda, K. (2016). Beam commissioning of a superconducting rotating-gantry for carbon-ion radiotherapy. Nuclear Instruments and Methods in Physics Research, Section A: Accelerators, Spectrometers, Detectors and Associated Equipment, 834, 71–80.

Jäkel, O. (2009). Medical physics aspects of particle therapy. In Radiation Protection Dosimetry (Vol. 137, pp. 156–166).

Jäkel, O., Hartmann, G. H., Karger, C. P., Heeg, P., & Rassow, J. (2000). Quality assurance for a treatment planning system in scanned ion beam therapy. Medical Physics, 27(7), 1588–1600.

Jäkel, O., Krämer, M., Karger, C. P., & Debus, J. (2001). Treatment planning for heavy ion radiotherapy: Clinical implementation and application. Physics in Medicine and Biology, 46(4), 1101–1116.

Jakubek, J. (2009). Energy-sensitive X-ray radiography and charge sharing effect in pixelated detector. Nuclear Instruments and Methods in Physics Research, Section A: Accelerators, Spectrometers, Detectors and Associated Equipment, 607(1), 192–195.

Jakubek, J. (2011). Precise energy calibration of pixel detector working in time-over-threshold mode. In Nuclear Instruments and Methods in Physics Research, Section A: Accelerators, Spectrometers, Detectors and Associated Equipment (Vol. 633).

Jakubek, J., Jakubek, M., Platkevic, M., Soukup, P., Turecek, D., Sykora, V., & Vavrik, D. (2014). Large area pixel detector WIDEPIX with full area sensitivity composed of 100 Timepix assemblies with edgeless sensors. Journal of Instrumentation, 9(4).

Jelen, U., Bubula, M. E., Ammazzalorso, F., Engenhart-Cabillic, R., Weber, U., & Wittig, A. (2013). Dosimetric impact of reduced nozzle-to-isocenter distance in intensity-modulated proton therapy of intracranial tumors in combined proton-carbon fixed-nozzle treatment facilities. Radiation Oncology, 8(1).

Jensen, A.D., Münter, M.W., and Debus, J. (2011). Review of clinical experience with ion beam radiotherapy. British Journal of Radiology 84.

Johnson, D., Chen, Y., & Ahmad, S. (2015). Dose and linear energy transfer distributions of primary and secondary particles in carbon ion radiation therapy: A Monte Carlo simulation study in water. Journal of Medical Physics, 40(4), 214–219.

Kanai, T., Furusawa, Y., Fukutsu, K., Itsukaichi, H., Eguchi-Kasai, K., & Ohara, H. (1997). Irradiation of mixed beam and design of spread-out Bragg peak for heavy- ion radiotherapy. Radiation Research, 147(1), 78–85.

Kanai, T., Endo, M., Minohara, S., Miyahara, N., Koyama-Ito, H., Tomura, H., … Kawachi, K. (1999). Biophysical characteristics of HIMAC clinical irradiation system for heavy-ion radiation therapy. International Journal of Radiation Oncology Biology Physics, 44(1), 201–210.

Karger, C.P., Jäkel, O., Palmans, H., and Kanai, T. (2010). Dosimetry for ion beam radiotherapy. Physics in Medicine and Biology 55.

Karger, C.P., and Peschke, P. (2018). RBE and related modeling in carbon-ion therapy. Physics in Medicine and Biology 63.

Kase, Y., Kanai, T., Matsumoto, Y., Furusawa, Y., Okamoto, H., Asaba, T., … Shinoda, H. (2006). Microdosimetric measurements and estimation of human cell survival for heavy-ion beams. Radiation Research, 166(4), 629–638.

Knoll, G. F. Radiation Detection and Measurement. Fourth Edition, Wiley & Sons, Inc., 2010.

Kraan, A. C. (2015). Range verification methods in particle therapy: Underlying physics and Monte Carlo modelling. Frontiers in Oncology, 5(JUN).

Krämer, M., & Kraft, G. (1994a). Calculations of heavy-ion track structure. Radiation and Environmental Biophysics, 33(2), 91–109.

Krämer, M., & Kraft, G. (1994b). Track structure and DNA damage. Advances in Space Research, 14(10), 151–159.

Krämer, M., Scifoni, E., Schuy, C., Rovituso, M., Tinganelli, W., Maier, A., … Durante, M. (2016). Helium ions for radiotherapy? Physical and biological verifications of a novel treatment modality. Medical Physics, 43(4), 1995–2004.

Langner, U. W., Eley, J. G., Dong, L., & Langen, K. (2017). Comparison of multi-institutional Varian ProBeam pencil beam scanning proton beam commissioning data. Journal of Applied Clinical Medical Physics, 18(3), 96–107.

Leo, W. R. Techniques for Nuclear and Particle Physics Experiments: A How-To Approach. Springer-Verlag, Berlin Heidelberg, 1994.

Leroy, C. and Rancoita, P. G. Principles of Radiation Interaction in Matter and Detection, Third Edition, World Scientific Publishing Co., 2011.

Li, H., Sahoo, N., Poenisch, F., Suzuki, K., Li, Y., Li, X., … Zhu, X. R. (2013). Use of treatment log files in spot scanning proton therapy as part of patient-specific quality assurance. Medical Physics, 40(2).

Linz, U. Ion Beam Therapy: Fundamentals, Technology, Clinical Applications. Springer, 2012.

Llopart, X., Ballabriga, R., Campbell, M., Tlustos, L., & Wong, W. (2007). Timepix, a 65k programmable pixel readout chip for arrival time, energy and/or photon counting measurements. Nuclear Instruments and Methods in Physics Research, Section A: Accelerators, Spectrometers, Detectors and Associated Equipment, 581(1-2 SPEC. ISS.), 485–494.

Lomax, A. J. (2008). Intensity modulated proton therapy and its sensitivity to treatment uncertainties 2: The potential effects of inter-fraction and inter-field motions. Physics in Medicine and Biology, 53(4), 1043–1056.

Lomax, M. E., Folkes, L. K., & O'Neill, P. (2013). Biological consequences of radiation-induced DNA damage: Relevance to radiotherapy. Clinical Oncology, 25(10), 578–585.

Lutz, G. Semiconductor Radiation Detectors: Device Physics. Accelerator Physics Series. Springer-Verlag Berlin Heidelberg, 2007.

Lutz G. and Klanner R. Solid State Detectors. In: Fabjan C., Schopper H. (eds) Particle Physics Reference Library: Volume 2: Detectors for Particles and Radiation. Springer, Cham., 2020.

Magalhaes Martins, P., Dal Bello, R., Ackermann, B., Brons, S., Hermann, G., Kihm, T., & Seco, J. (2020). PIBS: Proton and ion beam spectroscopy for in vivo measurements of oxygen, carbon, and calcium concentrations in the human body. Scientific Reports, 10(1).

Magallanes-Hernández, L. (2017). Low-dose ion-based transmission radiography and tomography for optimization of carbon ion-beam therapy. Doctoral Dissertation, Ludwig Maximilian University of Munich, Munich, Germany.

Malouff, T.D., Mahajan, A., Krishnan, S., Beltran, C., Seneviratne, D.S., and Trifiletti, D.M. (2020). Carbon Ion Therapy: A Modern Review of an Emerging Technology. Frontiers in Oncology 10.

Marek, L. (2020). Directional and spectrometric mapping of secondary radiation induced during hadron radiotherapy with miniaturized particle trackers. Master's Thesis, Czech Technical University of Prague, Prague, Czech Republic.

Martišíková, M., Hartmann, B., Hesse, B. M., Brons, S., Ackermann, B., & Jäkel, O. (2012). Characterization of a flat-panel detector for ion beam spot measurements. Physics in Medicine and Biology, 57(2), 485–497.

Martišíková, M., & Jäkel, O. (2010). Study of Gafchromic EBT film response over a large dose range. Physics in Medicine and Biology, 55(10).

Martišíková, M., Gehrke, T., Berke, S., Aricò, G., & Jäkel, O. (2018). Helium ion beam imaging for image guided ion radiotherapy. Radiation Oncology, 13(1).

Matsufuji, N., Komori, M., Sasaki, H., Akiu, K., Ogawa, M., Fukumura, A., … Kanai, T. (2005). Spatial fragment distribution from a therapeutic pencil-like carbon beam in water. Physics in Medicine and Biology, 50(14), 3393–3403.

Mein, S., Dokic, I., Klein, C., Tessonnier, T., Böhlen, T. T., Magro, G., … Mairani, A. (2019). Biophysical modeling and experimental validation of relative biological effectiveness (RBE) for 4He ion beam therapy. Radiation Oncology, 14(1).

Min, C. H., Zhu, X., Winey, B. A., Grogg, K., Testa, M., El Fakhri, G., … Shih, H. A. (2013). Clinical application of in-room positron emission tomography for in vivo treatment monitoring in proton radiation therapy. International Journal of Radiation Oncology Biology Physics, 86(1), 183–189.

Mobaraki, A., Ohno, T., Yamada, S., Sakurai, H., & Nakano, T. (2010). Cost-effectiveness of carbon ion radiation therapy for locally recurrent rectal cancer. Cancer Science, 101(8), 1834–1839.

Mohamad, O., Makishima, H., and Kamada, T. (2018). Evolution of carbon ion radiotherapy at the national institute of radiological sciences in Japan. Cancers 10.

Molière, G. (1948). Theorie der Streuung schneller geladener Teilchen II Mehrfach-und Vielfachstreuung1. Zeitschrift Fur Naturforschung - Section A Journal of Physical Sciences, 3(2), 78–97.

Molinelli, S., Mairani, A., Mirandola, A., Vilches Freixas, G., Tessonnier, T., Giordanengo, S., … Orecchia, R. (2013). Dosimetric accuracy assessment of a treatment plan verification system for scanned proton beam radiotherapy: One-year experimental results and Monte Carlo analysis of the involved uncertainties. Physics in Medicine and Biology, 58(11), 3837–3847.

Muraro, S., Battistoni, G., Collamati, F., De Lucia, E., Faccini, R., Ferroni, F., Fiore, S., Fralicciardi, P., Marafini, M., Mattei, I., et al. (2016). Monitoring of hadrontherapy treatments by means of charged particle detection. Frontiers in Oncology 6.

Parodi, K., Mairani, A., Brons, S., Hasch, B. G., Sommerer, F., Naumann, J., … Debus, J. (2012). Monte Carlo simulations to support start-up and treatment planning of scanned proton and carbon ion therapy at a synchrotron-based facility. Physics in Medicine and Biology, 57(12), 3759–3784.

Peach, K., Wilson, P., and Jones, B. (2011). Accelerator science in medical physics. British Journal of Radiology 84.

Peeters, A., Grutters, J. P. C., Pijls-Johannesma, M., Reimoser, S., De Ruysscher, D., Severens, J. L., … Lambin, P. (2010). How costly is particle therapy? Cost analysis of external beam radiotherapy with carbon-ions, protons and photons. Radiotherapy and Oncology, 95(1), 45–53.

Pereira, G.C., Traughber, M., and Muzic, R.F. (2014). The role of imaging in radiation therapy planning: Past, present, and future. BioMed Research International 2014.

Piersanti, L., Bellini, F., Bini, F., Collamati, F., De Lucia, E., Durante, M., … Voena, C. (2014). Measurement of charged particle yields from PMMA irradiated by a 220 MeV/u 12C beam. Physics in Medicine and Biology, 59(7), 1857–1872.

Poikela, T., Plosila, J., Westerlund, T., Campbell, M., Gaspari, M. D., Llopart, X., … Kruth, A. (2014). Timepix3: A 65K channel hybrid pixel readout chip with simultaneous ToA/ToT and sparse readout. Journal of Instrumentation, 9(5).

PTCOG Patient Statistics, https://www.ptcog.ch/index.php/ptcog-patient-statistics

PTCOG Therapy Facilities, https://www.ptcog.ch/index.php/facilities-in-operation

Reidel, C. A., Finck, C., Schuy, C., Rovituso, M., & Weber, U. (2019). Alignment procedure of silicon pixel detectors for ion-beam therapy applications. Nuclear Instruments and Methods in Physics Research, Section A: Accelerators, Spectrometers, Detectors and Associated Equipment, 931, 142–150.

Reimold, M. (2018). Monitoring of carbon ion pencil beams in a homogeneous PMMA phantom using Timepix3 detectors. Master's Thesis, University of Heidelberg, Heidelberg, Germany.

Reinhart, A. M., Spindeldreier, C. K., Jakubek, J., & Martišíková, M. (2017). Three dimensional reconstruction of therapeutic carbon ion beams in phantoms using single secondary ion tracks. Physics in Medicine and Biology, 62(12), 4884–4896.

Richter, C., Pausch, G., Barczyk, S., Priegnitz, M., Keitz, I., Thiele, J., … Baumann, M. (2016). First clinical application of a prompt gamma based in vivo proton range verification system. Radiotherapy and Oncology, 118(2), 232–237.

Rizzoglio, V., Adelmann, A., Gerbershagen, A., Meer, D., Nesteruk, K.P., and Schippers, J.M. (2020). Uncertainty quantification analysis and optimization for proton therapy beam lines. Physica Medica 75, 11–18.

Robert, C., Dedes, G., Battistoni, G., Böhlen, T. T., Buvat, I., Cerutti, F., … Testa, E. (2013). Distributions of secondary particles in proton and carbon-ion therapy: A comparison between GATE/Geant4 and FLUKA Monte Carlo codes. Physics in Medicine and Biology, 58(9), 2879–2899.

Rucinski, A., Battistoni, G., Collamati, F., De Lucia, E., Faccini, R., Frallicciardi, P. M., … Patera, V. (2018). Secondary radiation measurements for particle therapy applications: Charged particles produced by 4He and 12C ion beams in a PMMA target at large angle. Physics in Medicine and Biology, 63(5).

Russo, S., Mirandola, A., Molinelli, S., Mastella, E., Vai, A., Magro, G., … Ciocca, M. (2017). Characterization of a commercial scintillation detector for 2-D dosimetry in scanned proton and carbon ion beams. Physica Medica, 34, 48–54.

Schardt, D. (2007). Tumor therapy with high-energy carbon ion beams. Nuclear Physics A, 787(1-4 SPEC. ISS.), 633–641.

Schardt, D., Elsässer, T., and Schulz-Ertner, D. (2010). Heavy-ion tumor therapy: Physical and radiobiological benefits. Reviews of Modern Physics 82, 383–425.

Schaub, L., Harrabi, S.B., and Debus, J. (2020). Particle therapy in the future of precision therapy. The British Journal of Radiology 93, 20200183.

Schlegel, W and Bille J. Medizinische Physik 2. Medizinische Strahlenphysik. Springer-Verlag, Berlin Heidelberg, 2002.

Scholz, M., & Kraft, G. (1992). A Parameter-Free Track Structure Model for Heavy-Ion Action Cross-Sections. In Biophysical Modelling of Radiation Effects (Vol. 24, pp. 185-192\r351).

Scholz, M., & Kraft, G. (1994). Calculation of heavy ion inactivation probabilities based on track structure, X ray sensitivity and target size. In Radiation Protection Dosimetry (Vol. 52, pp. 29–33). Oxford University Press.

Scholz, M., & Kraft, G. (1996). Track structure and the calculation of biological effects of heavy charged particles. Advances in Space Research, 18(1–2), 5–14.

Seidel, S. (2019). Silicon strip and pixel detectors for particle physics experiments. Physics Reports, 828, 1–34.

Schulz-Ertner, D., Jäkel, O., & Schlegel, W. (2006). Radiation Therapy With Charged Particles. Seminars in Radiation Oncology, 16(4), 249–259.

Seidel, S. (2019). Silicon strip and pixel detectors for particle physics experiments. Physics Reports 828, 1–34.

Serber, R. (1947). Nuclear reactions at high energies. Physical Review, 72(11), 1114–1115.

Silari, M. (2011). Applications of particle accelerators in medicine. Radiation Protection Dosimetry, 146(4), 440–450.

Soukup P, Jakubek J and Vykydal Z. (2011). 3D sensitive voxel detector of ionizing radiation based on Timepix device. In Journal of Instrumentation (Vol. 6).

Spiriti, E., Finck, C., Baudot, J., Divay, C., Juliani, D., Labalme, M., … Romano, F. (2017). CMOS active pixel sensors response to low energy light ions. Nuclear Instruments and Methods in Physics Research, Section A: Accelerators, Spectrometers, Detectors and Associated Equipment, 875, 35–40.

Sprave, T., Verma, V., Sterzing, F., Bruckner, T., Hees, K., Land, B., … Uhl, M. (2018). Cost-effectiveness of carbon ion radiation therapy for skull base chordoma utilizing long-term (10-year) outcome data. Anticancer Research, 38(8), 4853–4858.

Tessonnier, T., Marcelos, T., Mairani, A., Brons, S., & Parodi, K. (2016). Phase space generation for proton and carbon ion beams for external users' applications at the heidelberg ion therapy center. Frontiers in Oncology, 5(JAN).

Tessonnier, T., Mairani, A., Brons, S., Sala, P., Cerutti, F., Ferrari, A., … Parodi, K. (2017). Helium ions at the Heidelberg Ion Beam Therapy center: Comparisons between FLUKA Monte Carlo code predictions and dosimetric measurements. Physics in Medicine and Biology, 62(16), 6784–6803.

Toppi, M., Battistoni, G., Bellini, F., Collamati, F., De Lucia, E., Durante, M., … Voena, C. (2016). Measurement of secondary particle production induced by particle therapy ion beams impinging on a PMMA target. In EPJ Web of Conferences (Vol. 117). EDP Sciences.

Toshito, T., Kodama, K., Sihver, L., Yusa, K., Ozaki, M., Amako, K., … Shibuya, H. (2007). Measurements of total and partial charge-changing cross sections for 200- to 400-MeV/nucleon 12C on water and polycarbonate. Physical Review C - Nuclear Physics, 75(5).

Traini, G., Battistoni, G., Bollella, A., Collamati, F., De Lucia, E., Faccini, R., … Patera, V. (2017). Design of a new tracking device for on-line beam range monitor in carbon therapy. Physica Medica, 34, 18–27.

Traini, G., Mattei, I., Battistoni, G., Bisogni, M. G., De Simoni, M., Dong, Y., … Sarti, A. (2019). Review and performance of the Dose Profiler, a particle therapy treatments online monitor. Physica Medica, 65, 84–93

Uhl, M., Herfarth, K., and Debus, J. (2014). Comparing the use of protons and carbon ions for treatment. Cancer Journal (United States) 20, 433–439.

Vanderstraeten, B., Verstraete, J., De Croock, R., De Neve, W., & Lievens, Y. (2014). In search of the economic sustainability of hadron therapy: The real cost of setting up and operating

a hadron facility. International Journal of Radiation Oncology Biology Physics, 89(1), 152–160.

Varasteh Anvar, M., Attili, A., Ciocca, M., Donetti, M., Fanola Guarachi, L. K., Fausti, F., … Cirio, R. (2016). Quality assurance of carbon ion and proton beams: A feasibility study for using the 2D MatriXX detector. Physica Medica, 32(6), 831–837.

Vavilov, P. (1957). Ionization losses of high-energy heavy particles. Soviet Phys. JETP, Vol: 5.

Weber, U., and Kraft, G. (2009). Comparison of carbon ions versus protons. Cancer Journal 15, 325–332.

Wozny, A. S., Alphonse, G., Cassard, A., Malésys, C., Louati, S., Beuve, M., … Rodriguez-Lafrasse, C. (2020). Impact of hypoxia on the double-strand break repair after photon and carbon ion irradiation of radioresistant HNSCC cells. Scientific Reports, 10(1).

Xie, Y., Bentefour, E. H., Janssens, G., Smeets, J., Vander Stappen, F., Hotoiu, L., … Teo, B. K. K. (2017). Prompt Gamma Imaging for In Vivo Range Verification of Pencil Beam Scanning Proton Therapy. International Journal of Radiation Oncology Biology Physics, 99(1), 210–218.

Xie, Y., Petzoldt, J., Janssens, G., O'Grady, F., Yin, L., Bentefour, E. H., … Teo, B. K. (2020). Prompt gamma imaging for the identification of regional proton range deviations due to anatomic change in a heterogeneous region. The British Journal of Radiology, 93(1116), 20190619.

Yasui, K., Toshito, T., Omachi, C., Hayashi, K., Tanaka, K., Asai, K., … Hayashi, N. (2018). Evaluation of dosimetric advantages of using patient-specific aperture system with intensity-modulated proton therapy for the shallow depth tumor. Journal of Applied Clinical Medical Physics, 19(1), 132–137.

Zeitlin, C., Guetersloh, S., Heilbronn, L., Miller, J., Fukumura, A., Iwata, Y., & Murakami, T. (2007). Fragmentation cross sections of 290 and 400 MeV/nucleon C12 beams on elemental targets. Physical Review C - Nuclear Physics, 76(1).

Zeitlin, C., and La Tessa, C. (2016). The role of nuclear fragmentation in particle therapy and space radiation protection. Frontiers in Oncology 6.

Zhu, X.R., Li, Y., Mackin, D., Li, H., Poenisch, F., Lee, A.K., Mahajan, A., Frank, S.J., Gillin, M.T., Sahoo, N., et al. (2015). Towards effective and efficient patient-specific quality assurance for spot scanning proton therapy. Cancers 7, 631–647.

Zyla, P.A., Barnett, R.M., Beringer, J., Dahl, O., Dwyer, D.A., Groom, D.E., Lin, C.J., Lugovsky, K.S., Pianori, E., Robinson, D.J., et al. (2020). Review of particle physics. Progress of Theoretical and Experimental Physics 2020, 1–2093.

Acknowledgments

I would like to express my gratitude to all the persons supporting me in many aspects during my PhD project.

First of all, I am very thankful to Prof. Dr. Oliver Jäkel for giving me the opportunity to carry out my PhD research in the Department of Medical Physics in Radiation Oncology. It has been a grateful experience to acquire knowledge and gain more experience in this friendly environment. I am also thankful to him and to Prof. Dr. Joao Seco for accepting to be my examiners of my work.

I am sincerely thankful to Dr. Mária Martišíková, my supervisor since my Master's thesis, for giving me the opportunity to continue working on this project in my PhD, for the unlimited support in each aspect of my work and for the availability to clarify, answer and discuss my doubts and ideas to publish my papers and to pursue the goals of this research.

I would also like to thank to Dr. Tim Gehrke and Laura Ghesquière-Diérickx for their priceless support. I thank to all the students that have been in the research group of Novel Detection Techniques for Ion Beams during these years and friend from another research groups, for the pleasant atmosphere in the office, coffee breaks and our very fancy social life during experiments and beers on the Neckarwiese. Definitely, this is the best group ever!

I want to express my gratitude to Jan Jakubek and the group of ADVACAM for their support with the Timepix3 detectors. I thank to the HIT facility and to Dr. Stephan Brons for the performance of the experiments. I thank Gernot Echner, Armin Runz and the workshop for the manufactured components needed for my experiments.

I also thank to Prof. Dr. Christian Karger and Dr. Reiner Stamen for being part of my Thesis Advisor Committee together with Dr. Mária Martišíková. I thank to Prof. Dr. Loredana Gastaldo and Prof. Dr. Björn Malte Schäfer for being my referees of the Experimental and Theoretical Physics fields, respectively.

Finally, I want to thank my parents for their blessing, their trust and their never-ending support regardless of distance. I thank to all my friends. I deeply grateful to You, who has allowed me to continue walking forward, and who gives me the strength of the universe, You, who are within me. From the deepest part of my heart, thank You!

Declaration

I, Renato Félix Bautista, declare here that this PhD thesis is the result of my own research, and that all sources used in this work have been duly referenced.

This thesis has not been submitted to any other university or institute for a degree award.

Heidelberg, April 12th, 2021

….....